quarterly

ISSN 1898-4088 (printed)
ISSN 2300-5319 (online)

2018
volume 12 no. 4

acta mechanica et automatica

CONTENTS

sciendo

DOI 10.2478/ama-2018-0039

acta mechanica et automatica, vol.12 no.4 (2018)

ELECTROPLASTIC DEFORMATION BY TWINNINGMETALS

VLADIMIR V. SAVENKO*

*Physics and Engineering Faculty, Mozyr State Pedagogical University
named after I.P.Shamyakin, 28 Studencheskaya Str., 247760, Mozyr, Republic of Belarus

savenko-vl@rambler.ru

received 1 March 2018, revised 15 October 2018, accepted 18 October 2018

Abstract: The article deals with theoretical and experimental approaches to electroplastic deformation caused by twinning of metals. The author specifies physical fundamentals of Kinetics regarding the development of twinning caused by the excitation of electronic subsystem of metals. Physical models of new channels for the realization of twinning aroused under conditions of electroplasticity have been discussed. Mechanisms of plasticized influence of a surface electric charge have been defined as well as the contribution of a dynamic pinch-effect in the elastic plastic deformation of metals with the participation of the intrinsic magnetic field of the current. The dynamic pinch effect creates ultrasonic vibration of the lattice system while Kinetics changes and plastic deformation are stimulated increasing the amplitude of the oscillations of rectilinear dislocations and the periodic change in the position of the dislocation loops with an increase in the probability of detachment of dislocations from the stoppers. When deformed above the yield point and due to the pinch effect the intrinsic magnetic field of the current diffuses into the crystal where the diffusion rate depends both on the conductivity of the metal and on the frequency of the current. It is necessary to take into account the physical conditions for the creation of ponderomotive effects in relation to specific technically important materials for the practical use of electroplastic deformation technology, especially when processing metals with pressure.

Keywords: Electroplastic Deformation, Ponderomotive Action Current, Pinch Effect, Skin Effect, Pulse Current, Magnetic Field, Electric Field Vortex Field Hall, Mechanical Pressure, Maximum Axial Force

1. INTRODUCTION

Development of Modern Physical Material as a science is closely associated with the development of technological processes of deformation for metals caused by the pressure found under the conditions of electroplasticity with the aim to obtain technically important materials with high characteristics that ensure their application in extreme physical conditions.

Electroplasticity found in metals is implemented by passing short pulses of high density current of 10^3A/mm^2 with a duration of 10^{-4}s, during plastic deformation through electrically conductive materials, which is known as the electroplastic effect (EPE).This effect is universal and manifests itself in all materials under different types of plastic deformation by sliding (magnesium steel) and twinning (bismuth).

EPE stimulates deformation processes, reduces strain forces, energy consumption and improves the physical and mechanical characteristics of the material.

Several authors explain the mechanisms of electroplastic deformation in the course of sliding by electron-dislocation interaction, the pressure of the "electronic wind" on the accumulation of dislocations, point defects, decrease in starting stresses for dislocation disruption from the stoppers, the action of thermal and nonthermic effective stresses and also the spin softening of metals (Troitskiy and Savenko, 2013; Khrushchev et al., 2017; Troitskiy, 2008b; Stashenko et al., 2008).

It should be noted when a current pulse is excited in the metal deformation zone, a significant amount of Joule heat is released, with a pulse duration equals to 100μs and a current density equals to 100 to several thousand A/mm^2, heating the sample does not exceed several degrees if the pulses are separated intervals equal to tens of seconds.

Plastic deformation by twinning is carried out when the slip is impossible, for example, while orientational inhibition at high loading rates and at low temperatures. The twinning begins at stress concentrators, the development of twins is carried out at high velocities. The concentration of stresses and deformations at the boundaries of twins often lead to the destruction of the material.

Thus, if it was possible to control the development of twinning, there would be a real opportunity to use twinning as a reservoir of material plasticity if to reduce the concentration of stresses at the boundaries of twins. Furthermore the twin boundaries are natural obstacles to complete dislocations, that's why it is possible to strengthen the material in an effective way by means of a system of thin twins.

2. EXPERIMENTAL METHODS, RESULTS AND DISCUSSION

When electric current pulses pass through metal single crystals with density equals to 50-1000 A/mm^2 and duration equals to 10^{-4}s, a redistribution of deformation by twinning is observed in the vicinity of the stress concentrators. If the crystal is deformed by a diamond indentor and current pulses are passed before or after deformation, no effect is observed. The constant electric field imposed on the crystal at any stage of deformation is also not effective. However, if the electric current pulse is passed through the crystal during deformation, the pattern of the indenter print

DOI 10.2478/ama-2018-0039

changes significantly. The print on the left is obtained after 10 seconds of holding the crystal with an indentor load of 10g. The imprint on the right corresponds to the same exposure and load to the indenter, but 5 seconds passed the load was lowered, a current pulse 10^{-4}s was passed through the sample. The current density in the pulse was 600 A/mm^2.

Comparison of the strain patterns with the current pulse and without a pulse shows that under the combined effect of electrical and mechanical stresses, the plastic deformation is stimulated by twinning. The length of individual twins increases, new twins appear. Thus, all the side factors affecting the deformation conditions were excluded.

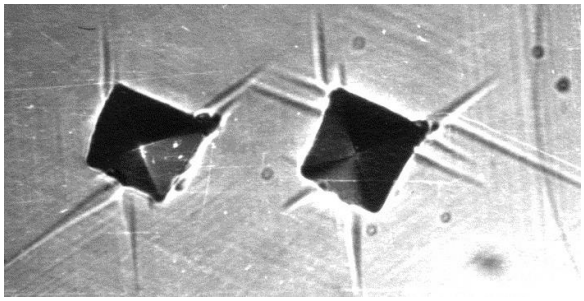

Fig. 1. A photomicrograph of twins on the cleavage plane of bismuth single crystals, x 530. The print on the left was obtained with an indentor load of 10 g. The imprint on the right – with the same load on the indenter, but during deformation through the crystal a current pulse of density 600 A/mm^2.

An increase in the density of total dislocations in the crystal leads to a decrease in volume of twinning and the area of the double.

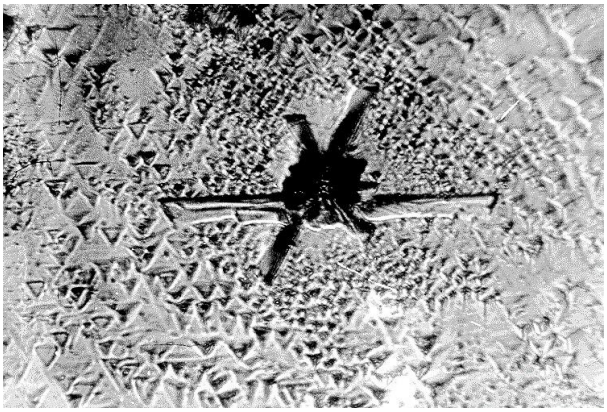

Fig. 2. The etched plane (111) of a bismuth crystal after deformation by a concentrated load. (Load on the indenter 10g; x530)

An increase in the density of total dislocations in the crystal leads to decrease in the volume of twinning and the area of the double boundaries (Fig. 2).

With increasing voltage applied to the crystal during deformation, the range and generation of twinning dislocations increases (Fig. 3). Up to a voltage of 800 V, the excitation processes of dislocation sources are preferable. The increase in voltage leads to the predominance of the following stages in the development of twins: the formation of a surface of separation and the translation of twinning dislocations along the final interface of the twins.

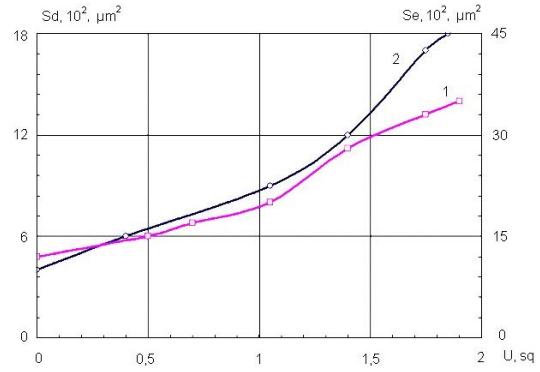

Fig. 3. Run (I) and generation of twinning dislocations (2) on the stress in bismuth crystals:Sd is the area of the twinning interface; Se is the volume of the twin boundaries; U is the electrical voltage applied to the crystal.

If we compare the twins obtained from the action of a concentrated load, and the twins that arise when the load and the electric current pulse are combined, it is easy to see that the ratio of the thickness of the twins at the mouth to their length h/L differs. The ratio h/L characterizes the degree of incoherence of the twin boundaries. If we divide this value by the crystal lattice parameter in the direction perpendicular to the motion of the twinning dislocations a, we obtain the average density of twinning dislocations at the interfaces:

$$\rho_d = \frac{h}{aL}, \tag{1}$$

instead of: a – lattice parameter.

The linear density of twinning dislocations for doubles caused by the combined effect of electrical pulses and mechanical stresses is 10^3-10^4 cm^{-1}, for doubles arising without current pulses, this value is 2-5 times larger (Fig. 2).

As the voltage is increased, the density of the twinning dislocations decreases, i.e. the deviation of the twin boundaries from the twinning plane decreases. With the curvature of the interfaces of twins, brittle fracture is often associated. Cracks in the vicinity of the twin boundaries usually arise when there are significant deviations of the boundaries from the twinning plane. There is a decrease in the degree of incoherence of twin boundaries, and thus there is a density of twinning dislocations at the boundaries; it is primarily a decrease in the thickness of dislocation clusters, a decrease in the role of the double boundaries as concentrators of internal stresses and, as a result, a decrease in the probability of crack formation at the boundaries of twin strips.

The study of a large number of prints shows that the ratio of the load on the indenter to the square of the maximum length of the twin beam in prints is a value close to a constant value. The values of P/L^2_{max} with the change in load almost do not change for crystals of the same composition. P/L^2_{max} has the dimensionality of stresses and characterizes the linear dimensions of the region of the crystal that extends beyond the twinning, so it is natural to assume that this value is proportional to the voltage needed to advance the twinning dislocations in the crystal, thus the quantity P/L^2_{max} can serve as a quantitative characteristic for the plastic deformations are twinning. The ratio P/L^2_{max} is proportional to the stresses at which the motion of the twinning dislocations ceases, when the dislocation at the apex of the twin reaches the regions where the external stress from the concentrated load is balanced by the resistance forces of the crystal lattice, i.e. this is an analog of the yield stress for plastic defor-

DOI 10.2478/ama-2018-0039

mation by twinning. The order of variation of P/L^2_{max} corresponds to the ranges of starting voltages for twinning dislocations in crystals (Stashenko, 2008; Troitskiy, 2008a; Gorelik, 2008; Gorelik and Zlobina, 2008; Samuilov and Troitskiy; 2017).

Fig. 4 shows the dependence of P/L^2_{max} on the current density in the pulse. We can see that P/L^2_{max} values begin to fall at current densities in the pulse of 50-70 A/mm^2 (the threshold values of the electroplastic effect in twinning), then the P/L^2_{max} value decreases significantly and at high current density in the pulse, of the quantity P/L^2_{max}.

If we consider the effect of electric current pulses on the development of twinning, then the P/L^2_{max} values under simultaneous action of external load and current pulse decrease several times, i.e. the transmission of the current pulse at the time of loading of the crystal is accompanied by a significant decrease in the resistance of the crystal lattice to twinning. Thus, the one-time action of the load and electrical impulses makes it possible to plasticize the material further due to twinning. In this case, the electric current pulses increase the share of twinning in the total plastic deformation of the doubling materials, i.e. increase the plasticity reserve.

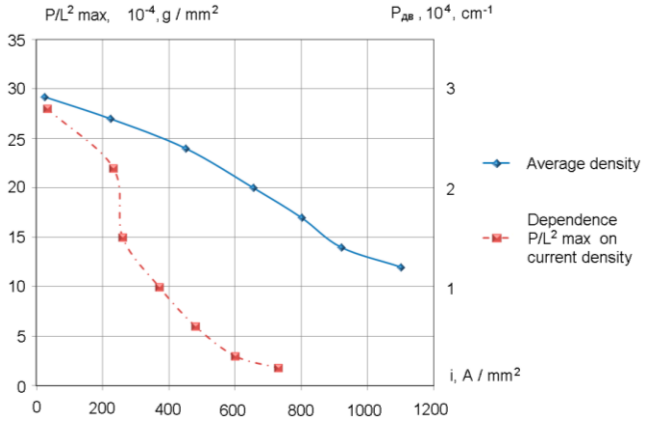

Fig. 4. Dependences of the value of P / L^2_{max} on the current density and the average density of twinning dislocations on the current density in bismuth Bi- 99.99%.

The branching of twins always appears on the curve boundaries where the degree of incoherence of the twin boundaries is the greatest.

Twins usually appear on dislocation clusters and lead to relaxation of internal stresses at the imprint. Up to now, it has been known that relaxation of internal stresses can be achieved by developing slip i.e. in the areas of the crystal adjacent to the twin boundaries (Gorelik and Zlobina, 2008). In this paper for the first time it was discovered that under the action of electrical pulses, the relaxation of internal stresses occurs as a result of the development of new twins, with new twins arising not only on clusters of complete dislocations, but also at the boundaries of the twin interlayers, i.e. on clusters of twinning dislocations what was experimentally and theoretically shown by the author in the work Troitskiy and Savenko (2013). Doubles, emerging at stress concentration sites, discharge dislocation clusters, thereby reducing the likelihood of brittle fracture in the stressed places of the crystal lattice (Fig. 5).

To explain this we use the picture of stress fields in a wedge-shaped twin (Fig. 6), which was obtained on the assumption that the twin boundary consists of complete (Khrushchev et al., 2017; Samuilov, 2017; Surkaev, 2015) rather than partial dislocations. The stress fields around the accumulation of such dislocations, which have the form of a wedge, can be calculated as shown in the formula:

$$\sigma_{xy} = \frac{Gb}{2\pi(1-\nu)}\left\{\sum_{n=0}^{N_1}\frac{(x+nd)[(x+nd)^2-(y+nh)}{[(x+nd)^2+(y+nh)^2]^2} + \right. \tag{2}$$

$$\left. + \sum_{n=0}^{N_2}\frac{(x+nd)\left[(x+nd)^2-(y-nh)^2\right]}{[(x+nd)^2+(y-nh)^2]^2}\right\},$$

where: σ_{xy} –the shear stresses, b –is the Burgers vector modulus, G – is the shear modulus, ν – is the Poisson ratio, n – is the summation index, N_1 and N_2 – are the number of dislocations at the twin boundaries (Troitskity and Savenko, 2013).

In our case, computer-generated curves were taken N_1=N_2=10.

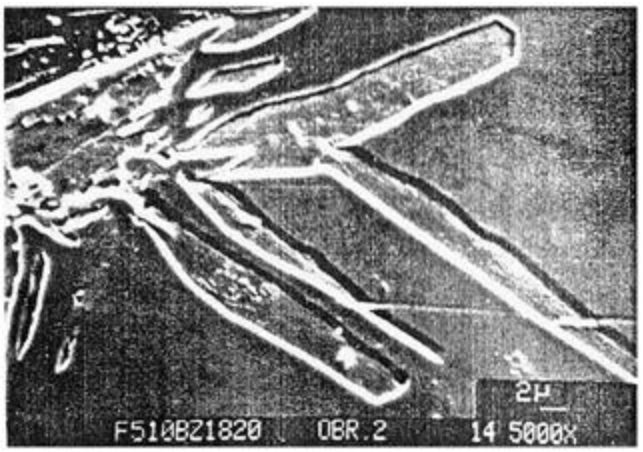

Fig. 5. The branching of a double as a result of the presence of an obstacle in the translation path of twinning dislocations.

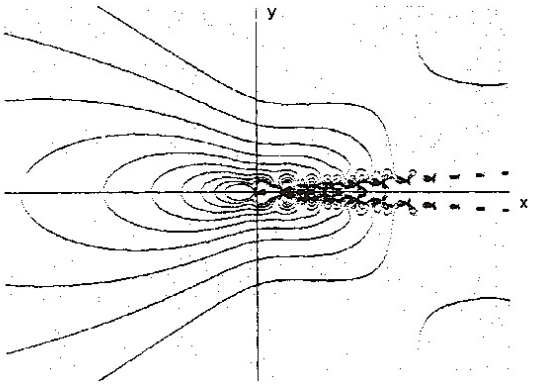

Fig. 6. Stress fields for a wedge-shaped twin.

As it is shown in Fig. 6 the stresses increase with the approach to the twin boundary, moreover, at the double vertex they are of the same order as in the immediate proximity of the twin boundary, but at a distance two or three times larger.

As a result, in the presence of stoppers in the path of motion of the wedge-shaped twin, a redistribution of the stresses at its vertex occurs in such a way that the magnitude of their projections to a new twinning direction becomes comparable with the threshold value of the appearance of the twin.

DOI 10.2478/ama-2018-0039

The growth of the density of complete dislocations makes twinning difficult.

In authors'opinion, consideration of the most probable mechanisms of the influence of electromagnetic fields on the plastic deformation of metals should be carried out with due regard to the state of the surface of the crystal, since the excitation of the electronic subsystem of the crystal by an electromagnetic field leads to a change in its surface energy. In deformation processes, moving dislocations, interacting with a free surface, acquire excess free energy, become unstable and tend to reach the surface of the crystal (Skal, 2013; Krajewski et al., 2012).The edge dislocation is attracted to the surface by the force of the "mirror image", which is determined by the slowly varying logarithmic potential. At the same time, the output of dislocation to the surface is accompanied by the appearance of a characteristic step. In this case, energy is created to create a new cellγb^2 where $\gamma$is the surface energy. This force is distributed deep into the crystal by a half-width of a dislocation of the order of several b, and in the immediate vicinity of the surface it can predominate over the "mirror image" force. Therefore, a decrease in the surface energy of the metal will facilitate the release of dislocations of the same sign onto the surface and lead to an increase in the rate of plastic deformation and a decrease in the deformation hardening. At the same time, the increase in surface energy intensifies the work of surface sources of dislocations by compensating for the "mirror image" force.

Dislocation is a linear defect only from the point of view of distortion of the electronic structure of the material, which is formed on the edge of the superfluous half-plane. It is to be expected that bound electronic states arise here, whose energy spectrum and the corresponding wave functions differ from the energy spectrum and the wave functions of the external valence electrons of a defect-free crystal lattice.

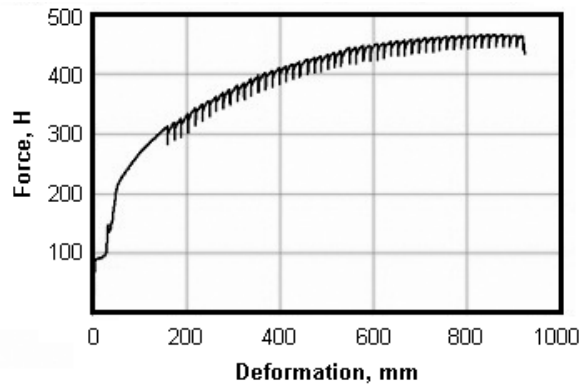

Fig. 7. Dependence of the statistical force applied to the sample on the magnitude of deformation up to the moment of its destruction. Stainless steel under the influence of current pulses

The excitation of the electronic subsystem of the current pulse metal, when electroplasticity is realized in a metallic sample loaded above the yield point, leads to the appearance of additional deformation processes due to the oscillations of the deforming forces, ponderomotive effects occur during the deformation processes (Fig. 7) which cause vibroacoustic ultrasonic vibrations of the crystal lattice in different crystallographic directions (Fig. 8) (Troitskity and Savenko, 2013; Khrushchev et al., 2017) due to the appearance of dynamic pin - and the skin effect.

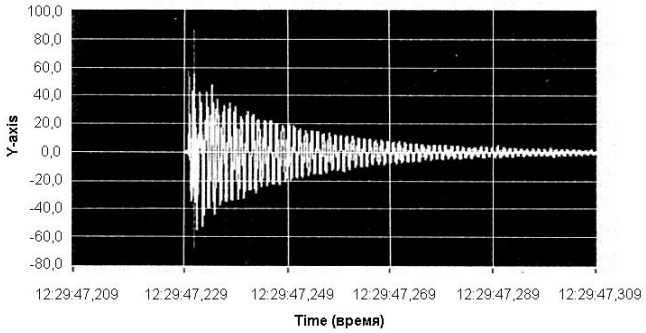

Fig. 8. Transient processes of ultrasonic acoustic vibration from the action of current pulses under strain conditions above the yield point.

If we consider the "ionic", "covalent", "metallic" bonds from the point of view of the distribution of the wave functions of the external valence electrons, then there is a clear tendency to delocalization of wave functions and an increase in the degree of their overlap. In this vein the greater overlap of the wave functions of the valence electrons of the atoms composing the crystals and the electronic states at the dislocations, the more plastic is the given material. The excitation of the electron subsystem of the crystal leads to an overlap of the wave functions in the dislocation core and to an increase in its mobility. The introduction into the impurity crystal where the wave functions of the valence electrons are delocalized, it reduces the shear stresses and, as a result, facilitates the process of plastic deformation is observed.

Under the influence of the intrinsic magnetic field of the current, which envelops the conductor (a deformable sample) with annular lines, polarization of the electronic subsystem of the metal arises and, as a result, the appearance of a transverse electric Hall field that prevents further compression of the electron plasma.

Consider the equation $\frac{\partial \mathrm{H}}{\partial \mathrm{t}} = \frac{\mathrm{c}^2}{4\pi\sigma\mu\nabla^2\mathrm{H}}$, which agrees with the diffusion equation $\frac{\partial n}{\partial t} = D\nabla^2 n$.

Choosing the projection on the Z-axis, we write in the form:

$$\frac{\partial H_Z}{\partial t} = \partial M \frac{(\partial^2 H_Z)}{\partial x^2}, \tag{3}$$

where: $\partial \mathrm{M} = \frac{\mathrm{c}^2}{4\pi\sigma\mu}$ – coefficient of magnetic diffusion, c – electrodynamic constant, μ – magnetic permeability, σ – specific conductivity.

Since, the field outside the sample varies according to the harmonic law, the following Z projection of the magnetic field inside the sample will be:

$$H_Z(0,t) = H_0 \cos(\omega t), \tag{4}$$

where magnetic field strength on the boundary, for $x = 0$. The harmonic dependence (3) characterizes the so-called stationary skin effect (Troitskiy, 2008a).

Since equation (2) is linear and contains real coefficients, the following calculations can be simplified by going over to complex writing. Thus, we seek a solution of another auxiliary problem with the replacement of $\cos(\omega t)$ by a complex exponent:

$$H_Z(0,t) = H_0 e^{(-i\omega t)}. \tag{5}$$

The solution of the original problem with a real field can be obtained from the solution of the auxiliary problem with a complex

DOI 10.2478/ama-2018-0039

field by separating the real part. Since the magnetic field outside the sample is proportional to$e^{-i\omega t}$,we assume that the solution of the auxiliary problem should be sought in the following form:

$$H_Z(\mathrm{x},t) = H(x)e^{(-i\omega t)}. \quad (6)$$

Substituting this dependence (4) in the partial differential equation (2), we can obtain the ordinary differential equation (3):

$$\frac{\partial^2 H}{\partial x^2} = -\frac{2i}{\delta^2}H, \quad (7)$$

where: $\delta = \sqrt{\left(\frac{2D_M}{\omega}\right)} = \frac{c}{\sqrt{2\pi\sigma\mu\omega}}$has the dimension of length.

The general solution of an ordinary differential equation of the second order with constant coefficients is in the form of a sum of exponentials $\mathrm{Ae}^{\mathrm{ikx}}$ with constant coefficients A and k^2.The coefficientkis found by substitution $\mathrm{e}^{\mathrm{ikx}}$ into equation (6).The algebraic equation $k^2 = \frac{2i}{\delta^2}$, hastworoots $k = \pm\frac{(1+i)}{\delta}$.

One of them, $(k+)$ corresponds to the decreasing, and the other$(k\ -)$ to the alternating magnetic field, which grows to the axis of the sample (as $x \to \infty$) to the alternating magnetic field. The radially increasing magnetic field should be omitted, since it corresponds to a meaningless increase in the magnetic field up to an infinite value when moving away from the source. Thus, within the conductor the solution of the auxiliary problem has the form:

$$H_z(x,t) = Ae^{-\left(\frac{(1-i)x}{\delta}\right)}e^{(-i\omega t)}. \quad (8)$$

The coefficient A can be found from the condition of continuity of the tangential projection of the magnetic field strength at the sample boundary at $x = 0$.Since the strength of the magnetic field varies outside the conductor at $\mathrm{x} = 0$ according to the law $H_z(0,t) = H_0e^{-i\omega t}$, we conclude that $\mathrm{A} = H_0$. Consequently,

$$H_z(x,t) = H_0e^{-\left(\frac{(1-i)x}{\delta}\right)}e^{(-i\omega t)}. \quad (9)$$

Defining the real part of the complex function $\mathrm{H_Z(x,t)}$, we find the real magnetic field in the sample:

$$H_Z(x,t) = H_0e^{-\frac{x}{\delta}}cos\left(\omega t - \frac{x}{\delta}\right), \quad (10)$$

where: δ – thickness of the skin layer (Troitsky, 2007; Savenko, 2017; Savenko et al., 2017).

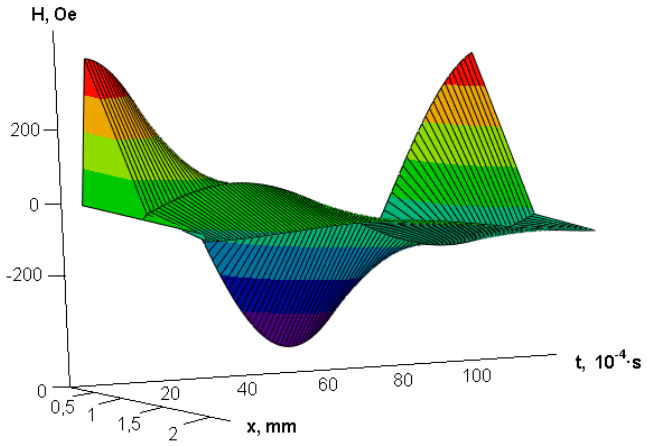

Fig. 9. The change in the magnetic field in a sample of magnesium at $\nu = 600Hz$

To determine the value of the magnetic field arising from ponderomotive factors during electroplastic deformation by 35 transition rolling of magnesium samples, we use the MathcadProfessional program, taking into account the final parameters of the last transition of deformation magnesium: $\mathrm{s} = 4\ \mathrm{mm}^2$ – cross-sectional area of the sample, $\mathrm{r} = 2\ \mathrm{mm}$ – sample cross-section radius, $\mathrm{j} = 10^3\ \frac{\mathrm{A}}{\mathrm{mm}^2}$ – current density, pulse duration $\tau = 10^4\mathrm{s}$, frequency $\nu = 600\ \mathrm{Hz}$, $\sigma = 22{,}7 \times 10^3\ \mathrm{cm/mm}$ – conductivity of magnesium.

As we can see in the graph (Fig. 9) a change in the magnetic field is observed in the sample of deformation magnesium with final parameters at the last transition.

The intensity of the magnetic field increases while moving from the center to the sample surface and it reaches the value H=400 Oe (31830 A/m) being at a distance of 1 mm from the center of the cross section of the sample, the magnetic field strength is H=100 Oe(7957A/m).

3. CONCLUSIONS

1. Electron-plastic deformation stimulates the formation of the interface, and the translation of the twinning dislocations along the finished interface, increases the range and generation of twinning dislocations which opens the possibility of additional plasticization of the twinning material, increasing the share of twinning in the total plastic deformation, thereby increasing the plasticity reserve of the doubling materials.
2. The twinning in the region of twin boundaries leads to an intense multiplication of the twinning dislocations and to the collective interaction of the screw components of the twinning dislocations with an obstacle, which opens up new channels for the realization of twinning.
3. Excitation of mechanical twinning by external field not only influences plasticizes, but also increases the real strength of the material. The stimulation of twinning by current pulses leads to a decrease in the density of twinning dislocations at the interfaces of mechanical twins, equalization of their dislocation structure, acceleration of stress relaxation processes, which reduces the probability of brittle fracture in the region of twin boundaries.
4. The electric charge arising on the surface of the sample as a result of the Hall polarization facilitates the operation of dislocation sources and stimulates the translation of twinning dislocations along the finished interfaces, leads to a partial discharge of long-range elastic stresses in clusters of twinning dislocations and the appearance of new channels for realizing the process of plastic deformation by twinning.

REFERENCES

1. **Gorelik V. S., Zlobina A. I.** (2008), Spectra of secondary radiation of opal matrices filled with silver nanoparticles obtained by fiber-optic excitation, *Inorganic material*, 44, 7, 6–9.
2. **Gorelik V.S.** (2008), Excitation by semiconductor LEDs secondary radiation in opals with pores filled with silver nanoparticles, *Inorganic material*, 44, 1, 1–4.
3. **Gorelik, V. S., Zlobina A. I., Chanieva R. I.** (2008), Spectra of secondary radiation of opal matrices filled with silver nanoparticles obtained by fiber-optic excitation, *Inorganic material*, 44(7), 6–9.

DOI 10.2478/ama-2018-0039

4. **Khrushchev M.M., Troitskiy O.A., Stashenko V.I., Levinl.S.** (2017), Change in the phase composition of steel under the influence of current pulses and microwave radiation under deformation, *Ferrous metallurgy,* 7, 82–87.
5. **Khrushchev M.M., Troitskiy O.A., Stashenko V.I., Levinl.S.** (2017), The Effect of current pulses and microwave radiation on the phase composition of steel under deformation, *Mechanical engineering and engineering education*,1, 50–56.
6. **Krajewski, A.,Włosiński W., Chmielewski T., Kołodziejczak P.** (2012), Ultrasonic-vibration assisted arc-welding of aluminum alloys, *Bulletin of the Polish Academy of Technical Sciences,* 60 (4), 841–852.
7. **Samuilov S.D.** (2017),Electroplastic compaction (briquetting) of dispersed conductive materials for recycling waste of high-strength alloys, obtaining blanks, semi-finished products, materials and products with a new level of properties, *Fundamental and applied problems of engineering and technology,*4(324), 83–89.
8. **Samuilov S.D.,Troitskiy O.A.** (2017), New methods of production of porous metal materials with closed and open porosity, *Fundamental and applied problems of engineering and technology,* 3(323), 12–16.
9. **Savenko V.S.**(2017), The contribution of ponderomotive factors to the realization of electroplastic deformation / V.S. Savenko, O.A. Troitsky, A.G. Silivonets // Izvestiya NAN RB,*A series of physical and technical sciences*, 1, 85–91.
10. **Savenko V.S., Silivonets A.G., Gunenko A.V.** (2017), Calculation of current density and magnetic field strength inside a conductor under conditions of electroplasticity, *Vesnik of the Polotsk State University, Series C. Fundamental sciences,*4,72–78.
11. **Savenko V.S.,Troitskiy O. A., Gunenko A.V.** (2018), Physical Aspects of Electroplastic Deformation of Metals, *Vesnik of the Brest University*, 1, 40–48.
12. **Skal A.S.** (2013), The full Lorentz force formula responsible for turbulence in solids and fluids and explained Faraday's paradox, *International Journal of Scientific & Engineering Research*, 4(2), 10–14.
13. **Stashenko V.I.** (2008), Electroplastic drawing of medium carbon steel, *Problems of mechanical engineering and reliability of machines,* 6, 12–14.
14. **Stashenko V.I., Troitskiy O.A., Novikov N.N.** (2008), Electroplastic drawing of iron wire, *Problems of mechanical engineering and reliability of machines,* 5, 32–38.
15. **SurkaevL.** (2015), Magnetohydrodynamic perturbations arising in metallic conductors under the action of the discharge current, *Technical Physics*,60(7), 981–993.
16. **Troitskiy O.A.** (2007), Influence of current Pulse count in Pulse Train and time Lag Between Pulses on the Electroplastic metal Deformation, *Symposium China-Rassia "Elektroplastic effect in metals"*,China, 28–32.
17. **Troitskiy O.A.** (2008), Electronic mechanisms of electroplastic deformation of metals, *Deformation and fracture of materials*, 5, 41–44.
18. **Troitskiy O.A.** (2008), Inertial effect of the Stewart-Tolman for high-speed wire drawing and the collision of the bullet with the target, *Problems of mechanical engineering and reliability of machines*, 9, 29–34.
19. **Troitskiy O.A.** (2016), *Physical and technological basis of electro-plastic deformation of metals*, MGPU, Mozyr.
20. **Troitskiy O.A., Savenko V.S.** (2013), *Fundamental and applied researches of electroplastic deformation of metals: monograph*, Ministry of Finance ITC, Minsk.

sciendo

DOI 10.2478/ama-2018-0040

acta mechanica et automatica, vol.12 no.4 (2018)

OPTIMIZING SAMPLING PARAMETERS OF CMM DATA ACQUISITION FOR MACHINING ERROR CORRECTION OF FREEFORM SURFACES

Małgorzata PONIATOWSKA*

*Faculty of Mechanical Engineering, Bialystok University of Technology, ul. Wiejska 45 C, 15-351 Bialystok, Poland

m.poniatowska@pb.edu.pl

received 21 May 2018, revised 27 October 2018, accepted 31 October 2018

Abstract: An optimization study using the design of experiment technique is described, in which the surface profile height of a freeform surface, determined in coordinate measurements, is the response variable. The control factors are coordinate sampling parameters, i.e. the sampling grid size and the measuring tip diameter. As a result of the research, an optimal combination of these parameters was found for surface mapping with acceptable measurement uncertainty. The presented study is the first stage of optimization of machining error correction for the freeform surface and was intended to take into account mechanical-geometric filtration of surface irregularities caused by these geometrical parameters. The tests were carried out on a freeform workpiece milled with specific machining parameters, Ra of the surface roughness was 1.62 μm. The search for the optimal combination of parameters was conducted using Statistica software.

Key words: Freeform Surface, Machining Error Correction, Coordinate Measurement, Measurement Parameters, Design of Experiment Technique

1. INTRODUCTION

Objects with freeform surfaces are more and more often designed for functional and aesthetic reasons. The complex geometries of such surfaces are challenging both at the manufacturing stage and at the accuracy assessment stage.

The first step in accuracy assessment of freeform surfaces is to map the actual geometry with the use of a cloud of points. For that purpose, coordinate measuring machines (CMMs) with ball-tip touch probes are usually used (Savio et al., 2007; Sładek, 2016).

Numerically controlled CMMs make it possible to generate the path of automatic movement of the touch probe, i.e. to generate nominal points on the CAD model, according to the adopted criterion. The distribution and number of these points are called the sampling strategy. The complete measurement plan involves also configuration of the measuring probe set, i.e. the orientation and length of the stylus, and also the ball tip diameter.

In coordinate measurements of freeform surfaces, local deviations at the measurement points, i.e. normal deviations of the measurement points from the nominal surface represented by the CAD model, are determined. These deviations may be the basis for determining geometric deviations or corrections compensating machining errors. Both of these applications require a complete knowledge of the surface. However, information on surface irregularities depending on the adopted measurement parameters – the sampling step and probe tip diameter – are separated as early as at the sampling stage, because both these factors cause mechanical-geometric filtration of irregularities (Adamczak et al., 2010; Rajamohan et al., 2011a, 2011b). Rajamohan et al. (2011b) in their calculations included the contact error resulting from the surface curvature for the specified probe tip size in the performed computer simulations of various sampling strategies. Moreover, they observed the effect of mechanical-geometric filtration bringing about minimising of the observed surface deviation in measurements with the use of a ball with a bigger diameter.

It is assumed that measurement points faithfully represent measured surfaces. However, measurement results are always burdened with uncertainty. One of the reasons for measurement uncertainty, in addition to the contributions of measuring equipment, workpiece geometry and measurement conditions, is the sampling strategy (Mehrad et al. 2013; Moroni and Petro, 2014; Weckenmann et. al., 2004) whose influence is entirely dependent on the metrologist. An unreasonable strategy planning can be the largest uncertainty contributor. Considering the measurement time, the number of points should be as low as possible, while larger numbers of points characterise surfaces more accurately. Therefore, a strategy is intensely searched for in which the number of points would be as low as possible, and their distribution would enable an efficient surface mapping with an acceptable measurement uncertainty. In the area of accuracy assessment, different sophisticated methods for distributing points, both on geometric primitives and freeform surfaces, are used. Some of the researchers pay more attention to the number of points, whereas others focus on the distribution of measurement points (Moroni and Petro, 2014; Poniatowska, 2012; Obeidat and Raman, 2009). In the application to the correction of machining errors, the only solution is to measure according to the regular grid of points, as in reverse engineering, but in this case measurements are based on the CAD model.

In this paper, in search of the optimal combination of sampling parameters research was conducted using the DOE (Design of Experiments) technique. This technique may be applied to solving problems related to the manufacturing and measurement processes, in order to change these processes and to understand the influence of different factors on the final process or product quality

(Karaszewski and Skrzypczyńska, 2013; Kowalczyk, 1995). DOE is an experimental technique that helps to investigate (design) the best combinations of process parameters, changing quantities, levels, and combinations, in order to obtain statistically reliable results. It is a way that may be followed so as to find solutions to process problems with greater objectivity by means of experimental and statistical techniques. In the work, the loss of measurement process quality, caused by applying various combinations of sampling parameters, was investigated.

In the literature of the art, many researchers sought for optimal measurement parameters and uncertainties, both in touch measurements (Feng et al., 2007; Moroni and Petro, 2014) and non-touch measurements (Al-Ahmari and Aalam, 2015), including applying DOE techniques (Al-Ahmari and Aalam, 2015; Barini et al., 2010, Feng et al. 2007)). The influence of many parameters was taken into account, such as: measuring speed, stylus length, number of points and measuring distances.

The tests described in the present paper were carried out on a milled freeform surface classified by Savio et al. (2007) as a surface of medium shape complexity characterised by moderate to large curvature changes. The problem of selecting surface sampling parameters – the tip diameter and the point grid size – for surface irregularities mapping with acceptable measurement uncertainty, has been solved. The presented study is the first stage of optimization of the machining error correction for the surface of an injection mold and was intended to take into account mechanical-geometric filtration of surface irregularities caused by these geometrical parameters. The effect of parameters causing geometric-mechanical filtration depends on surface topography. The tests were carried out on the workpiece milled with specific machining parameters, Ra of the freeform surface roughness was 1.62 μm. The solution should be treated as a task specific with the possibility of applying to milled surfaces with a similar curvature and roughness.

2. APPROACH DESCRIPTION

In designing the coordinate sampling parameters, the Taguchi method was applied. It is one of the methods that can be used successfully in DOE. The basic notion in the described method is the quality loss function applied in quality loss assessment and dependent on the adopted quality characteristics (Karaszewski and Skrzypczyńska, 2013).

According to Taguchi, the parameters which exert great influence on the measurement and manufacturing process can be adjusted to varying levels so that some settings can result in the robustness of the process (Karaszewski and Skrzypczyńska, 2013; Kowalczyk, 1995).

Control factors are the selected independent variables of the experiment, which have different effects on the response variables when adjusted to different levels, in this case – the sampling grid size and probe diameter.

Factor levels are the intensity to which the control factors are adjusted in a particular experiment. They can be identified as low level, intermediate level, and high level.

Response variables are the dependent variables which change when they go through different process parameters. In the experiments, there may be one or more response variables, in this case – the surface profile height of a freeform surface, determined from local deviations at the measurement points.

Noise factors are the variables which influence the response variables. They may or may not be known. Special care should be taken to prevent noise factors from interfering in the experimental results.

Treatments: each experimental run is a treatment, that is, a combination of factor levels, in this case – the combination of sampling parameters.

Experimental matrix is the matrix composed of control factors with different levels for each treatment given.

Repetition is the reproduction of the selected combination under the same experimental conditions. Repetition makes it possible to estimate the experimental error that is used to define whether the differences in the control variables are significant.

According to the approach used in the Taguchi method, to measure the process quality, minimisation of the changeability of this process in response to the *N* noise factors should be adopted, with simultaneous maximization of the changeability in response to the S signal factors. Combining the two criteria, the ratio of the signal to the noise $\eta = S/N$ is obtained. It should be noted that *S/N* is reversely proportional to the quality loss function. This means that as *S/N* increases, the quality improves and loss is minimised. The way in which η is expressed differs depending on the optimization problem concerned. In practice, three types of the η coefficient are applied:

– the 'nominal is the best' characteristics

$$\eta = \frac{S}{N} = 10 \log \frac{\bar{y}}{S^2}, \tag{1}$$

– the 'smaller is the better' characteristics

$$\eta = \frac{S}{N} = -10 \log \frac{1}{n} \sum y^2, \tag{2}$$

– the 'larger is the better' characteristics

$$\eta = \frac{S}{N} = -10 \log \frac{1}{n} \sum \frac{1}{y^2}, \tag{3}$$

where: y – observed data or each type of characteristics, $\bar{y}$ – the average of observed data, S – signal factors, N – noise factors, η – signal to noise ratio, n – the number of repetitions.

In touch measurements, the probe tip acts like a mechanical-geometric filter. It means that the range of information included in the measurement data is related to the probe tip size. In the presented experiments, an attempt to assess the influence of the sampling parameters on the height of the determined irregularities was made. It was assumed that the *H* height of the surface profile (a response variable), i.e. the sum of the absolute value of the biggest *min.* and *max* local deviations is the value that best represents the level of mapping of the actual surface in the measurement process. The reason for that is the different operation of the probe tip on peaks and in valleys of irregularities, in particular, the valley detection error of the probe tip due to its size (Fig. 1).

In the performed optimization tests, the *H* of the surface profile with various combinations of control factors was determined. The influence of the following control factors on the measurement results: (1) the *d* diameter of the ball tip, and (2) the $s \times s$ grid size was investigated. Four ball tips of the diameters of 1, 2, 3, and 4 mm, typically applied in coordinate measurements, were used. The freeform surface measurements were taken under the same conditions and along a regular grid of points, using different combinations of the *d* and $s \times s$ parameters. The $s \times s$ sampling grid sizes, with the *s* values of 0.25; 0.5; 1, and 2 mm were selected.

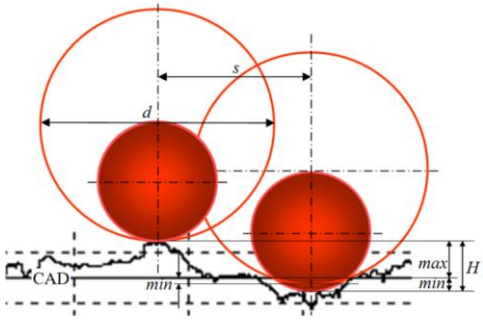

Fig. 1. The nature of a ball tip functioning in the character of a mechanical-geometric filter

The freeform surface of the workpiece on which the tests were performed was previously calibrated in an accredited calibration laboratory using the tip d = 2 mm and grid size (1 × 1) mm. This knowledge on the surface was used in the experiment. However, to determine only the effect of the parameters causing the mechanical-geometric filtration, and to take into account the smaller parameters d and $s \times s$, as the 100% process quality, the arithmetic mean of the profile height from 5 repetitions for the ball tip of the smallest diameter d = 1 mm, and the sampling grid (0.25 × 0.25) mm was adopted. All tests were carried out under the same experimental conditions. According to literature data, in general, larger sampling parameters are used in data acquisition for machining error correction (e.g. Chena et al., 2013, Chen et al., 2018)). Chena et al. (2013) used data obtained from measurements on a machine tool applying the ball tip of 6 mm and (3.5 × 3.5) mm, while Chen et al. (2018) carried out their measurements on CMM with the tip of d = 5 mm and $s \times s$ = (4 × 4) mm. The question is: what values of these parameters should be used to ensure effective freeform surface mapping? According to the Taguchi method approach, the loss of the measurement process quality, caused by applying higher measurement parameters (the d and $s \times s$ control factors), was investigated. The process quality loss (the Δ loss of the information on the surface irregularities) was represented by the difference between the profile H for a given combination of the control factors and the H representing 100% of the process quality.

The experiment included 16 treatments with 5 repetitions. The control factors combinations used in the experiment are presented in Fig. 2.

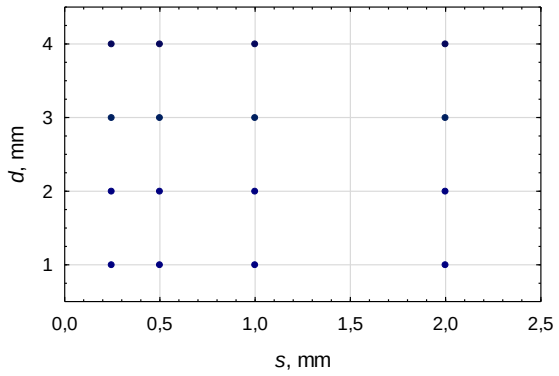

Fig. 2. Experimental matrix

The experiment plan was developed with STATISTICA software, using the option 'planning experiments according to the Taguchi method' (orthogonal tables). The 'smaller the better' characteristics was selected. This characteristics is applied when minimising undesirable characteristics is needed.

3. EXPERIMENTAL RESEARCH

3.1. Data acquisition

The measurements described in this paper were carried out on a Global Performance CMM (with PC DMIS software), (Maximumm Perissible Error) $MPE_E = 1.5 + L/333$ [µm], equipped with a Renishaw SP25M probe and a 10 mm stylus with a ball tip. The measurement uncertainty for the form deviation with reference to datum features, estimated using EMU software developed at University of Bielsko-Biala (the author – W. Jakubiec) (Jakubiec et al. 2012), was equal to U = 0.9 µm. The experiment was performed on a freeform surface of a workpiece made of WCLV steel with the base measuring (50 × 50) mm, obtained in the milling process using a ball-end mill of 6 mm in diameter, with the rotational speed equal to 8000 rev/min, the working feed of 800 mm/min, and a zig-zag cutting path in the XY plane (Fig. 3, Ra = 1.62 µm). Fig. 3 shows an example of the point distribution on the measured surface.

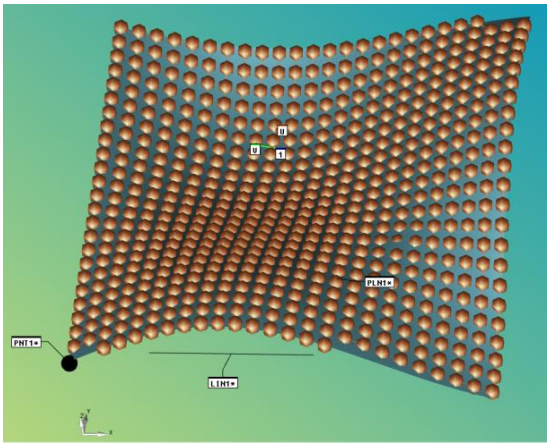

Fig. 3. Distribution of measurement points on CAD model in PC DMIS software, measurement parameters d = 2 mm, $s \times s$ = (2 × 2) mm

3.2. Results and discussion

Pursuant to the Taguchi theory, the quality of the investigated process increases with the increase of the η coefficient. In order to illustrate the trend of the signal-to-noise ratio, graphs of the main effects, showing the effect of each control factor on the response variable, are created. In the described experiment, the H determined for the measurement parameters of $s \times s$ = (0.25 × 0.25) mm and d = 1 mm was adopted as 100% of the process quality. The mean values of the main effects can be seen in Fig. 4.

While analysing the graphs (Fig. 4), it can be observed that the η value decreases more rapidly for the ball tip diameter than for the sampling step. It means that increasing the d parameter has a greater impact on the process quality loss, in this case – on the loss of the information on the surface profile height.

While analysing the η values for the particular combinations of the $s \times s$ and d parameters (Fig. 5) we can see that we obtain a similar process quality loss for some combinations of these

DOI 10.2478/ama-2018-0040

parameters. For example, for d = 3 mm and $s \times s$ = (0.5 × 0.5) mm, the η value is 49.1, while for d = 1 mm and $s \times s$ = (1 × 1) mm the η value equals 49.7. This means a similar loss of information about surface irregularities for a smaller number of measurement points for d = 1 mm and $s \times s$ = (1 × 1) mm. In this case, the numbers of the measurement points are 10,000 and 2,500, respectively. Similarly, for d = 1 mm and $s \times s$ = (2 × 2) mm, the value of η = 45.8 is similar to the value of η = 45.1 for the combination of d = 3 mm and $s \times s$ = (1 × 1) mm, and to the value η = 45.0 for the combination of d = 4 mm and $s \times s$ = (0.25 × 0.25) mm. In this case, the numbers of the measurement points are 625, 2 500 and 40 000, respectively.

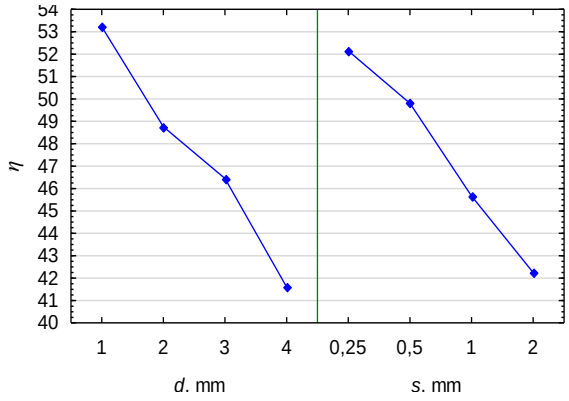

Fig. 4. Mean values of η of main effects

In the graphs (Fig. 5) it can be observed that changing the sampling grid for the constant diameter value of the ball tip for d = 3 mm and d = 4 mm affects the process quality to a lesser extent (with a small increase in η) than in the case of ball tips with d = 1 mm and d = 2 mm. At the same time, it can be seen that the use of the ball with d = 4 mm for all the applied $s \times s$ values results in an exceptionally low quality of the measurement process. It is caused by strong mechanical-geometric filtration of the surface irregularities, which indicates that in the measurement practice, in geometric accuracy assessment, ball tips of this size shall not be used. Using ball tips with d = 2 mm and d = 3 mm yields similar process quality for the same $s \times s$ values. A significantly better measurement process quality is obtained in measurements for which the ball tip with d = 1 mm is applied. In connection with the above findings, Fig. 6 presents charts illustrating the absolute value of the Δ loss of information on the H of surface profile for the ball tips with d = 1 mm and d = 2 mm. The estimates of the experimental errors are included to show that the differences in the control variables are significant (Chapter 2).

In evaluating the acceptable measurement uncertainty, the principle as in the accuracy assessment was adopted. Accuracy assessment and machining process are performed according to a given geometric specification. Acting in accordance with the rules for proving conformity or nonconformity with the specifications defined in the relevant standards (ISO 14253-1:2014; ISO 14253-2:2011), and using the charts in Fig. 5 and Fig. 6, it is possible to select the optimal combination of sampling parameters so that – after including the influence of these parameters in the uncertainty budget (Sładek, 2016; ISO/IEC Guide 98-3:2008, Uncertainty of measurement – Part 3: Guide to the expression of uncertainty in measurement) – the measurement is efficient. In industrial applications, the ISO 9000 series of standards for quality management systems are used for determining the acceptable measurement uncertainty. In some industry sectors, internal directives on quality management consisting of an examination of the measurement process capability are applied (Sładek, 2016; Dietrich and Schulze, 2000). To confirm the capability of the measurement process, the measurement uncertainty must be known and it must remain within an acceptable relation to the corresponding tolerance of a controlled feature of the part under question.

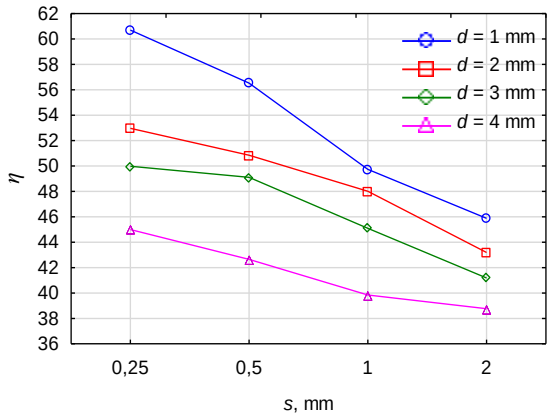

Fig. 5. Values of η ratio for all combinations of s and d parameters

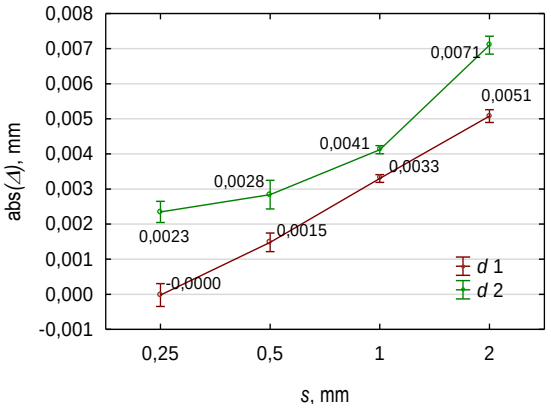

Fig. 6. Loss of information on surface profile height for ball tips with diameters d = 1 mm and d = 2 mm

Tab. 1. The examples of selected measurement uncertainties for various combinations of measurement parameters

Form tolerance [μm]	Uncertainty limit [μm]	abs(Δ) [μm]	Measurement uncertainty [μm]	Measurement parameter combination (*optimal)	
				d [mm]	*s* [mm]
20	2.0	1.40± 0.41	1.3	1	0.5
		2.22 ± 0.34	1.6	2	0.25
		2.83 ± 0.40	1.9	2	0.5
		3.31 ± 0.02	**2.0**	**1**	**1**
		4.19 ± 0.15	2.6	2	1

In this study, parameters were sought for efficient mapping of the freeform surface of the injection mold with a form tolerance

of 0.02 mm. In accordance with the documents mentioned above the measurement process may be considered as capable if the measurement uncertainty does not exceed 2.0 μm. This means that under laboratory conditions, for the form deviation measurement uncertainty of 0.9 μm (Section 3.1), taking into consideration the Δ loss resulting from the applied measurement parameters and their statistical error (Fig. 6, Tab. 1), as well as statistical error of the reference value, the optimal combination of measurement parameters to this task is the combination of d = 1 mm and $s \times s$ = (1 × 1) mm (the measurement uncertainty in this case amounts to 2.0 μm for coverage factor equal 2).

4. CONCLUSIONS

While taking measurements on CMMs for freeform surfaces mapping, the sampling parameters should be rationally selected so that the measurement process is efficient – that is, so that it makes it possible to map the surface irregularities for the smallest possible number of measurement points. In search of the optimal combination of the sampling parameters to data acquisition for machining error correction, the DOE experimental and statistical techniques were applied. The performed optimization experiments described in the present paper provided information on the influence of the coordinate sampling parameters – the d ball tip diameter and the s × s grid size – on the loss of the measurement process quality. The loss of information on the height of the surface profile, included in the measurement data, was investigated. The experiments showed that the ball tip diameter is the parameter that affects the results most. Styluses with ball tips of d = 4 mm cause such great loss of the process quality that they should not be used in surface irregularities mapping. Using the presented test results, and with the specified, acceptable contribution of the influence of the parameters in the measurement uncertainty budget, it is possible to select their optimal combination with respect to the geometric specification. In the presented experiment, for the freeform surface of an injection mold with a form tolerance of 0,020 mm, the optimal combination of measurement parameters, to keep the measurement uncertainty at the acceptable level, is d = 1 and $s \times s$ = (1 × 1) mm.

REFERENCES

1. **Adamczak S., Janecki D, Makieła W., Stępień K.** (2010), Quantitative comparison of cylindricity profiles measured with different methods using Legendre-Fourier coefficients, *Metrology and Measurement Systems* XVII, 233-244.
2. **Al-Ahmari A.M.A., Aalam J**. (2015), Optimizing parameters of freeform surface reconstruction using CMM, Measurement, 64, 17-28.
3. **Barini E. M., Tosello G., De Chifre L.** (2010) Uncertainty analysis of point-by-point sampling complex surfaces using touch probe CMMs. DOE for complex surfaces verification with CMM, Precision Engineering, 34, 16-21.
4. **Chen Y., Tang H., Tang Q.,, Zhang A., Chen D., Li K.,** (2018), Machining error decomposition and compensation of complicated surfaces by EMD method, *Measurement*, 116, 341-349.
5. **Chena Y., Gaoa J.,, Deng H., Zhenga D., Chena X., Kelly R**. (2013), Spatial statistical analysis and compensation of machining errors for complex surfaces, Precision Engineering 37, 203–212.
6. **Dietrich E., Schulze A.** (2000), *Statistical methods in qualification of* measuring devices of machines and processes, Notika System, Warsaw (in Polish).
7. **Feng C-X, Saal A. L., Salsbury J. G., Ness A. R., Lin G. C. S.** (2007) Precision Engineering, 31, 94-101.
8. **ISO 14253-1:2014**, Geometrical product specifications (GPS) – Inspection by measurement of workpieces and measuring equipment – Part 1: Decision rules for proving conformity or nonconformity with specification.
9. **ISO 14253-2:2011**, Geometrical product specifications (GPS) – Inspection by measurement of workpieces and measuring equipment – Part 2: Guidance for the estimation of uncertainty in GPS measurement, in calibration of measuring equipment and in product verification.
10. **ISO/IEC Guide 98-3:2008**, *Uncertainty of measurement – Part 3: Guide to the expression of uncertainty in measurement* (GUM:1995).
11. **Jakubiec W., Płowucha W., Starczak M.** (2012), Analytical estimation of coordinate measurement uncertainty, *Measurement*, 45, 2299-2308.
12. **Karaszewski R., Skrzypczyńska K.** (2013), *Quality management,* TNOiK, Toruń (in Polish).
13. **Kowalczyk J.** (1995), *Quality management –Taguchi Method*, Bellona, Warsaw (in Polish).
14. **Mehrad V., Xue D., Gu P**. (2013), Prediction of surface reconstruction uncertainties for freeform surface inspection, *Measurement* 2013, 46, 2682-2694.
15. **Moroni G., Petrò S.** (2014), Optimal inspection strategy planning for geometric tolerance verification, *Precision Engineering*, 38, 71-81
16. **Obeidat S.M., Raman S**.: *An intelligent sampling method for inspecting free-form surfaces.* International Journal Advanced Manufacturing Technology 2009, 40, 1125-1136.
17. **Poniatowska M.** (2012), Deviation model based method of planning accuracy inspection of free-form surfaces using CMMs, *Measurement*, 45, 927-937.
18. **Rajamohan G., Shunmugam M. S., Samuel G. L.** (2011a), Effect of probe size and measurement strategies on assessment of freeform profile deviations using coordinate measuring machine, *Measurement*, 44, 832-841.
19. **Rajamohan G., Shunmugam M.S., Samuel G.L.** (2011b), Practical measurement strategies for verification of freeform surfaces using coordinate measuring machines, *Metrology and Measurement Systems,* XVIII, 209-222.
20. **Savio E., De Chiffre L, Schmitt R.** (2007), Metrology of freeform shaped parts, *Annals of the CIRP*, 56, 810-835.
21. **Sladek J. A.** (2016), *Coordinate Metrology: Accuracy of Systems and Measurements*. Springer, Berlin Heidelberg.
22. **Weckenmann A, Estler T., Peggs G., Mc Murtry D.** (2004), Probing Systems in Dimensional Metrology, *CIRP Ann*., 53, 657-684.

Acknowledgments: The work is supported by Polish Ministry of Science and Higher Education, and realized in Bialystok University of Technology under the project S/WM/2/2017.

DOI 10.2478/ama-2018-0041

TWO-PARAMETRIC ANALYSIS OF ANTI-PLANE SHEAR DEFORMATION OF A COATED ELASTIC HALF-SPACE

Leyla SULTANOVA*

*School of Computing and Mathematics, Keele University, Keele, Staffordshire, ST5 5BG, United Kingdom

l.sultanova@keele.ac.uk

received 31 October 2018, revised 6 December 2018, accepted 10 December 2018

Abstract: The anti-plane shear deformation problem of a half-space coated by a soft or a stiff thin layer is considered. The two-term asymptotic analysis is developed motivated by the scaling for the displacement and stress components obtained from the exact solution of a model problem for a shear harmonic load. It is shown that for a rather high contrast in stiffness of the layer and the half-space Winkler-type behaviour appears for a relatively soft coating, while for a relatively stiff one, the equations of plate shear are valid. For low contrast, an alternative approximation is suggested based on the reduced continuity conditions and the fact that the applied load may be transmitted to the interface. In case of a stiff layer, a simpler problem for a homogeneous half-space with effective boundary condition is also formulated, modelling the effect of the coating, while for a relatively soft layer a uniformly valid approximate formula is introduced.

Key words: Soft/Stiff Thin Coating, Asymptotic, Contrast, Substrate

1. INTRODUCTION

Coated structures find numerous applications in modern engineering and technology, including, in particular biological sciences and structural mechanics, see e.g. Li et al. (2014), Bose (2017) and Pawlowski (2008). The presence of a thin coating layer usually motivates an asymptotic approach relying on a small geometric parameter, see e.g. Ahmad et al. (2011), Kaplunov and Prikazchikov (2017), and Yang (2006). Often, in addition, there is a contrast in material parameters of the coating and the half-space, hence, the problem could require multiparametric analysis, similar to that presented recently by Kaplunov et al. (2016) and Kaplunov et al. (2017) for vibrations of strongly inhomogeneous structures. In case of a coated half-space, high contrast in stiffness between the layer and the substrate implies a second small material parameter, along with the two limiting cases, corresponding to a relatively soft and a relatively stiff coating. The importance of these two cases was appreciated within the framework of contact problems, see e.g. Alexandrov (2010). A two-parametric asymptotic analysis of equilibrium of a 3D half-space coated by a soft layer, allowing a variety of scenarios depending on the relation between the relative thickness and stiffness, has been carried out by Kaplunov et al. (2018).

In this paper, these results are extended to a problem of anti-plane shear deformation of a coated elastic half-space. Focusing on an anti-plane shear is of interest within linear and nonlinear solid mechanics theories, since it allows establishing a mathematically simpler analysis without loss of physical interpretation, see e.g. Horgan (1995). First, we derive the exact solution for anti-plane deformations caused by a harmonic shear load. Then, considering the relative thickness of the layer to be small, and supposing a contrast in stiffness of the layer and the half-space, we develop a two-parametric asymptotic analysis for an arbitrary shear load. While doing it, we rely on the exact solution in order to motivate the original scaling of the displacement and stresses, required for the asymptotic integration technique, see for more detail Aghalovyan (2015), Argatov and Mishuris (2016), and Goldenveizer et al. (1993). A classification following from the relation between the two asymptotic parameters is established. The results for the anti-plane displacement and stress components are obtained. In particular, we focus on the relation between the shear load and the displacement, which results in Winkler-type behaviour for a rather soft coating and involves the equations of plate shear in case of a soft layer. The derived asymptotic results are compared numerically with the exact solution for shear harmonic load.

2. STATEMENT OF THE PROBLEM

Consider an anti-plane problem of equilibrium for a homogeneous linearly elastic isotropic half-space coated by a thin isotropic layer of thickness h, subject to action of a shear force $P = P(x_1)$ at the surface of the coating ($x_3 = 0$), see Fig. 1.

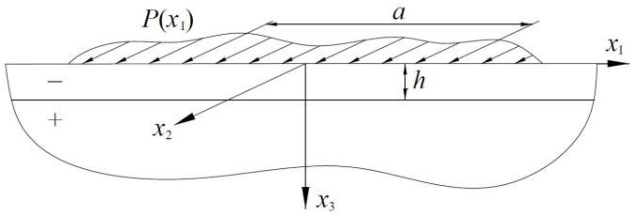

Fig. 1. Problem statement

Throughout the paper, we assume the following:

– the thickness of the layer h is small compared to a typical length scale a related to the load variation along the coordinate x_1;

– there is a contrast in stiffness of the layer and the half-space;

In view of these assumptions, we introduce a small geometrical parameter:

$$\varepsilon = \frac{h}{a} \ll 1, \tag{1}$$

and a material parameter:

$$\mu = \begin{cases} \frac{\mu^-}{\mu^+}, & \mu^- \le \mu^+ \\ \frac{\mu^+}{\mu^-}, & \mu^+ \le \mu^- \end{cases} \lesssim 1, \tag{2}$$

where: $\mu^{\pm}$ – shear moduli, with "–" and "+" denoting the layer and the half-space, respectively. The first line in (2) corresponds to the case of the soft layer, and the second line is for a relatively stiff coating. Note, that the non-nontrast case ($\mu = 1$) is also included in consideration. The parameters above may be related to each other as:

$$\mu = \varepsilon^{\alpha}, \quad \alpha \ge 0, \tag{3}$$

where for a fixed ε, α represents the level of the contrast, i.e. with an increase of α, the contrast in stiffness of the layer and the half-space becomes more pronounced.

In this paper, we concentrate on the anti-plane problem assuming, therefore, that displacements $u_1^{\pm} = u_3^{\pm} = 0$ and $u_2^{\pm}$ do not depend on x_2. Hence, defining dimensionless variables as:

$$\xi_1 = \frac{x_1}{a}, \tag{4}$$

$$\xi_3^- = \frac{x_3}{h}, \quad 0 \le x_3 \le h, \quad \xi_3^+ = \frac{x_3 - h}{a}, \quad x_3 \ge h, \tag{5}$$

the governing equations for the layer and the half-space are written as:

$$\frac{h}{a}\sigma_{12,1}^- + \sigma_{23,3}^- = 0, \quad \sigma_{12}^- = \frac{\mu^-}{a}u_{2,1}^-, \quad \sigma_{23}^- = \frac{\mu^-}{h}u_{2,3}^-, \tag{6}$$

$$\sigma_{12,1}^+ + \sigma_{23,3}^+ = 0, \quad \sigma_{12}^+ = \frac{\mu^+}{a}u_{2,1}^+, \quad \sigma_{23}^+ = \frac{\mu^+}{a}u_{2,3}^+, \tag{7}$$

where: $\sigma_{12}^{\pm}$ and $\sigma_{23}^{\pm}$ – Cauchy stresses, and comma indicates differentiation.

The boundary condition, modelling shear load at the surface of the layer, and continuity conditions at the interface take the form

$$\sigma_{23}^- = -P, \quad \xi_3^- = 0, \tag{8}$$

$$u_2^- = u_2^+, \quad \sigma_{23}^- = \sigma_{23}^+, \quad \xi_3^- = 1. \tag{9}$$

We also impose the decay condition for the displacement, i.e. $u_2^+ \to 0$ as $\xi_3^+ \to \infty$.

3. PROBLEM FOR A HARMONIC SHEAR LOAD

We begin the analysis with investigation of a model problem for a shear harmonic force

$$P = A\mu^- \sin\xi_1, \tag{10}$$

where: A – constant amplitude, see Fig. 2.

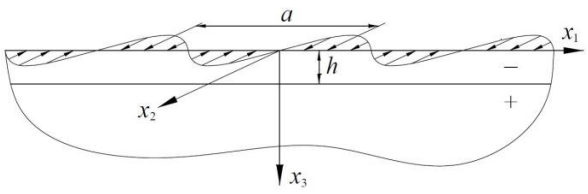

Fig. 2. Problem for a harmonic surface load

In this case, the displacemens may be sought as:

$$u_2^{\pm} = f^{\pm}(\xi_3^{\pm})\sin\xi_1. \tag{11}$$

Substituting (11) into governing equations (6) and (7), we have:

$$f^{-\prime\prime}(\xi_3^-) - \varepsilon^2 f^-(\xi_3^-) = 0, \quad f^{+\prime\prime}(\xi_3^+) - f^+(\xi_3^+) = 0. \tag{12}$$

Taking into account boundary and continuity conditions (8) and (9), respectively, the solution of (12) decaying at infinity is written as:

$$f^-(\xi_3^-) = c_1 e^{\varepsilon\xi_3^-} + c_2 e^{-\varepsilon\xi_3^-}, \quad f^+(\xi_3^+) = c_3 e^{-\xi_3^+}, \tag{13}$$

where:

$$c_i = \frac{N_i}{D}, \quad i = 1,2,3, \tag{14}$$

with:

$$N_1 = Ah(\mu^- - \mu^+), \quad N_2 = Ahe^{2\varepsilon}(\mu^- + \mu^+), \tag{15}$$

$$N_3 = 2Ahe^{\varepsilon}\mu^-, \tag{16}$$

and:

$$D = \varepsilon[\mu^-(e^{2\varepsilon} - 1) + \mu^+(e^{2\varepsilon} + 1)]. \tag{17}$$

Substituting the latter into relations (6) and (7), the stress components are found in the form:

$$\sigma_{12}^{\pm} = \frac{\mu^{\pm}}{a}f^{\pm}(\xi_3^{\pm})\cos\xi_1, \quad \sigma_{23}^+ = -\frac{\mu^+}{a}f^+(\xi_3^+)\sin\xi_1, \tag{18}$$

$$\sigma_{23}^- = \frac{\mu^-}{h}\varepsilon\left(c_1 e^{\varepsilon\xi_3^-} - c_2 e^{-\varepsilon\xi_3^-}\right)\sin\xi_1. \tag{19}$$

Then, using (1) and (2), together with (3), we deduce the leading order asymptotic behaviour of the displacement and stress components obtained above, in terms of a small parameter ε, for a relatively soft and stiff layer, see Table 1.

Tab. 1. Asymptotic behaviour of displacements and stresses

	Soft layer		Stiff layer	
	$\alpha \ge 1$	$0 \le \alpha \le 1$	$\alpha \ge 1$	$0 \le \alpha \le 1$
u_2^-	1	$\varepsilon^{\alpha-1}$	ε^{-2}	$\varepsilon^{-\alpha-1}$
σ_{12}^-	ε	ε^{α}	ε^{-1}	$\varepsilon^{-\alpha}$
σ_{23}^-	1	1	1	1
u_2^+	$\varepsilon^{\alpha-1}$	$\varepsilon^{\alpha-1}$	ε^{-2}	$\varepsilon^{-\alpha-1}$
σ_{12}^+	1	1	$\varepsilon^{\alpha-1}$	1
σ_{23}^+	1	1	$\varepsilon^{\alpha-1}$	1

Now, we study in more detail the relation between displacement u_2^- at the surface of the coating ($\xi_3^- = 0$) and prescribed load P by introducing the coefficient:

$$k = \frac{P}{u_2^-|_{\xi_3^- = 0}}. \tag{20}$$

Note, that this coefficient is constant only for the considered sinusoidal load. In general, the relation between displacement $u_2^-|_{\xi_3^- = 0}$ and load P is a function of ξ_1. In case of a shear harmonic load (10), it is given by:

$$k = \frac{A\mu^- D}{N_1 + N_2}, \tag{21}$$

following from (11), $(13)_1$ and (14). The leading order estimates of the coefficient k depending on the parameter α are presented in Table 2.

DOI 10.2478/ama-2018-0041

Tab. 2. Leading order of the coefficient k for a harmonic shear force

	k	
	Soft layer	**Stiff layer**
$\alpha > 1$	$\frac{\mu^-}{h}$	$\frac{\mu^- h}{a^2}$
$\alpha = 1$	$\frac{\mu^-\mu^+}{h\mu^+ + a\mu^-}$	$\frac{2\mu^- h}{a^2}$
$0 \le \alpha < 1$	$\frac{\mu^+}{a}$	$\frac{\mu^+}{a}$

Therefore, at $\alpha > 1$, the coefficient k does not depend on the material parameter of the half-space μ^+, meaning that the deformation of the substrate is neglected. In general, in case of a rather soft layer, it may be described as a Winkler-type behaviour, similarily to Kaplunov et al. (2018), while for a stiff layer, taking into account the term a^2, it indicates that the plate shear equation may be expected as a relation between u_2^- and P. In the range $0 \le \alpha < 1$, the relation is entirely affected by the presence of the half-space, i.e. the layer may no longer be separated, and the original problem for a coated solid should be considered. The case $\alpha = 1$ seems to be a transition point, since, for instance, for a soft layer, k depends on both the material parameters of the layer and the half-space, but, at the same time, according to assumptions (1), (2) and the relation (3), $\frac{h}{a} = \frac{\mu^-}{\mu^+} = \varepsilon$, therefore, it may also be written as $k = \frac{\mu^-}{2h}$.

4. ASYMPTOTIC ANALYSIS

In this section we develop a more general procedure for an arbitrary load acting on the surface of the layer, adopting the method of direct asymptotic integration of the equations of elasticity. Note that the scaling is motivated by the asymptotic orders in Table 1, obtained for a harmonic shear force.

4.1. Soft layer, $\alpha \ge 1$

First, we scale the displacement and stress components according to the first column of the Table 1, having for a relatively soft layer:

$$u_2^- = hu_2^{*-}, \quad \sigma_{12}^- = \mu^-\varepsilon\sigma_{12}^{*-}, \quad \sigma_{23}^- = \mu^-\sigma_{23}^{*-}, \tag{22}$$

where the quantities with the asterisk are assumed to be of the same asymptotic order. Hence, governing equations (6) become:

$$\varepsilon^2\sigma_{12,1}^{*-} + \sigma_{23,3}^{*-} = 0, \quad \sigma_{12}^{*-} = u_{2,1}^{*-}, \quad \sigma_{23}^{*-} = u_{2,3}^{*-}. \tag{23}$$

Similarly, substituting the scaling for the half-space given by:

$$u_2^+ = h\varepsilon^{\alpha-1}u_2^{*+}, \quad \sigma_{12}^+ = \mu^-\sigma_{12}^{*+}, \quad \sigma_{23}^+ = \mu^-\sigma_{23}^{*+}, \tag{24}$$

into equations (7), we get:

$$\sigma_{12,1}^{*+} + \sigma_{23,3}^{*+} = 0, \quad \sigma_{12}^{*+} = u_{2,1}^{*+}, \quad \sigma_{23}^{*+} = u_{2,3}^{*+}. \tag{25}$$

Here and below, the applied load is scaled as:

$$P = \mu^- p^*. \tag{26}$$

In what follows, boundary and continuity conditions (8) and (9), respectively, may be rewritten as:

$$\sigma_{23}^{*-} = -p^*, \quad \xi_3^- = 0, \tag{27}$$

$$u_2^{*-} = \varepsilon^{\alpha-1}u_2^{*+}, \quad \sigma_{23}^{*-} = \sigma_{23}^{*+}, \quad \xi_3^- = 1. \tag{28}$$

Next, we expand the displacements and stresses of the layer in asymptotic series:

$$\begin{pmatrix} u_2^{*-} \\ \sigma_{12}^{*-} \\ \sigma_{23}^{*-} \end{pmatrix} = \begin{pmatrix} u_2^{-(0)} \\ \sigma_{12}^{-(0)} \\ \sigma_{23}^{-(0)} \end{pmatrix} + \cdots . \tag{29}$$

Hence, at leading order we have from (23):

$$\sigma_{23,3}^{-(0)} = 0, \quad \sigma_{12}^{-(0)} = u_{2,1}^{-(0)}, \quad \sigma_{23}^{-(0)} = u_{2,3}^{-(0)}, \tag{30}$$

subject to boundary conditions at $\xi_3^- = 0$

$$\sigma_{23}^{-(0)} = -p^*. \tag{31}$$

In view of $(28)_1$, $u_2^{*-} \gg u_2^{*+}$ at $\alpha > 1$ while $u_2^{*-} \sim u_2^{*+}$ at $\alpha = 1$, therefore, the leading order continuity conditions at $\xi_3^- = 1$ become:

$$u_2^{-(0)} = 0, \quad \alpha > 1, \quad u_2^{-(0)} = u_2^{+(0)}, \quad \alpha = 1, \tag{32}$$

$$\sigma_{23}^{-(0)} = \sigma_{23}^{+(0)}. \tag{33}$$

From $(30)_1$ and satisfying (31), we obtain:

$$\sigma_{23}^{-(0)} = -p^*. \tag{34}$$

Then, using $(30)_3$ together with (32), we deduce:

$$u_2^{-(0)} = p^*(1 - \xi_3^-), \quad \alpha > 1, \tag{35}$$

$$u_2^{-(0)} = p^*(1 - \xi_3^-) + u_2^{+(0)}\big|_{\xi_3^- = 1}, \quad \alpha = 1. \tag{36}$$

Therefore, as it was discussed above, at $\xi_3^- = 0$, the relation between displacement and applied load at $\alpha > 1$ is not affected by the presence of the substrate, which may be described as Winkler-type behaviour, while for $\alpha = 1$ the reaction of the half-space is involved. The same happens for shear stress $\sigma_{12}^{-(0)}$, for which we have from $(30)_2$, (35) and (36):

$$\sigma_{12}^{-(0)} = \frac{\partial p^*}{\partial \xi_1}(1 - \xi_3^-), \quad \alpha > 1, \tag{37}$$

$$\sigma_{12}^{-(0)} = \frac{\partial p^*}{\partial \xi_1}(1 - \xi_3^-) + \frac{\partial u_2^{+(0)}}{\partial \xi_1}\Big|_{\xi_3^- = 1}, \quad \alpha = 1. \tag{38}$$

4.2. Soft layer, $0 \le \alpha < 1$

Scaling for the layer now takes the form:

$$u_2^- = h\varepsilon^{\alpha-1}u_2^{*-}, \quad \sigma_{12}^- = \mu^-\varepsilon^\alpha\sigma_{12}^{*-}, \quad \sigma_{23}^- = \mu^-\sigma_{23}^{*-}, \tag{39}$$

leading to:

$$\varepsilon^{\alpha+1}\sigma_{12,1}^{*-} + \sigma_{23,3}^{*-} = 0, \tag{40}$$

$$\sigma_{12}^{*-} = u_{2,1}^{*-}, \quad \varepsilon^{1-\alpha}\sigma_{23}^{*-} = u_{2,3}^{*-}. \tag{41}$$

Scaling and equations for the half-space are taken as (24) and (25), respectively, with boundary condition (27), whereas the continuity conditions become:

$$u_2^{*-} = u_2^{*+}, \quad \sigma_{23}^{*-} = \sigma_{23}^{*+}, \quad \xi_3^- = 1. \tag{42}$$

At leading order, the equations for the layer are:

$$\sigma_{23,3}^{-(0)} = 0, \quad \sigma_{12}^{-(0)} = u_{2,1}^{-(0)}, \quad u_{2,3}^{-(0)} = 0, \tag{43}$$

subject to boundary condition (31) and the following continuity conditions:

$$u_2^{-(0)} = u_2^{+(0)}, \quad \sigma_{23}^{-(0)} = \sigma_{23}^{+(0)}, \quad \xi_3^- = 1. \tag{44}$$

As above, quantity $\sigma_{23}^{-(0)}$ is expressed as (34). Then, $(43)_3$ and $(44)_1$ imply:

$$u_2^{-(0)} = u_2^{+(0)}\big|_{\xi_3^-=1}. \tag{45}$$

Finally, $(43)_2$ yields:

$$\sigma_{12}^{-(0)} = \frac{\partial u_2^{+(0)}}{\partial \xi_1}\Big|_{\xi_3^-=1}. \tag{46}$$

Hence, shear displacement and stress depend only on the deformation of the substrate.

4.3. Stiff layer, $\alpha \geq 1$

For a stiff layer, we scale the displacements and stresses according to the third column in Table 1:

$$u_2^- = h\varepsilon^{-2}u_2^{*-}, \quad \sigma_{12}^- = \mu^-\varepsilon^{-1}\sigma_{12}^{*-}, \quad \sigma_{23}^- = \mu^-\sigma_{23}^{*-}, \tag{47}$$

which implies:

$$\sigma_{12,1}^{*-} + \sigma_{23,3}^{*-} = 0, \quad \sigma_{12}^{*-} = u_{2,1}^{*-}, \quad \varepsilon^2\sigma_{23}^{*-} = u_{2,3}^{*-}. \tag{48}$$

Scaling for the half-space is taken as:

$$u_2^+ = h\varepsilon^{-2}u_2^{*+}, \tag{49}$$

$$\sigma_{12}^+ = \mu^-\varepsilon^{\alpha-1}\sigma_{12}^{*+}, \quad \sigma_{23}^+ = \mu^-\varepsilon^{\alpha-1}\sigma_{23}^{*+}, \tag{50}$$

which, substituted into (7), gives (25). Boundary condition, again, is expressed as (27), whereas the continuity conditions are:

$$u_2^{*-} = u_2^{*+}, \quad \sigma_{23}^{*-} = \varepsilon^{\alpha-1}\sigma_{23}^{*+}, \quad \xi_3^- = 1. \tag{51}$$

At leading order for the layer we have:

$$\sigma_{12,1}^{-(0)} + \sigma_{23,3}^{-(0)} = 0, \quad \sigma_{12}^{-(0)} = u_{2,1}^{-(0)}, \quad u_{2,3}^{-(0)} = 0, \tag{52}$$

with boundary condition (31). Taking into account $(51)_2$, i.e. $\sigma_{23}^{*-} \gg \sigma_{23}^{*+}$ at $\alpha > 1$, and $\sigma_{23}^{*-} \sim \sigma_{23}^{*+}$ at $\alpha = 1$, the continuity conditions at $\xi_3^- = 1$ are:

$$u_2^{-(0)} = u_2^{+(0)}, \tag{53}$$

$$\sigma_{23}^{-(0)} = 0, \quad \alpha > 1, \quad \sigma_{23}^{-(0)} = \sigma_{23}^{+(0)}, \quad \alpha = 1. \tag{54}$$

From $(52)_3$ we have:

$$u_2^{-(0)} = V, \tag{55}$$

where: $V = V(\xi_1)$, i.e. displacement $u_2^{-(0)}$ is constant across the thickness of the layer, giving the function V, which may be denoted as a shear of the coating. Next, we deduce from $(52)_2$:

$$\sigma_{12}^{-(0)} = \frac{\partial V}{\partial \xi_1}. \tag{56}$$

Using $(52)_1$ and satisfying boundary condition (31), we obtain:

$$\sigma_{23}^{-(0)} = -\frac{\partial^2 V}{\partial \xi_1^2}\xi_3^- - p^*. \tag{57}$$

Finally, from continuity conditions (54), we have:

$$\frac{\partial^2 V}{\partial \xi_1^2} = -p^*, \quad \alpha > 1, \tag{58}$$

$$\frac{\partial^2 V}{\partial \xi_1^2} = -p^* - \sigma_{23}^{+(0)}\big|_{\xi_3^-=1}, \quad \alpha = 1, \tag{59}$$

which are in fact the equations of plate shear, with the substrate reaction equal to 0 at $\alpha > 1$.

4.4. Stiff layer, $0 \leq \alpha < 1$

In this case, the scaling for the layer is given by:

$$u_2^- = h\varepsilon^{-\alpha-1}u_2^{*-}, \quad \sigma_{12}^- = \mu^-\varepsilon^{-\alpha}\sigma_{12}^{*-}, \quad \sigma_{23}^- = \mu^-\sigma_{23}^{*-}, \tag{60}$$

with the governing equations:

$$\varepsilon^{1-\alpha}\sigma_{12,1}^{*-} + \sigma_{23,3}^{*-} = 0, \tag{61}$$

$$\sigma_{12}^{*-} = u_{2,1}^{*-}, \quad \varepsilon^{\alpha+1}\sigma_{23}^{*-} = u_{2,3}^{*-}. \tag{62}$$

Scaling for the half-space is:

$$u_2^+ = h\varepsilon^{-\alpha-1}u_2^{*+}, \quad \sigma_{12}^+ = \mu^-\sigma_{12}^{*+}, \quad \sigma_{23}^+ = \mu^-\sigma_{23}^{*+}, \tag{63}$$

with equations (25). Boundary and continuity conditions are taken as (27) and (42).

The leading order equations and results are the same as in Subsection 4.2.

5. NUMERICAL COMPARISON OF THE ASYMPTOTIC RESULTS WITH THE EXACT SOLUTION

In this section the derived asymptotic results are tested by comparison with the exact solution of a problem for harmonic load (10) applied at the surface of the layer $x_3 = 0$. In doing so, we study the coefficient k introduced in (20).

For the exact solution, coefficient k follows from (21).

For the asymptotic results, in case of a soft layer, we use relations (35) and (36) for $\alpha > 1$ and $\alpha = 1$, respectively, and (45) for $0 \leq \alpha < 1$. Shear stress $\sigma_{23}^{-(0)}$ is uniform across the thickness of the layer, see (34), and may be transmitted to the interface, therefore, the value of the interfacial displacement $u_2^{+(0)}\big|_{\xi_3^-=1}$, due to continuity conditions (33) and $(42)_2$, may be found from a simpler problem for a homogeneous half-space with $\sigma_{23}^+ = -P$. Its solution for harmonic load (10) is presented as Case 1 in Appendix.

In order to derive k for a hard layer, we solve plate shear equation (58) for $\alpha > 1$ and (59) for $\alpha = 1$. For the latter case, taking into account continuity condition (53), the deflection of the layer, see (55), may be again derived from a problem for a half-space with $\sigma_{23}^+ = -P - \frac{\mu^+}{a}\frac{\partial^2 u_2^+}{\partial \xi_1^2}\Big|_{\xi_3^+=0}$ (Case 2 in Appendix for harmonic load). The case $0 \leq \alpha < 1$ is identical to one for a soft layer.

As a result, asymptotic formulae for the coefficient k coincide with leading order exact solution presented in Table 2.

As an illustration, we plot the dimensionless coefficient

$$k_* = \frac{h}{\mu^-}k, \tag{64}$$

in Fig. 3 and 4 for a soft and a stiff layer, respectively, with

DOI 10.2478/ama-2018-0041

$\alpha = \log_\varepsilon \mu$, Poisson's ratios $\nu^- = 0.25$ and $\nu^+ = 0.3$, and $\varepsilon = 0.1$. Here, blue solid lines correspond to the exact solution, dashed and dot-dashed lines display the asymptotic approximations at $\alpha > 1$ (formula (35) in case of a soft coating and (58) for a stiff one) and $0 \le \alpha < 1$ (formula (45) valid for both soft and stiff layers), respectively, which have limited ranges of applicability. For a soft coating, case $\alpha = 1$ gives two-term approximation (36), which appears to be uniformly valid over the whole range of parameter α, and the associated curve, denoted by red dots in Fig. 3, is very close to the exact solution. As for a stiff layer, approximation at $\alpha = 1$, represented by formula (59), is a limiting case, displayed by the blue dot in Fig. 4, being valid only for this particular value of α, therefore there is no uniformly valid approximation. We can, however, match the derived approximations through

$$\tilde{k}_* = k_*^0 e^{-\frac{\alpha}{b}} + k_*^\infty \left(1 - e^{-\frac{\alpha}{b}}\right), \tag{65}$$

where: k_*^0 and k_*^∞ – dimensionless coefficients for approximations at $\alpha = 0$ and $\alpha > 1$, respectively, and b can be found using the value of k_* at $\alpha = 1$. For harmonic load (10), $b \approx 0.455$, and the related curve is plotted with red dots in Fig. 4.

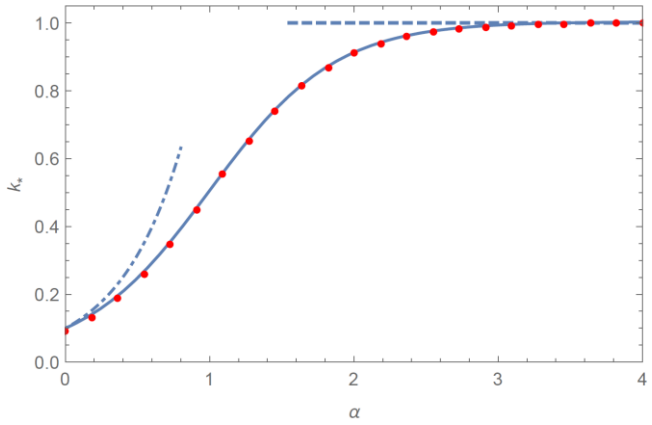

Fig. 3. Asymptotic and exact solution for harmonic load for a soft coating

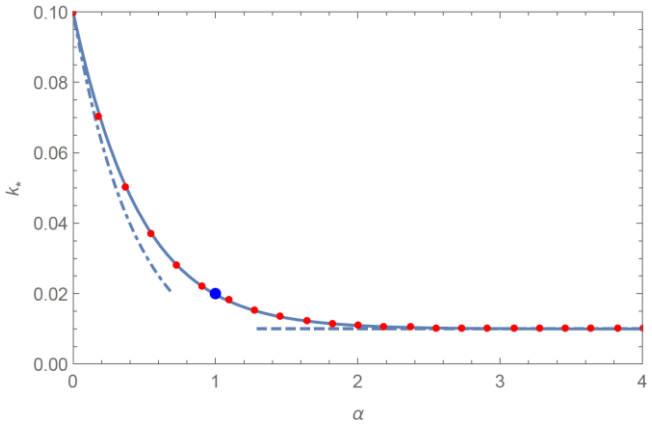

Fig. 4. Asymptotic and exact solution for harmonic load for a stiff coating

6. CONCLUDING REMARKS

A full two-parametric asymptotic analysis (in ε and μ) of the anti-plane shear deformation problem of a coated half-space is developed. It is demonstrated that in case of a relatively soft layer for a rather high contrast ($\alpha > 1$), the deformation of the substrate can be neglected, which leads to Winkler-type behaviour. In a similar situation for a relatively stiff coating ($\alpha \ge 1$), we arrive at equations of plate shear. At the same time, in the intermediate range of contrast in stiffness considered in Sections 4.2 and 4.4, the layer deformation is strongly affected by the presence of the substrate. In this case, shear deformation may be found from a simpler problem for a half-space. The latter, together with a Winkler-type behaviour term, result in two-term asymptotic formula (36) uniformly valid over the whole range of material parameter for a relatively soft layer. For a stiff coating, when the geometrical and material parameters are of the same order ($\alpha = 1$), it is also possible to reduce the original problem for a coated solid to a problem for a homogeneous half-space with effective boundary conditions at the surface.

The obtained solution is also of importance for problems of delamination between the thin coating and the substrate, especially in tribological context, see e.g. Goryacheva and Torskaya (2010), Holmberg et al. (2009) and Jiang et al. (2010).

In addition, we mention related problems for the imperfect transmission conditions, see Mishuris (2003, 2004) and Mishuris and Öchsner (2005). Note that such asymptotically evaluated simplified conditions can be verified numerically with FEM analysis, see e.g. Mishuris et al. (2005), Mishuris and Öchsner (2007). This is of crucial importance as accurate mathematical proof may not always be available. On the other hand, such conditions fail near singular points (crack tip, edges), but still may be valuable for physical applications in fracture mechanics, see Mishuris (1999, 2001).

We also note related problems on homogenization of high-contrast periodic structures, see e.g. Cherdantsev and Cherednichenko (2012), Figotin and Kuchment (1998), Kaplunov and Nobili (2017), and Smyshlyaev (2009).

APPENDIX

Consider a homogeneous elastic half-space ($\xi_3^+ \ge 0$) subject to the boundary conditions presented in Table 3.

Tab. 3. Summary for a homogeneous half-space with various cases of boundary conditions

	Case 1	Case 2
Boundary conditions		
σ_{23}^+	$-A\mu^- \sin\xi_1$	$-A\mu^- \sin\xi_1 - \dfrac{\mu^+}{a}\dfrac{\partial^2 u_2^+}{\partial \xi_1^2}\Big\vert_{\xi_3^+=0}$
Coefficient in (13)		
c_3	$\dfrac{Aa\mu^-}{\mu^+}$	$\dfrac{Aa\mu^-}{2\mu^+}$
Displacements and stresses at the surface		
u_2^+	$\dfrac{Aa\mu^- \sin\xi_1}{\mu^+}$	$\dfrac{Aa\mu^- \sin\xi_1}{2\mu^+}$
σ_{12}^+	$A\mu^- \cos\xi_1$	$\dfrac{A\mu^- \cos\xi_1}{2}$
σ_{23}^+	$-A\mu^- \sin\xi_1$	$-\dfrac{A\mu^- \sin\xi_1}{2}$

The equations of the formulated problem and the solution are given by (7) and (11) with functions $(13)_2$, where the values of the coefficient c_3, corresponding to the related case of the applied boundary conditions, are also presented in Table 3, together with the displacement and stress components at the surface $\xi_3^+ = 0$.

REFERENCES

1. **Aghalovyan L.** (2015), *Asymptotic theory of anisotropic plates and shells*, Singapore: World Scientific.
2. **Ahmad M., Nolde E., Pichugin, A.V.** (2011), Explicit asymptotic modelling of transient Love waves propagated along a thin coating, *Zeitschrift für angewandte Mathematik und Physik*, 62(1), 173-181.
3. **Alexandrov V.M.** (2010), Contact problems on soft and rigid coatings of an elastic half-plane, *Mechanics of Solids*, 45(1), 34-40.
4. **Argatov I., Mishuris G.** (2016), *Contact mechanics of articular cartilage layers*, Springer.
5. **Bose S.** (2017), *High temperature coatings*, Butterworth-Heinemann.
6. **Cherdantsev M., Cherednichenko K.D.** (2012), Two-scale Γ-convergence of integral functionals and its application to homogenisation of nonlinear high-contrast periodic composites, *Archive for Rational Mechanics and Analysis*, 2014(2), 445-478.
7. **Figotin A., Kuchment P.** (1998), Spectral properties of classical waves in high-contrast periodic media, SIAM Journal on Applied Mathematics, 58(2), 683-702.
8. **Goldenveizer A.L., Kaplunov J.D., Nolde E.V.** (1993), On Timoshenko-Reissner type theories of plates and shells, *International Journal of Solids and Structures*, 30(5), 675-694.
9. **Goryacheva I.G., Torskaya E.V.** (2010), Modeling of fatigue wear of a two-layered elastic half-space in contact with periodic system of indenters, *Wear*, 268(11-12), 1417-1422.
10. **Holmberg K., Ronkainen H., Laukkanen A., Wallin K., Hogmark S., Jacobson S., Wiklund U., Souza R.M., Ståhle P.** (2009). Residual stresses in TiN, DLC and MoS2 coated surfaces with regard to their tribological fracture behaviour. *Wear*, 267(12), 2142-2156.
11. **Horgan C.O.** (1995), Anti-plane shear deformations in linear and nonlinear solid mechanics, *SIAM review*, 37(1), 53-81.
12. **Jiang H., Browning R., Whitcomb J.D., Ito M., Shimouse M., Chang T.A., Sue H.J.** (2010). Mechanical modeling of scratch behavior of polymeric coatings on hard and soft substrates, *Tribology letters*, 37(2), 159-167.
13. **Kaplunov J., Nobili A.** (2017), Multi-parametric analysis of strongly inhomogeneous periodic waveguideswith internal cutoff frequencies, *Mathematical Methods in the Applied Sciences*, 40(9), 3381-3392.
14. **Kaplunov J., Prikazchikov D., Sergushova O.** (2016), Multi-parametric analysis of the lowest natural frequencies of strongly inhomogeneous elastic rods, *Journal of Sound and Vibration,* 366, 264-276.
15. **Kaplunov J., Prikazchikov D., Sultanova L.** (2018), Justification and refinement of Winkler-Fuss hypothesis, *Zeitschrift für Angewandte Mathematik und Physik,* 69(3), 80.
16. **Kaplunov J., Prikazchikov D.A.** (2017), Asymptotic theory for Rayleigh and Rayleigh-type waves, *Advances in Applied Mechanics*, 50, 1-106, Elsevier.
17. **Kaplunov J., Prikazchikov D.A., Prikazchikova, L.A.** (2017), Dispersion of elastic waves in a strongly inhomogeneous three-layered plate, *International Journal of Solids and Structures*, 113, 169-179.
18. **Li M., Liu Q., Jia Z., Xu X., Cheng Y., Zheng Y., Xi T., Wei S.** (2014), Graphene oxide/hydroxyapatite composite coatings fabricated by electrophoretic nanotechnology for biological applications, *Carbon*, 67, 185-197.
19. **Mishuris G.** (2001), Interface crack and nonideal interface concept (Mode III), *International Journal of Fracture*, 107(3), 279–296.
20. **Mishuris G.** (2003), Mode III interface crack lying at thin nonhomogeneous anisotropic interface. Asymptotics near the crack tip, *IUTAM Symposium on Asymptotics, Singularities and Homogenisation in Problems of Mechanics*, 251-260.
21. **Mishuris G.** (2004), Imperfect transmission conditions for a thin weakly compressible interface. 2D problems, *Archives of Mechanics*, 56(2), 103-115.
22. **Mishuris G. and Öchsner A.** (2005), Transmission conditions for a soft elasto-plastic interphase between two elastic materials. Plane strain state, *Archives of Mechanics*, 57(2-3), 157-169.
23. **Mishuris G. and Öchsner A.** (2007), 2D modelling of a thin elasto-plastic interphase between two different materials: plane strain case, *Composite Structures*, 80(3), 361-372.
24. **Mishuris G., Öchsner A. and Kuhn G.** (2005), FEM-Analysis of nonclassical transmission conditions between elastic structures part 1: soft imperfect interface, *CMC-TECH SCIENCE PRESS*, 2(4), 227.
25. **Mishuris G.S.** (1999), Stress singularity at a crack tip for various intermediate zones in bimaterial structures (Mode III), *International Journal of Solids and Structures*, 36(7), 999-1015.
26. **Pawlowski L.** (2008), *The science and engineering of thermal spray coatings*, John Wiley & Sons.
27. **Prikazchikova L., Ece Aydın Y., Erbaş B., Kaplunov J.** (2018), Asymptotic analysis of an anti-plane dynamic problem for a three-layered strongly inhomogeneous laminate, *Mathematics and Mechanics of Solids*, 1081286518790804.
28. **Smyshlyaev V.P.** (2009), Propagation and localization of elastic waves in highly anisotropic periodic composites via two-scale homogenization, *Mechanics of Materials*, 41(4), 434-447.
29. **Yang F.** (2006), Asymptotic solution to axisymmetric indentation of a compressible elastic thin film, *Thin Solid Films*, 515(4), 2274-2283.

Acknowledgement: The study was supported by ACORN Scholarship from Keele University. Fruitful discussions with J. Kaplunov and D. A. Prikazchikov and valuable suggestions of the referees are gratefully acknowledged. The author was also supported during her visit to Russia by grant 14.Z50.31.0036 awarded to R.E. Alexeev from Nizhny Novgorod Technical University by the Department of Education and Science of the Russian Federation.

DOI 10.2478/ama-2018-0042

A NEW FUEL-INJECTION MECHATRONIC CONTROL METHOD FOR DIRECT-INJECTION INTERNAL COMBUSTION ENGINES

Józef TUTAJ[*], Bogdan FIJAŁKOWSKI[**]

[*]Institute for Automotive Vehicles and Combustion Engines, Department of Mechanical Engineering, Cracow University of Technology, Al. Jana Pawła II 37, 31-864 Kraków, Poland
[**]Institute of Technology, State Higher Vocational School in Nova Sandec, ul. Staszica 1, 33-300 Nowy Sącz, Poland

pmtutaj@cyf-kr.edu.pl, pmfijalk@cyf-kr.edu.pl

received 6 June 2017, revised 7 December 2018, accepted 11 December 2018

Abstract: In this paper, a novel fuel-injection mechatronic control method and system for direct injection (DI) internal combustion engines (ICE) is proposed. This method and system is based on the energy saving in a capacitance using DC-DC converter, giving a very fast ON state of the fuel injectors' electro-magnetic fluidical valves without an application of the initial load current. A fuel-injection controller for the DI ICEs that provides a very short rising time of an electromagnet-winding current in an initial ON state of the fuel-injector's electromagnetic fluidical valves, which improves a fuel-injection controller reliability and simplify its construction, is presented. Due to a number of advantages of afore -mentioned fuel-injection mechatronic control method and system, it may be utilised for the DI ICEs with fuel injectors dedicated to all types of liquid and/or gas fuels, for example, gasoline, diesel-oil, alkohol, LPG and NPG.

Key words: Direct Injection, Internal Combustion Engine, Fuel Injection, Injection Control System

1. INTRODUCTION

Currently on automotive market, more and more automotive vehicles use internal combustion engines (ICE) with a spark-ignition and direct-fuel injection. The idea for directly injection consists in forming the mixture directly in a combustion chamber. To achieve this, the electromagnetic fuel injector (EFI) is placed in the combustion chamber and by an intake fluidical valve is flow only an air.

A special injection mechano-hydraulical (M-H) pump generates the fuel injection at high pressure (5 to 12 MPa). The task of the fuel injector is dosing and spraying of a fuel into the smallest particles to provide an adequate mixing of the fuel and air in a specific area of the combustion chamber. After activation of an electromagnet of the EFI by an appropriate current pulse, the fuel is injected into the combustion chamber due to the pressure difference inside and outside fuel injector.

The idea of direct injection (DI) of a gasoline is quite old (Bosch 2014, Zhao 2016), but mass production took place only since 1995 with the introduction of ICEs with the gasoline direct injection (GDI) by Mitsubishi.

Electronically controlled fuel injection is currently used more widely, both in ICEs with the spark ignition with different markings of the supply system (GDI, FSI, IDE, HPI, JTS, etc.), as well as – Diesel ICEs (HDI, JTD, CDI, DCI, TDI etc.).

EFIs for ICEs with the direct fuel injection need to convey the current pulse with the proper value of the instantaneous power to the winding of the fuel injection electromagnet in the initial phase of fuel injection's opening, due to the operation to be performed by moving the needle fuel injector with a specific mass in a relatively short ON state (Achleitner et al., 2007; Husted et al., 2014).

The purpose of this article is to present a new method of control and powering of the injector of the direct injection system, which uses the energy stored in the additional capacitor to fast force the winding current, and does not need to be taken into account when controlling the so-called "initial load phase" time (Fig. 2).

The paper presents the results of electric current measurements of the injector during experimental tests.

1.1. A fuel injecttion mechatronic control for direct-injection internal combustion engines

In conventional fuel-injection mechatronic control, the microcontroller generates the control voltage for the solenoid coil of the EFI equals 60 - 90 V that is necessary to activate the EFIs of ICEs with the direct fuel injection. The internal structure of the EFI is shown in Fig. 1.

The control voltage is so high so as to minimize a response time of the EFI's mechatronic-control signal and get a short time of the fuel injection, which should be less than time of the fuel injection for ICEs with the fuel injection into the intake manifold (Fig. 2).

1.2. An initial load phase

The winding of the fuel-injector's electromagnet is powered by a pulse-width-modulated (PWM) voltage of value equals 12 – 14 V, in order to stabilize the current value of about 1 A.

An initial load phase prepares the gasoline fuel injector fuel to open in a short time, through the initial activation of the fuel

injector (approx. 1.5 ms before the beginning of opening of the EFI) to generate the initial value of the EFI's electromagnet-winding current.

The EFI's solenoid coil consists of an electrical circuit RL, and therefore a presence of the inductance L (several mH) in depending on the type of the EFI and its resistance R (0.5-2 Ω) causes that at the EFI's solenoid-coil supply voltage of a constant value, the current rises from zero to a steady-state value limited by the resistance R of the EFI's solenoid coil.

The initial load phase allows bringing faster floating of the EFI's needle during opening of the electromagnetic fluidical valve by the primary saving of an electrical energy in the inductance.

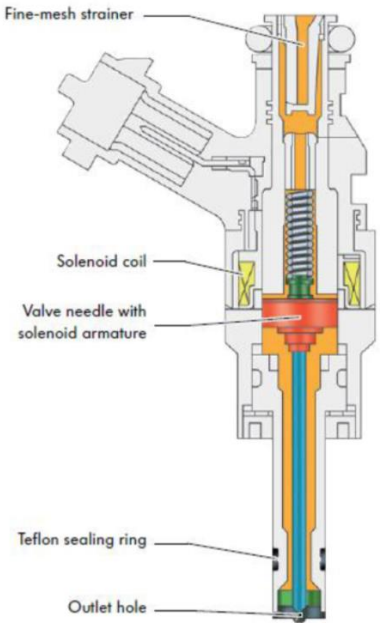

Fig. 1. Electromagnetic fuel injector (Bosch, 2014).

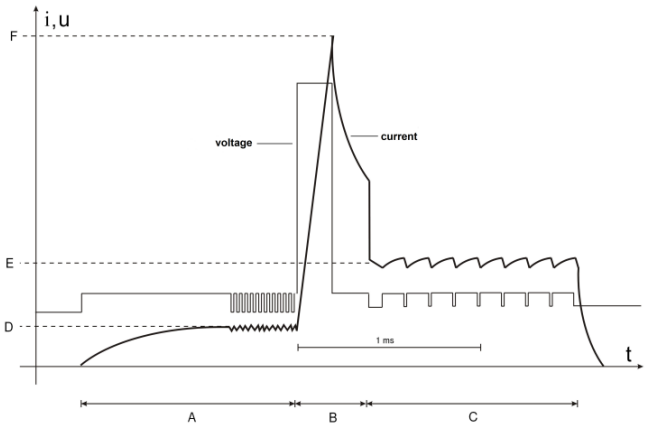

Fig. 2. Waveforms of the fuel-injector's current and voltage: A - initial load phase: B - excitation phase; C - hold-up phase; D - initial load current; F - excitation current; E - hold-up current

1.3. An excitation phase

An excitation phase is for causing a rapid increase of the EFI's needle by temporarily increasing the current flowing through the fuel-injector's solenoid coil. The EFI's electromagnet winding is supplied on a following ways: by means of an electrical valve (electronic switch) that for a short time commutate the voltage of about 80-90 V, which increases the winding's current to an instantaneous value of about 11-12 A. Afterwards, the EFI's solenoid coil is switched to the voltage of 12-14 V, and causes a decrease in the forcing current impulse. It should be noted that the relatively high current flows only for a very short time of about 0.5 ms without any causing any thermal overload of the electromagnet's winding.

The high instantaneous value of the power-pulse control will cause decreasing of the opening time of the EFI. The width of the voltage pulse (the voltage wave-form of the EFI's electromagnet solenoid coil supply in Fig. 1) must be controlled with high accuracy, because even a small change in the duration of the voltage strongly influences the instantaneous value of the electro-magnet-winding current.

1.4. A holding-up phase

Holding-up phase allows you to continue a power supply (opening of the EFI), limiting the saved electrical energy needed to held the EFI's needle in the open position by a few milliseconds, depending on the required fuel dose. The EFI's solenoid coil is supplied as follows: with the PWM controlled voltage of about 12-14 V; and the current of about 2.5-3 A. The duration of the holding phase (1-5 ms) determines the size of the dose of fuel injected into the combustion chamber of the ICE. Loss of current pulse closes the EFI.

The above-described method for controlling fuel injectors for DI ICEs by many car manufacturers has significant drawbacks. The use of an initial-load-phase's current pulse (the prediction pulse opening the fuel injector) causes as well an additional fuel-injector's thermal load – an additional heating of the windings of the electromagnet coil during the initial-load phase of the EFI's opening, as troublesome fuel-dose control. Because the synchronization pulses control of fuel injectors should take into account the additional lead time of the initial-load phase and convert a position angle of the crankshaft), for the EFI's opening at a predetermined angular position of the crankshaft of the ICE.

A second shortcoming of this control method is a disadvantageous shape of the current pulse in the electromagnet winding of the fuel-injector during an excitation phase (Fig. 2).

The shape of the current pulse in the excitation-phase control like a 'peak' that results in generation of harmonics with higher frequencies and increasing of larger eddy-current losses in a magnetic circuit of the EFI. The exact stabilization of the excitation-phase duration due to the fact that in the case of un-controlled extension of this impulse may be destroyed the EFI (the electromagnet-winding current - resulting from the higher supply voltage of 80-90 V and lower impedance could be achieved in the long run value of tens of amperes).

2. A NEW METHOD AND FUEL MECHATRONIC CONTROL SYSTEM FOR DIRECT-INJECTION INTERNAL COMBUSTION ENGINES

In Fig. 3 is shown a fuel-injection mechatronic control system for DI ICEs that is based on an electrical energy accumulation in a capacitor and fast transfer of the power to the EFI's electromagnet solenoid coil.

DOI 10.2478/ama-2018-0042

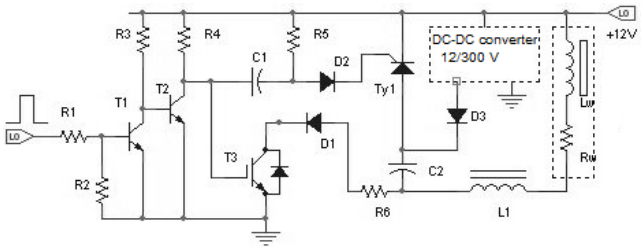

Fig. 3. Schematic diagram of the fuel-injector controller for DI ICEs

The capacitor C2 collects electricity using the diode D3 is charged from the output voltage 12/300 V of the DC-DC converter. With the emergence of the input control pulse is actuated at once the thyristor Ty1 and isolated-gate bipolar transistor (IGBT) T3. The energy stored in the capacitor C2 is in a very short period of time transferred to the additional inductance L1 and the fuel-injector's electromagnet winding. After discharging the capacitor C2, a function to maintain the current of the EFI's electromagnet through the IGBT T3 by means of the two-terminal circuit consisting of the high-voltage pulse diode D1 (400 V, 5 A), and additional resistor R6. A value of the resistor R6 determines a value of the holding current (Fig. 3). Since the energy stored in the capacitor C2 depends only on the output voltage of the DC-DC converter and its capacitance, and therefore the value of this energy can be easily stabilized and the EFI is protected from damage even in the case of a wrong control pulse appearance (e.g. due to interference). After an exchange of energy between the capacitor C2 and the EFI's electromagnet winding Rw, Lw during the holding-up phase, the commutation system consisting of components: L1, R6, D1, T3, holds up the current in the EFI's electromagnet winding. Very fast exchange of energy between the capacitor C2 and the additional inductance L1 and EFI's electromagnet winding Lw, Rw lasts approximately 0.3 ms (instead of approx. 0.5 ms in a conventional fuel-injection control system). It means that there is no need for an initial-load-phase pulse of the EFI, which simplifies the control and reduces heat losses in the EFI's electromagnet winding (no initial-load-phase current of approx. 1 (A) during approximately 1.5 (ms). An additional advantage (in addition to faster opening of the EFI) is preferable to form of a forcing pulse shape, which reduces the losses in the magnetic circuit of the EFI. The schematic diagram of the 12V / 250-300V DC-DC converter is shown in Fig. 4.

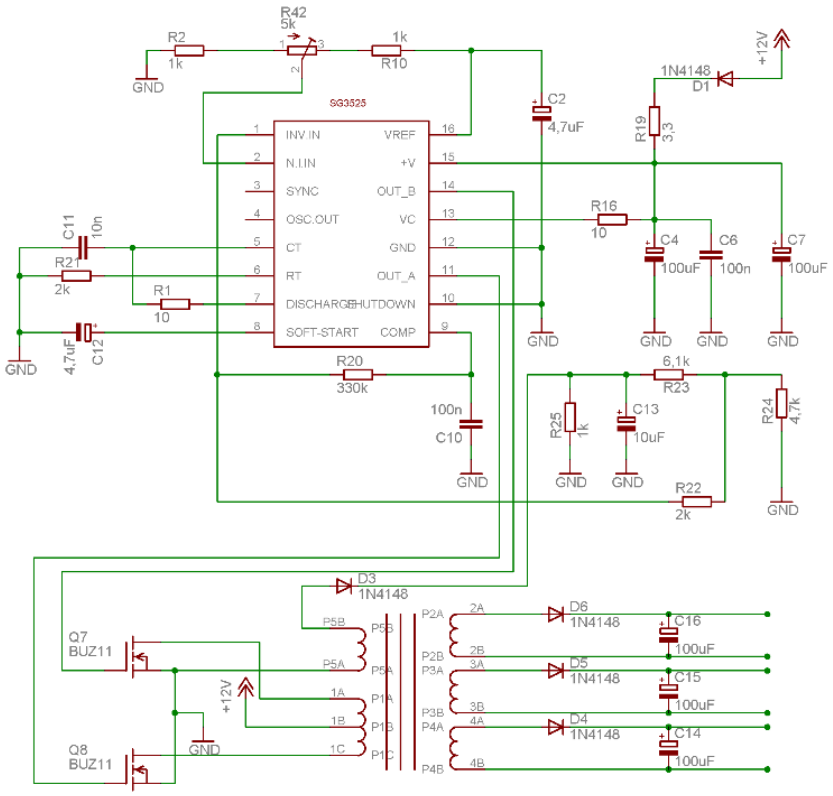

Fig. 4. Circuit diagram of the 12V / 250-300V DC-DC converter

An auxiliary voltage of 250 - 300 V is generated by the DC-DC converter with a feedback loop to stabilize the output voltage using the application specified integrated circuit (ASIC) type SG3525.

2.1. Mathematical model of the pressure dynamics

In this paper, we exercise a mathematical model describing the pressure dynamics in the common rail (CR) rail that is projected and experimentally validated in di Gaeta et al. (2009, 2011, 2012). This mathematical model depicts the electrical dynamics of the EFI (fluidical valve), ignoring the effects owing to the movement of its plunger (i.e. inductance variations and back-electromotive force), and the actuation circuit utilized to drive the EFI fluidical valve) as well. According with this alternative the pressure, say p(t) bar, in the CR depends on the mechano-hydraulical (M-H) pump rotational speed and EFI current i(A), and

it can be de-composed into two components, namely the mean pressure term, say pa(t), and the residual pressure, p(t), relating the ripple around the mean value. The CR dynamical system is then given by:

$$\frac{di}{dt} = \frac{R}{L} i + \frac{V_b}{L}\left(\frac{a\delta(t)+b}{100}\right), \quad (1a)$$

$$p_a(t) = c(N)i + d(N), \quad (1b)$$

$$p(t) = p_a(t) + \eta(t), \quad (1c)$$

where: δ (%) is the duty cycle expressed in percentage terms of the PWM signal used to actuate the EFI hydraulical valve, a and b are parameters of the EFI actuation circuit, L (H) and R (Ω) are the EFI (hydraulical valve) inductance and the electric resistance of solenoid coil, respectively, whereas V_b (V) is the chemo-electrical (CH-E) storage battery voltage supplying the power circuit and N (rpm) is the rotational speed of the M-H pump that is equal to N + Nc/2 with Nc being the ICE rotational speed.

The terms c(N) and d(N) in (1) depend on the M-H pump rotational speed N and have to be experimentally identified. According to the approach in di Gaeta et al. (2009), we mathematically model them as third-order polynomials of the form:

$$c(N) = \sum_{k=0}^{3} c_k \left(\frac{N}{10^3}\right)^k, d(N = \sum_{k=0}^{3} d_k \left(\frac{N}{10^3}\right)^k. \quad (2)$$

2.2. GDI injector's mathematical model

Since for the design of basic automotive control loops, namely air-to-fuel ratio (AFR) control, the control variable to be designed is the mass of fuel to be injected, a relation between this control variable and the time of injection is essential for the integration of the CR in the entire ICE control system (Gupta et al., 2011; Jiangjian et al., 2007; Tang et al., 2009; Yan and Wang, 2011).

In this paper, we advise and validate by means of experimental data a simple but effective static mathematical model for the injected mass that obtains the following mathematical structure:

$$m_{inj} = T_{inj}\, r_1 \sqrt{\Delta P} + (q_1 \Delta P + q_0), \quad (3)$$

where: m_{inj} (mg) is the actual injected fuel mass, r_1, q_0 and q_1 are the mathematical model parameters to be tuned via experiments while ΔP (bar) is the pressure difference between the upstream EFI (rail pressure) and the downstream EFI (ambient pressure during tests).

Once the mathematical model of the injected fuel mass (Eq. 3) is available, the inverse relation describing the injection calibrated time as a function of a desired fuel mass is:

$$T_{inj} = \frac{m_d - q_1 \Delta P - q_0}{r_1 \sqrt{\Delta P}}, \quad (4)$$

where: m_d (mg) is the demanded fuel mass to be sprayed into ICE cylinder at the injection pressure ΔP determined by the AFR control duty (Corno et al., 2008; Gaeta et al., 2012).

3. THE MEASUREMENT WAVEFORMS OF THE FUEL-INJECTOR'S CURRENT PULSES

In Fig. 5 are shown waveforms of the current pulses for DI ICEs of fuel for two cases of the fuel-dose control.

In waveforms can be observed a very short forcing-current-pulse rise time to peak value of approx. 11 A, without the use initial-load phase and the ability to obtain short time of opening of the EFI.

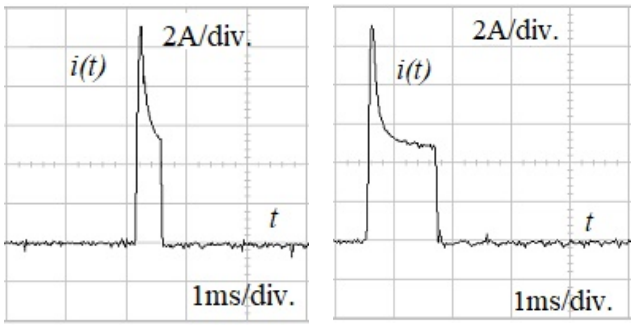

a) b)

Fig. 5. Waveforms of the fuel-injector's current pulses for DI ICEs of fuel for two cases of the fuel-dose control: a) a small amount of fuel, b) a large amount of fuel

4. CONCLUSION

In the paper the fuel-injection mechatronic controller for DI ICEs that provides a very short rise time of the EFI's electromagnet solenoid coil current in the excitation phase of opening without the use of initial-load phase, which improves the reliability of the electronic driver and simplifies its construction, is presented.

Thanks to the numerous advantages of the above-described fuel-injection mechatronic control system and method for controlling the fuel injection can be utilized for DI ICEs with the EFIs suitable for different liquid and/or gas fuels, for example, gasoline, diesel-oil, alcohol, methane, liquefied petroleum gas (LPG) and so on.

REFERENCES

1. **Achleitner E., Bcker H., Funaioli A.** (2007), Direct injection systems for otto engines.,*SAE Technical Paper,* 2007-01-1416.
2. **Berndorfer A., Breuer S., Piock W., Bacho P.** (2013), Diffusion Combustion Phenomena in GDi Engines caused by Injection Process, *SAE Technical Paper,* 2013-01-0261.
3. **Bosch R.** (2014*)*, *Automotive Electrics and Automotive Electronics*, *Springer Vieweg*, 5th Edition, *Springer*, Germany,
4. **Boudy F., Seers P.** (2009), Impact of physical properties of biodiesel on the injection process in a common-rail direct injection system, *Energy Conversion and Management*, 50(12), 2905-2912.
5. **Chatlatanagulchai W., Yaovaja K., Rhienprayoon S., Wannatong K.** (2010), Gain-scheduling integrator-augmented sliding-mode control of common-rail pressure in dieseldual-fuel engine, *SAE Technical Paper*, 2010-01-1573.
6. **Chen H., Gong X., Liu Q. F., Hu Y. F.** (2014), Triple-step method to design nonlinear controller for rail pressure of gasoline direct injection engines, *IET Control Theory & Applications*, 8(11), 948-959.
7. **Chladny R.R., Koch C.R.,** (2008), Flatness-based tracking of an electromechanical variable valve timing actuator with disturbance observer feedforward compensation, *IEEE Transactions on Control Systems Technology*, 16(4), 652 – 663.
8. **Como M., Savaresi S.M., Scattolini R., Comignaghi E., Sofia M., Palma A., Eduardo Sepe E.** (2008), Modelling, parameter identification and dynamics analysis of a common rail injection system for gasoline engines, *Proceedings of the 17th IFAC World Congress*, 8481-8486, Seoul, Korea.

9. **Gaeta A., Fiengo G., Palladino A., Giglio V.** (2009), A control oriented model of a common-rail system for gasoline direct injection engine, *Proceedings of the 28th Chinese Control Conference*, 6614-6619, Shanghai, China.
10. **Gaeta A., Montanaro U. , Fiengo G. , Palladino A & Giglio V.** (2012), A model-based gain scheduling approach for controlling the common-rail system for GDI engines, *International Journal of Control*, 85(4), 419-436.
11. **Gaeta, A., Montanaro, U., Giglio, V.** (2011), Model-based Control of the AFR for GDI Engines via Advanced Co-simulation: An Approach to Reduce the Development Cycle of Engine Control Systems, *Journal of Dynamic Systems, Measurement, and Control*, 133, 061006 (1-17).
12. **Giorgetti N., Ripaccioli G., Bemporad A., Kolmanovsky I., and Hrovat D.** (2006), Hybrid model predictive control of direct injection stratified charge engines, *IEEE/ASME Transactions on Mechatronics*, 11(5), 499-506.
13. **Gupta, V.K., Zhang Z., Sun Z.** (2011), Modeling and control of a novel pressure regulation mechanism for common rail fuel injection systems, *Applied Mathematical Modelling*, 35(7), 3473-3483.
14. **Hoffmann G., Befrui B., Berndorfer A., Piock W. and Varble D**. (2014), Varble Fuel System Pressure Increase for Enhanced Performance of GDi Multi Hole Injection Systems, *Delphi Automotive* Published 04/01/2014 Copyright © *2014 SAE International J. Engines.*
15. **Husted H., Spegar T., Spakowski J.** (2014), The Effects of GDi Fuel Pressure on Fuel Economy, *SAE Technical Paper*, 2014-01-1438.
16. **Jiangjian A., Gao Xiyan B., Yao Chunde C.** (2006), An Experimental Study on Fuel Injection System and Emission of a Small GDI Engine, Proceedings of the *2nd IEEE/ASME International Conference on Mechatronic and Embedded Systems and Applications*, 1-6.
17. **Lino P., Maione B., Rizzo A.** (2007), Nonlinear modelling and control of a common rail injection system for diesel engines, *Applied Mathematical Modelling*, 31(9), 1770-1784.
18. **Montanaro U., Gaeta A., Giglio V.** (2011), An MRAC approach for tracking and ripple attenuation of the common rail pressure for GDI engines, *Proceedings of the 18th IFAC World Congress*, 4173–4180, Milano, Italy.
19. **Ra Y., Loeper, P., Andrie, M., Krieger, R., David E. Foster D. , Reitz R. and Durrett R.** (2012), Gasoline DICI Engine Operation in the LTC Regime Using Triple-Pulse Injection, *SAE Int. J. Engines*, 5(3), 1109-1132.
20. **Sellnau M., Sinnamon J., Hoyer K., Husted H.** (2012), Full-Time Gasoline Direct-Injection Compression Ignition (GDCI) for High Efficiency and Low NOx and PM, *SAE Int. J. Engines*, 5(2), 300-314.
21. **Sellnau M., Sinnamon J., Hoyer K., Kim, J., Cavotta M. and Harry Husted H.** (2013), Part-Load Operation of Gasoline Direct-Injection Compression Ignition (GDCI) Engine, *SAE Technical Paper*, 2013-01-0272.
22. **Sun Z-Y., Zhao J., ShiLeonid Y. and Ma G.** (2015), Numerical investigation on transient flow and cavitation characteristic within nozzle during the oil drainage process for a high-pressure common-rail DI diesel engine, *Energy Conversion and Management*, 98, 507-517.
23. **Tang H.J., Weng L., Dong Z.Y., Yan R.** (2009), Adaptive and learning control for SI engine model with uncertainties, *IEEE/ASME Transactions on Mechatronics*, 14, 93-104.
24. **Wen-Chang T., Peng-Cheng Y.,** (2011), Design of the Electrical Drive for the High-Pressure GDI Injector in a 500cc Motorbike Engine, *International Journal of Engineering and Industries*, 2(1), 70-83.
25. **Yan F., Wang J.** (2011), Common rail injection system iteractive learning control based parameter calibration for accurate fuel injection quantity control, *International Journal of Automotive Technology*, 12(2), 149-157.
26. **Zhao H.** (2016) Advanced Direct Injection Combustion Engine Technologies and Development, *Elsevier*, Amsterdam.

sciendo

DOI 10.2478/ama-2018-0043

acta mechanica et automatica, vol.12 no.4 (2018)

CROSSING AXES OF WORKPIECE AND TOOL AT GRINDING OF THE CIRCULAR TROUGH WITH VARIABLE PROFILE

Volodimyr KALCHENKO*, Andrij YEROSHENKO*, Sergiy BOYKO*

*Chernihiv National University of Technology, Mechanical Engineering Department, 95 Shevchenko street, Chernihiv, Ukraine

vvkalchenko74@gmail.com, yeroshenkoam@gmail.com, svboyko.cstu@gmail.com

received 11 April 2017, revised 7 December 2018, accepted 11 December 2018

Abstract: In the article the method of grinding with crossed axes of the tool and the workpiece got further developed. The work discloses a method of processing details having an external surface with a profile in the form of an arc of a circle of variable radius (for example, rolls of pipe rolling mills). The particular three-dimensional geometric models of the processing, shaping and profiling of abrasive wheels have been developed. A method for controlling the grinding process, which ensures the removal of allowances along equidistant curves has been offered. The developed method of grinding provides a constant depth of cutting according to the coordinate of profile processing. This is achieved at the expense of the synchronous inclination of the wheel and its insertion by the size of the allowance. The diameter of grinding wheel affects on the maximum angle of orientation of the wheel has been proven. It has been shown that increasing the diameter of the abrasive wheel has led to a slight decrease in value orientation angle.

Key words: Circular Trough, Grinding, Equidistant Curves, Cutting Edge, Abrasive Surface, Abrasive Materials, Crossed Axes, Abrasive Wheel, Orientation Angle, Grinding Performance

1. INTRODUCTION

Details having the shape as bodies of rotation with a profile in the form of a circular arc or spiral surface are widespread in modern engineering. As examples of the ring bearings, spindles, rollers of the tube mills, the mandrel cold rolling tubes. To working surfaces of these details there are high demands on the geometrical accuracy and surface quality (Grabchenko et al., 2016). Finishing profiles of these details are carried by grinding.

The most efficient method of grinding surfaces of rotation with a profile in the form of a circular arc shaping is by copying. This method is characterized by high efficiency and simplicity of shaping movements. But this method has several disadvantages:

- Uneven specific load and thickness of the cutting layer along the profile of the abrasive tool, which results in uneven wear (Abidi et al., 2013; Anderson et al., 2011);
- Variable processing capacity in the process of infeed, maximum value of filing per rotation is determined at the time of forming the center point of the profile (Cong Sun et al., 2018);
- The temperature at the area of processing edge portions of part profile is a limiting factor, because the ratio of the thickness of the cutting layer az to the radius of cutting edge ρ does not exceed 0.1, which leads to increased friction. For example, when processing the bearing rings, the edge portions of the profile have a large inclination with respect to the rotation axis of a detail, for them, the contact arc at processing is more than the initial arc. Contact is carried throughout the profile length (Peng et al., 2016; Kalchenko et al., 2016);
- infeed length $l = \delta / cos\theta_{max}$ greater than allowance for processing δ and depends on the maximum angle of ascent profile forming θ_{max} (Tian et al., 2015).

Using method-oriented processing tool which further changes the angular orientation relative to the detail, can eliminate these shortcomings. Material removal is done by lateral movement of the wheel and its rotation in the plane in which the axis of wheel rotation and detail are located.

Consider the process of form-building processing roll rolling for manufacturing thin-walled seamless tubes, which has a profile in the form of a circle arc and requires high geometric accuracy and quality of processing.

Thin-walled seamless tubes are made by cold rolling at tube mills. In order to get high quality tubes it has to be ensured with high accuracy of form-building elements of states. The basic elements – is a tube-roll which has an annular trough, which forms a tube directly. The working part of the trough consists of a pressing area and a calibrating area. The tube is deformed on pressing area, which has a variable profile (Stepien, 2009; Kalpana, Arunachalam. 2018). The calibration roll trough section has a constant radius of a form-building surface. No matter what area is that, the center of trough profile has a constant radius centered on the axis of the roll rotation (Grabchenko et al., 2016).

Finishing roll trough is performed by grinding. Rolls are made of alloy tool steel and tempering to the hardness of HRC 58-62. To produce high-quality thin-walled tubes, trough profile deviation on calibrating area should be within 0,01-0,03 mm and roughness should be Ra 0,63-0,32 μm. The allowance for final polishing should not exceed 0.3-0.5 mm (Grabchenko et al., 2016).

At the present stage for processing of variable troughs profile mainly are used two basic techniques: rounding and touch.

For grinding by a method of rounding the processing is performed by grinding wheel that has a profile in a shape of arc of a grinding wheel, which center moves on equidistance to the profile. The shaping occurs with parallel axis of the roll and grinding wheel which lies in one plane. The main disadvantage of this method is the shaping of the contact point of the grinding wheel and workpiece, which significantly reduces the processing performance. This method of processing is implemented on grinding machines.

The method of the touch is realized by using special constructions of machines that allow the tool to rotate around a vertical axis. The radius of axial profile of grinding wheel is equal to the radius of calibration area of trough. Therefore, the shaping of this area is carried out by a method of copying with a contact line, which increases productivity and the quality finishes. The shape crimping area that has a variable trough profile is carried out by rounding point of a contact, which reduces the performance compared to processing trough with a constant radius of the profile (Grabchenko et al., 2016; Li, Axinte 2016).

The analysis of existing methods showed that at this stage there is no way for grinding rolls with a variable profile which would allow the process by copying not only the calibrating area which has a constant radius of a profile but also crimping.

All these ways of grinding trough variable profile are carried out within two operations. This leads to the formation of the transition that reduces the quality of a shaping tube. This error specifically impacts the roll at the calibration area.

Thus, the aim of this work is to develop a method of grinding, which increases the accuracy of the roll shaping and processing performance through the use of a method of copying on crimping and calibration trough sections with a linear contact of instrument and workpiece. It is necessary to develop modular 3D models of profiling of abrasive grinding wheel, shaping and removal allowance that provide the processing by the equidistant curves.

2. DEVELOPMENT OF THE TROUGH MODEL

The mathematical description of nominal workpiece surface can be performed by spherical module:

$$\overline{r}_w = S^w_{\theta \cdot y_w \cdot \varphi_w \cdot y_p} \cdot e^{-4}, \quad (1)$$

where: $\overline{r}_w$ – is the radius vector of the surface of the ring trough with variable profile of rolling roll; $S^w_{\theta \cdot y_w \cdot \varphi_w \cdot y_p}$ – spherical module is a matrix of switching from the starting point in a coordinate system of the workpiece; $e^{-4} = (0,0,0,1)^T$ – radius vector of starting point (Grabchenko et al., 2016; Kacalak et al., 2013, Kacalak W., Budniak Z., 2015; Uhlmann et al., 2016).

Spherical module of workpiece is a product of one-coordinate matrix M_2 - moves along the axis *OY*, M_6 and M_4 - turns about *OZ* and *OX* axes, respectively:

$$S^w_{\theta \cdot y_w \cdot \varphi_w \cdot y_p} = M_6(\theta_w) \cdot M_2(y_w) \cdot M_4(\varphi_w) \cdot M_2(y_p),$$

where θ_w – is the angle of rotation around the axis of the workpiece rotation (Fig. 2); y_w – is the distance from the center of the profile to the axis of the workpiece rotation; φ_w – is the angle of rotation around the axis of *OX*; $y_p = \rho$ – is the radius profile of the workpiece. Parameters of the matrices y_w, φ_w, y_p for pressing section of the roll are variables and the functions of the independent parameter θ_w. On the calibration area, where profile is unchanged, they become constant.

$$M_2(y_w) = \begin{pmatrix} 1 & 0 & 0 & 0 \\ 0 & 1 & 0 & y_w \\ 0 & 0 & 1 & 0 \\ 0 & 0 & 0 & 1 \end{pmatrix}, M_2(y_p) = \begin{pmatrix} 1 & 0 & 0 & 0 \\ 0 & 1 & 0 & y_p \\ 0 & 0 & 1 & 0 \\ 0 & 0 & 0 & 1 \end{pmatrix},$$

$$M_4(\varphi_w) = \begin{pmatrix} 1 & 0 & 0 & 0 \\ 0 & cos\varphi_w & -sin\varphi_w & 0 \\ 0 & sin\varphi_w & cos\varphi_w & 0 \\ 0 & 0 & 0 & 1 \end{pmatrix},$$

$$M_6(\theta_w) = \begin{pmatrix} cos\theta_w & -sin\theta_w & 0 & 0 \\ sin\theta_w & cos\theta_w & 0 & 0 \\ 0 & 0 & 1 & 0 \\ 0 & 0 & 0 & 1 \end{pmatrix}.$$

The calculation of the models (1) in the MathCAD allowed to simulate graphic representation of a trough which is a subject to processing. Initial data of processing: trough diameter $D_w = 2R_w = 80$ *mm*, radius of the profile on the calibrating area ρ = 12 mm, tolerance *0.02 mm*, sector angle $\xi = 140^o$, difference of the radii on the crimping area is $\Delta R = 2.5$ *mm*, surface roughness *Ra* = *1.25* microns, the material of workpiece - alloy steel, hardness *HRC = 58 ... 62*, allowance for processing *0.4 mm*. The parameters of the grinding wheel: diameter *150 mm*, grain 40, bunch of ceramic.

The tool radius vector in a modular kind is described through the form of details and transition matrix:

$$\overline{r_t} = M_{tw} \cdot \overline{r}_w, \quad (2)$$

where: M_{tw} – is the transition matrix from the coordinate system of the workpiece to the coordinate system of the tool.

The matrix of transition (2) is the product of two spherical modules:

$$M_{tw} = S^{\varphi_t}_{\theta_t \cdot y_c} \cdot S^O_{\psi}, \quad (3)$$

where: $S^{\varphi_t}_{\theta_t \cdot y_c}$ – is the module of the shape-building of a tool; S^O_{ψ} – is the module of the angular orientation of the tool relative to the details.

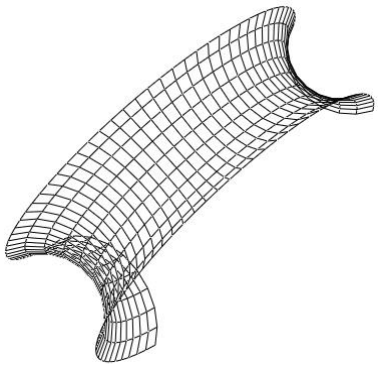

Fig. 1. Model of trough

Orientation module (3) is performed by the matrices of relative rotation:

$$S^{\varphi_t}_{\theta_t \cdot y_c} = M_6(\theta_t) \cdot M_2(y_c), \quad (4)$$

where: θ_t – is the angle of rotation of the workpiece coordinate system relative to the axis of rotation of the tool; y_c – is the distance between the axes of rotation of the tool 1 and workpiece 2 (Fig. 2).

The module of orientation (3) is presented by the matrix of relative rotations:

$$S_{\psi}^{O} = M_5(\psi), \tag{5}$$

where: ψ – is the angle of rotation grinding wheel 1 about the axis which is perpendicular to the axis of rotation of workpiece and tools, and passing through the center of the profile of the

radius ρ, $M_5 = \begin{pmatrix} cos\psi & 0 & sin\psi & 0 \\ 0 & 1 & 0 & 0 \\ -sin\psi & 0 & cos\psi & 0 \\ 0 & 0 & 0 & 1 \end{pmatrix}$. (6)

In processing an annular trough by copying, there occurs a necessity of displacement of grinding wheel in the vertical direction *Δh* which is ensured by a vertical feed *Sv* (Fig. 2). It is caused by a variable radius of the profile on the crimping area of the roll. The shift is made so that the surface of trough and wheel in the central point of contact lines has a common normal line. Therefore, the center of rotation of the wheel *Ot*, the central point of the line of contact *K* and radius center of curvature of the ridge trough *Owj* must lie on one line. On the calibration area where the radius of the curvature bottom of trough is constant and coincides with the axis of rotation of the roll *Ow*, offset value *Δh = 0.*

The final shaping of a pipe is on the calibration area of the roll where the trough radius is the smallest. The tool surface is determined by the condition of the touch wheel with trough on the calibration area. The radius of the axial section of the tool *ρk* must be less than the radius of the workpiece *ρ*. Thus, from now on, the radius vector of the tool $\overline{r_t}$ will be considered for the roll calibration areas where modular model parameters are constant, except the rotation angle of workpiece θ_w.

3. DETERMINATION OF THE TOOL PROFILE

For profiling of the tool it is necessary to make the equation that defines the line of the contact

$$\overline{V} \cdot \overline{n} = 0, \tag{7}$$

where: $\overline{n}$ – is the unit vector of normal line to the workpiece surface; $\overline{V}$ – is the vector of the velocity of the relative motion of the surface in the coordinate system of the tool (Grabchenko et al., 2016; Anderson 2011).

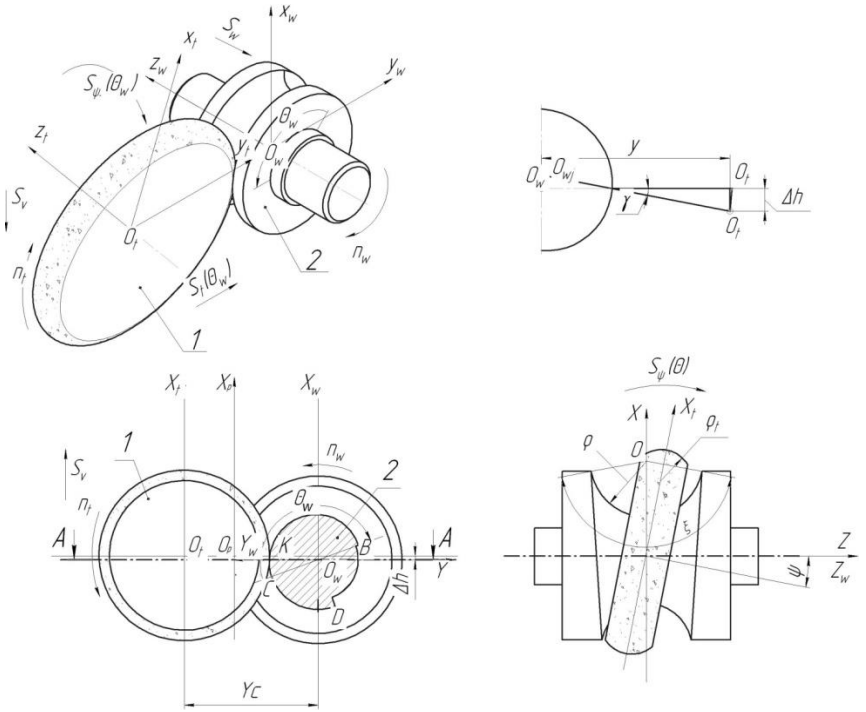

Fig. 2. Scheme of the trough processing with variable profile of roll rolling

The vector of the normal, as we know, can be found as the vector product of vectors tangent to the surface (Chi, Li. 2012; Yanlong et al., 2013; Rabiey, Zhi Wei. 2018). There is a need to differentiate the normal radius vector of the workpiece surface on both parameters.

During the one-parametric rounding (Grabchenko et al., 2016; Kalchenko et al., 2017) relationship between the parameters ψ_w, θ and τ_w equal to zero of a mixed product of three vectors that are derived of the vector $\overline{r_t}$.

$$\left(\frac{\partial \overline{r_t}}{\partial \psi_w} \times \frac{\partial \overline{r_t}}{\partial \theta}\right) \cdot \frac{\partial \overline{r_t}}{\partial \tau_w} = 0, \tag{8}$$

where: $\left(\frac{\partial \overline{r_t}}{\partial \psi_w} \times \frac{\partial \overline{r_t}}{\partial \theta}\right) = \overline{n}$ – is the vector normal to the surface of the workpiece at the point with curvilinear coordinates ψ_w, θ. The value ψ_w is determined from the condition of tangency the surface of the tool with the workpiece surface, and is the maximum value of ψ.

DOI 10.2478/ama-2018-0043

$\frac{\partial \overline{r_t}}{\partial \tau_w} = \overline{V}$ – is the vector of velocity of relative motion of the surface in the coordinate system of the tool; τ_w – is the time of moving the workpiece, while turning it at the angle θ_t in the opposite motion an axis OtZt of the wheel.

The velocity of the workpiece regarding the wheel determined by a matrix of transition from the workpiece coordinate system in the tool coordinate system:

$$\frac{\partial \overline{r_t}}{\partial \tau_w} = \frac{\partial M_6(\theta_w)}{\partial \theta_w} \cdot \frac{\partial \theta_w}{\partial \tau_w} \cdot M_{tw}, \tag{9}$$

where: $\frac{\partial \theta_w}{\partial \tau_w} = \overline{\omega_{tw}}$ is the angular velocity of the workpiece rotation relative to the axis of the wheel.

The radius vector $\overline{r_t}$ describes a set of tool surfaces. The choice of a rational surface is carried on the analysis of the geometric parameters of the outer surface of the workpiece and allowance, which is removed (Fig. 2).

The radius vector of the tool can be presented by a spherical module that is similar to the same module of the workpiece (1), but with its own parameters

$$\overline{r}_t = S^t_{\theta_t \cdot y_t \cdot \varphi_t \cdot y_{pt}} \cdot e^{-4}, \tag{10}$$

$$S^t_{\theta_t \cdot y_t \cdot \varphi_t \cdot y_{pt}} = M_6(\theta_t) \cdot M_2(y_t) \cdot M_4(\varphi_t) \cdot M_2(y_{pt}),$$

where: $\overline{r}_t$ – is the radius vector of the surface of the wheel; $S^t_{\theta_t \cdot y_t \cdot \varphi_t \cdot y_{pt}}$ – is the spherical module, that is a matrix of transition from the starting point to the coordinate system of the tool; θ_t – is the angle of turning around the axis *OtZt* of rotation of the tool; $y_t = R_t$ – is the distance from the center of the profile of the tool to its axis of rotation; φ_t – is angle of rotation around the axis *OtXt*; $y_{pt} = \rho_t$ – is the radius wheel profile (Fig. 3).

Model (10) provides the possibility to determine the coordinates of the profile wheel, which is shown in Fig. 3.

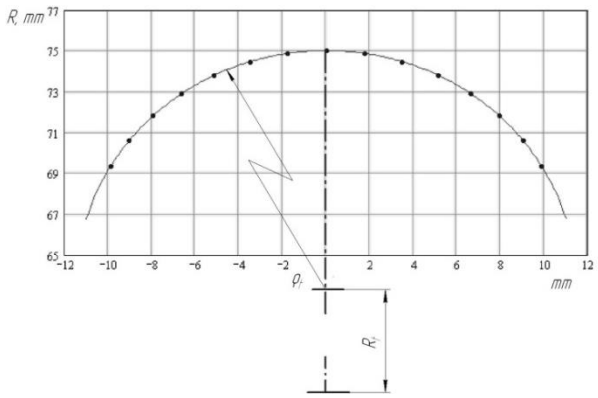

Fig. 3. Profile of the tool

In processing the crimping area, the angle of the wheel is constantly changing with the change of the radius of the trough, reaching a maximum inclination of at the beginning of the crimping area of the roll. The angle at each point of the ridge is determined according to the condition of a minimum deviation of the radius projection of the line of contact on the axial plane from the radius of profile trough.

Fig. 4 shows a sweep of lines of the contact of the tool and the workpiece for various angles of the wheel while processing trough with the parameters listed above.

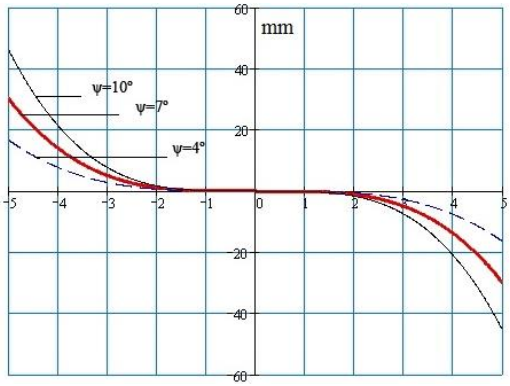

Fig. 4. The contact line of the wheel and the workpiece while grinding by the oriented tool

The radius vector of an annular trough rolling with a variable profile of the roll that is formed after processing by the tool that is described by model (5) can be presented by two spherical modules and the radius vector of the tool:

$$\overline{r_{wt}} = S^{\varphi}_{\theta_w \cdot y} \cdot S^{O}_{\psi \cdot x} \cdot \overline{r_t}, \tag{11}$$

where: $S^{\varphi}_{\theta_w \cdot y} = M_6(\theta_w) \cdot M_2(-y_c + a \cdot \theta - t \cdot k)$ – is the shaping module of details; θ_w – is the angle of rotation coordinate system of the tool around the axis of rotation of the workpiece; $y = -y_c + a \cdot \theta - t \cdot k$ – the current coordinate interaxal distance of the tool and workpieces; $a = \frac{t}{2\pi}$ – is the constant of Archimedean spiral, which moves in relative motion wheel when removing of the allowance; t – is the value of traverse wheel in the direction perpendicular to the axis OwZw of workpiece rotation on each of its turnover; k – is the number of working moves required to remove the allowance; $S^{O}_{\psi \cdot x} = M_5(\pm\psi) \cdot M_1(x)$ – is the module of the angular orientation of the tool relative to the workpiece.

Processing of crimping area of the trough will be conducted with an error that is caused by a mismatch of the radii of the trough profile and projection of the contact line on the axial plane that passes through the point of the contact at the bottom of the trough. Thus, trough profile processing will be carried out by successive clarifying: the maximum error of processing will be expressed at the beginning of the crimping area of the roll Δ and will gradually decrease in the direction of the calibration area (area F1) and will reach the zero value (Fig. 5). It should be noted that regardless of the plot which is processed, the bottom of trough is formed without an error. The value of the error Δ is determined by the method of least squares and must lie within the tolerance of processing.

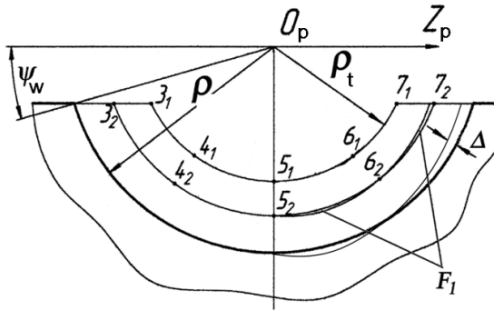

Fig.5. The scheme of the trough profile clarifying

During the processing (Fig. 6) the bottom of the trough 1, the wheel 3 moves along the equidistant relative motion of the tool center 2. The normal 4 passes through the center wheel, the point of contact at the bottom of trough and the center of the radius curvature.

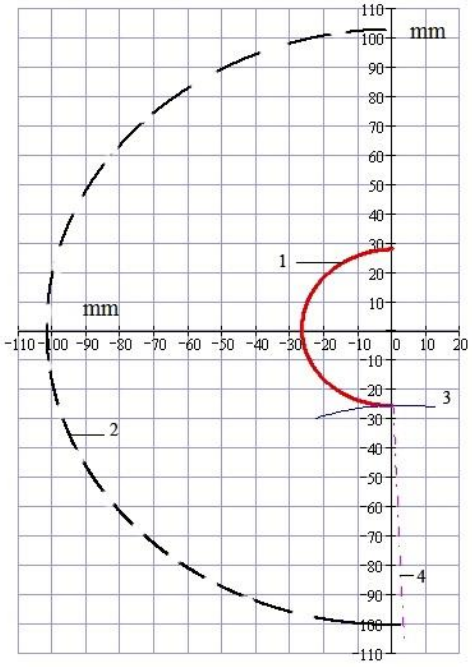

Fig .6. The scheme of the trough processing

4. CONCLUSIONS

The 3D module models of allowance removal, shaping and profiling tools have been developed. New method of grinding by copying with a linear contact of the wheel and workpiece on calibration and crimping areas of trough roller, based on the analysis of these models, which significantly increases processing performance, has been developed.

Based on the analysis of models the method of managing the process of grinding, which provides for removal allowance by equidistantly curves has been proposed. The constant cutting depth profile of the coordinate processing is achieved by simultaneous cutting and turning wheel by the amount of allowance processing, which improves the performance of grinding.

The diameter of the grinding wheel affects the maximum value of the orientation angle ψ. By increasing the diameter of the grinding wheel the value ψ slightly decreased.

Increasing the central angle θ leads to a significant decrease of the orientation angle ψ. Thus the profile of the tool approaches the workpiece profile.

The developed modular models can be used to determine:

- the efficiency of processing by the oriented tool;
- the optimal crossing angle during the cutting;
- other parameters of forming curved surfaces of the revolution;
- thickness of the layer, which is cut off by cutting edge.

REFERENCES

1. **Abidi H., Rezaei S.M., Sarhan A.A.D.** (2013), Analitycal modeling of grinding wheel loading phenomena, *International Journal of Advanced Manufacturing Technology*, 68(1-4), 473-485.
2. **Anderson D., Warkentin A., Bauer R.** (2011), Experimental and numerical investigations of single abrasive-grain cutting, *International Journal of Machine Tools & Manufacture*, 51, 898-910.
3. **Chang H.-C., Wang J.-J.J.** (2008), A stochastic grinding force model considering random grit distribution, *International Journal of Machine Tools & Manufacture*, 48, 1335-1344.
4. **Chi Y., Li H.** (2012), Simulation and analysis of grinding wheel based on Gaussian mixture model, *Frontiers of Mechanical Engineering*, 7(4), 427-432.
5. **Cong S., Yansheng D., Dongxue L., Shichao X..** (2018), Modeling and predicting ground surface topography on grinding chatter, *Procedia CIRP*, 71, 364-369.
6. **Grabchenko A.I., Kalchenko V.I., Kalchenko V.V.** (2016), Grinding with crossed axes of tool and workpice (in Russian), Chernihiv, CHNTU.
7. **Gu W.B., Yao Z.Q., Li H.L.** (2011), Investigation of grinding modes in horizontal surface grinding of optical glass BK7, *J Mater Process Technol.*, 211(10), 1629-1636.
8. **Kacalak W., Budniak Z.** (2015), Modelowanie i analizy szlifowania powierzchni śrubowych wzintegrowanym środowisku cad/cae cad/cae, *Inżynieria Maszyn*, R. 20, z. 1, 19-32.
9. **Kacalak W., Tandecka K., Sempruch R.,** (2013), Modeling research of Microcutting process, *Mechanik*, 8-9, 189-202/702 (in Polish).
10. **Kalchenko V., Yeroshenko A., Boyko S., Sira N.** (2017), Determination of cutting forces in grinding with crossed axes of tool and workpiece, *Acta Mechanica et Automatica*, 11(1),58-63.
11. **Kalchenko V., Yeroshenko A., Sira N.** (2016), Theoretical and experimental study of the process of removal allowance, wear wheel, precision shaping and thermal stress during grinding of cylindrical and staircase shafts with crossed axes of wheel and workpiece (in Ukrainian), *Technical sciences and technology*, 4(6), 35-43.
12. **Kalpana K., Arunachalam N.** (2018), Grinding wheel redress life estimation using force and surface texture analysis. *Procedia CIRP*, 72, 1439-1444.
13. **Li H.N., Axinte D.** (2016), Textured grinding wheels: A review, *International Journal of Machine Tools and Manufacture*, 109, 8-35.
14. **Peng Y., Dai Y., Song C., Shi F.** (2016), Tool deflection model and profile error control in helix path contour grinding, *International Journal of Machine Tools and Manufacture*, 111, 1-8.
15. **Rabiey M., Joseph Lee Z.W.** (2018), Simulation of workpiece surface roughness after flat grinding by electroplated wheel, *Procedia CIRP*, 77, 303-306.
16. **Stepien P.** (2009). A probabilistic model of the grinding process. *Applied Mathematical Modelling*, 33, 3863-3884.
17. **Tian L., Fu Y., Xu J., Li H., Ding W.** (2015), The influence of speed on material removal mechanism in high speed grinding with single grit, *International Journal of Machine Tools and Manufacture*, 89, 192-201.
18. **Uhlmann E., Koprowski S., Weingaertner W.L., Rolon D.A.** (2016), Modelling and Simulation of Grinding Processes with Mounted Points: Part II of II - Fast Modelling Method for Workpiece Surface Prediction. *Procedia CIRP*, 46, 603-606.
19. **Yan L., Rong Y.M., Jiang F., Zhou Z.X.** (2011), Three-dimension surface characterization of grinding wheel using white light interferometer. *International Journal of Advanced Manufacturing Technology,* 55, 133-141.
20. **Yanlong C., Jiayan G., Bo L., Xiaolong C., Jiangxin Y., Chunbiao G..** (2013), Modeling and simulation of grinding surface topography considering wheel vibration. *The International Journal of Advanced Manufacturing Technology*, 66(5–8), 937-945.

DOI 10.2478/ama-2018-0044

COMPARISON ANALYSIS OF COCKROFT – LATHAM CRITERION VALUES OF COMMERCIAL PLASTICINE AND C45 STEEL

Łukasz WÓJCIK*, Zbigniew PATER*

*Lublin University of Technology, Mechanical Engineering Faculty, Nadbystrzycka 36, 20-618 Lublin, Poland

l.wojcik@pollub.pl, z.pater@pollub.pl

received 11 January 2018, revised 14 December 2018, accepted 18 December 2018

Abstract: The paper presents and compares the results of theoretical and experimental research in the field of cracking of model material (commercial plasticine) and C45 steel in hot forming conditions. The aim of the research was to determine the limit values of the Cockroft-Latham integral for both materials. The presented research methodology includes experimental tests (tensile tests) and numerical simulations carried out in the DEFORM-3D program. For laboratory tests, axially symmetric samples made of C45 steel and model material were used. On the basis of the obtained experimental and numerical results, a comparative analysis of both materials was carried out.

Key words: Physical Modelling, Cockroft-Latham Criterion, Plasticine, C45 Steel

1. INTRODUCTION

Solid elements obtained in metal forming processes are often subject to certain limitations. These limitations include material cracking occurring during its plastic working. These cracks are often invisible to the human eye, but have a very negative effect on the final product. The safety of people and things depends on the location, size and propagation of cracks. The paper (Antolik, 2014) presents the method of detecting cracks in finished elements and the impact of cracks on the user's safety.

There are two ways to break materials, they are brittle and ductile. In papers (Altan et al., 1996; Arikawa and Kakimotoa, 2014; Charoensuk et al., 2017, Cockroft and Latham,1968; Gontarz and Piesiak, 2010; Lis et al., 2018;Pires et al., 2016), the authors described the most common type of cracking method in hot plastic parts - ductile fracture. Plastic cracks occur as a result of the formation of cracks and necking of the matrix. In the case of non-metallic materials, the role of gaps is played by voids and gas bubbles created as a result of material production.

Currently, simulation programs (numerical) are the most frequently used tools to predict the place and type of cracks. This method is based on numerical modeling, it consists of replacing the actual model with a discrete model. The discrete model, on the other hand, is composed of a finite number of elements and nodes. The paper (Gontarz and Winiarski, 2015) presents a method of using computer simulations for testing and analysis of the process of extrusion of hollow elements with a movable sleeve.

Numerical methods allow obtaining results for elements with complicated shapes, where numerical calculations are often impossible. Computer simulations are characterized by the ease of testing. The main limitation of the numerical method is the uncertainty of the obtained results.

Another method used for researching and analyzing the process of plastic forming is physical modeling. Physical modeling is a method that facilitates the analysis and testing of technological processes.

The idea of physical modeling is to replace the real material with a model material. Model materials are divided into two groups: a group of metallic materials (including tin, lead, sodium) and a group of non-metallic materials (including plasticine, wax, resin). More information on model materials is presented in articles (Bylya, Davey and Krishnamurthy, 2017;Kowalczyk, 1995; Mizuno and Komori, 2009; Pater and Wojcik, 2017). This technique is based on four main criteria of similarity: similarity of flow curves for real and model material, similarity of friction conditions, similarity of tool shape and similarity of process kinematics.

In the scientific literature, the results of experimental research (Asai and Kitamura, 2014; Moon and Van Tyne, 2000; Rasty and Sofuoglu, 2000) have been presented many times to determine the mechanical properties of materials used for physical modeling of the hot forming of metal. In the laboratory analyzes, the subject of cracking of model materials was omitted.

In this work, it was considered useful to carry out research on the determination of the limit value of the Cockrofta-Latham integral for commercial plasticine and hot-formed C45 steel

Standardized Crockroft-Latham criterion determines well the moment of the cracking of the extended material, in which necking and next its plastic splitting take part.

According to the standard Cocroft-Latham criterion, the crack occurs when the value of integral (1) exceeds a certain value of C. The constant C is determined separately for each material under specific conditions, the appropriate temperature and strain rate.

$$\int_0^{\varphi^*} \frac{\sigma_1}{\sigma_m} d\varphi = \mathrm{C} \tag{1}$$

where: σ_m – mean stress, σ_1 – the greatest main stress, φ^* – limiting deformation of cracking, C – fixed material

2. MATERIAL AND TESTS METHODOLOGY

The model material used for the research is commercial plasticine based on white and black wax, while C45 steel was used as the real material.

Plasticine is a model material belonging to non-metallic materials. The exact chemical composition of the used plasticine is not known for the patent protection of the finished product. Plasticine is a mixture of clays, oils, waxes and coloring pigments.

The plastic mass used was previously subjected to plastometric tests, the procedure and the results of the tests were presented in the paper (Lis, Pater and Wójcik 2016). Plastometric tests showed high sensitivity to changes in temperature and deformation rate.

Fig. 1 shows a summary of the flow curves for the studied plasticine in the temperature range from 0 to 20˚C with a flow curve obtained for C45 steel shaped at 1150˚C.

The commercial plasticine used for the model tests is described by two constitutive equations (depending on the color), the white plasticine is described by equation (2), while equation (3) describes the black plasticine.

To determine the limit value of the Cockroft-Latham integral, experimental and numerical studies were carried out.

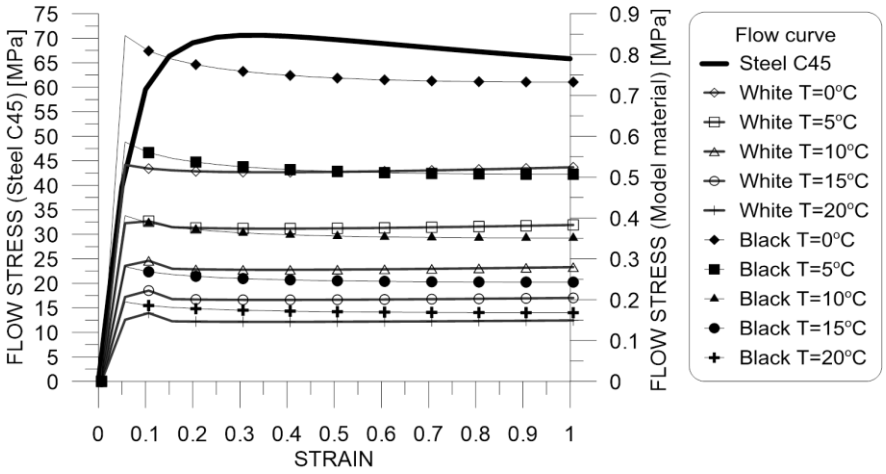

Fig.1. Flow curves for plasticine and C45 steel

$$\sigma_{pl} = 0.48057 \cdot \varepsilon^{-0.0313} \cdot \exp(0.087 \cdot \varepsilon) \cdot \dot{\varepsilon}^{(0.245-0.0026 \cdot T)} \cdot \exp(-0.0328 \cdot T) \quad (2)$$

$$\sigma_{pl} = 0.6817 \cdot \varepsilon^{-0.0711} \cdot \exp(0.072 \cdot \varepsilon) \cdot \dot{\varepsilon}^{(0.2701-0.003 \cdot T)} \cdot \dot{\varepsilon}^{(0.245-0.0026 \cdot T)} \cdot \exp(-0.07358 \cdot T) \quad (3)$$

where: σ_{pl}– yield stress [MPa], ε – equivalent strain, $\dot{\varepsilon}$ – strain rate [s^{-1}], T – sample temperature [°C].

2.1. Experimental tests

Experimental tests used to determine the limiting value of the Cockroft-Latham integral of the model material were carried out on an Instron 3369 testing machine. This machine is characterized by a maximum load of 50 kN. The measuring stand allows the measurement of force with an accuracy of ± 0.5% of the obtained value. The measuring device allows registering the movement of the slider and force as a function of time.

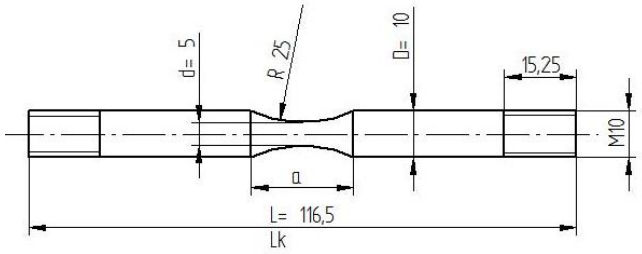

Fig. 2. The shape and dimensions of the sample used for testing (threaded parts refer to samples made of C45 steel

Axial symmetrical samples with constriction were used for experimental tests. The shapes of the samples have been repeat edly described in the articles (Bariani et al., 2014;Derpenski, et al., 2018;Eivani et al., 2018; Fu et al., 2011; Fuertes et al., 2015). The geometrical dimensions of the sample are shown in Fig.2.

In total, 15 plasticine samples of each color were used for experimental tests.

In the papers (Altan and Vazquez, 2000;Assempour et al., 2012;Assempour and Razi, 2003; Cherkashina and Mazur, 2012; Galan and Perig, 2017), the authors presented many different methods for the preparation of test samples. Based on the analysis of these methods, the following procedure for the generation of loads was adopted.

The first stage of sample preparation for experimental tests was heat treatment of plasticine billets supplied from the manufacturer. This treatment consisted of heating the plasticine to the temperature of about 30-35°C. The next step was multiple manual reworking of the material. The use of this operation allowed to get rid of the air bubbles created as a result of production. The presence of bubbles negatively affects the quality of the final sample.

In the next stage, cylindrical bodies were shaped, which were later subjected to the extrusion process, as a result of which a rod with a diameter of 10 mm was obtained.

The obtained rod was then divided into 120 mm long samples. Samples were made by cross-wedge rolling. After the rolling, the samples were cut according to the dimensions shown in Fig.2. The samples were measured and their dimensions are listed in table 1.

In the last part of the preparations, samples from the model material were cooled to temperatures 0, 5, 10, 15, 20˚C for a period of 24 hours; this selected time allowed to obtain the same temperature in the entire sample volume.

Prepared samples for experimental research are shown in Fig. 3.

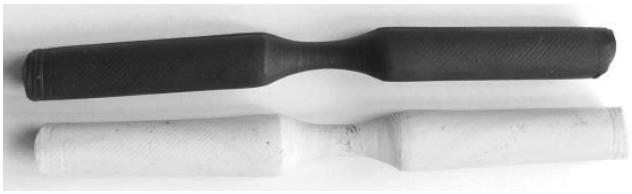

Fig. 3. Samples made of plasticine, used for experimental research

Tab.1. Parameters of samples from model material used for stretching (markings according to Fig. 2)

No.	T [˚C]	D [mm]	d [mm]	a [mm]	L [mm]	L_k [mm]	ΔL [mm]
White Plasticine							
1	0	9.96	4.65	21.7	100.1	105.2	5.1
2		10.19	4.54	21.3	100.5	105.3	4.8
3		10.21	4.60	21.5	100.7	105.1	4.4
1	5	10.1	4.7	20.9	100.7	106.5	5.8
2		10.2	4.65	21.1	100.8	106.4	5.6
3		10.4	4.68	21.6	100.7	105.3	4.6
1	10	10.15	4.64	21.5	100.3	106.7	6.4
2		10.06	4.58	21.7	100.5	107.9	7.4
3		10.21	4.69	21.7	100.5	107.2	6.7
1	15	10.18	4.85	20.9	100.5	109.3	8.8
2		10.3	4.73	21.8	100.3	107.7	7.4
3		10.28	4.78	21.7	100.7	108.6	7.9
1	20	10.13	4.91	21.8	100.6	108.0	7.4
2		10.18	4.75	21.9	100.9	109.9	9.0
3		10.2	4.73	21.2	101	110.2	9.2
Black Plasticine							
1	0	10.10	4.80	21.3	100.7	104.7	4.0
2		10.23	4.99	21.4	100.4	104.8	4.4
3		10.28	5.00	21.2	100.3	104.8	4.5
1	5	10.26	5.02	21.5	100.4	105.9	5.5
2		10.23	4.94	21.6	100.6	105.4	4.8
3		10.21	4.90	21.4	100.3	105.9	5.6
1	10	10.11	4.97	21.5	100.7	106.5	5.8
2		10.19	4.92	21.6	100.4	106.8	6.4
3		10.14	4.96	21.6	100.6	106.6	6.0
1	15	10.20	5.01	22.2	100.8	107.7	6.86
2		10.10	4.94	21.9	100.4	107.1	6.68
3		10.30	5.02	21.8	100.5	107.2	6.68
1	20	10.18	4.94	21.4	100.2	108.0	7.84
2		10.20	4.90	21.9	100.6	108.3	7.72
3		10.20	4.93	21.3	100.9	108.7	7.82

In order to properly fix the sample in the jaws of the testing machine, special inserts were designed and printed to enable it to be accurately captured in Fig.4.

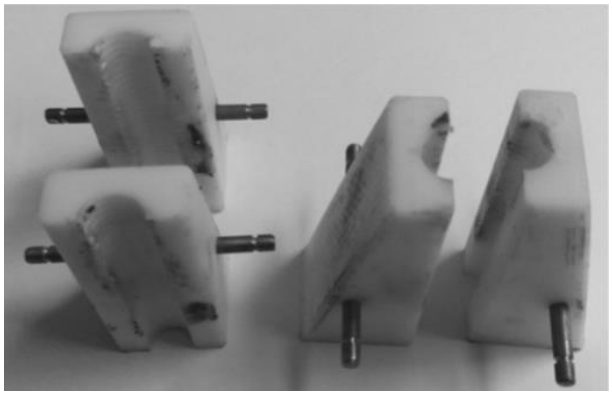

Fig. 4. Sample mounting inserts in a testing machine

The tensile test of samples made of model material proceeded according to the following scheme: cooling samples in a laboratory refrigerator to the test temperature (0, 5, 10, 15, 20˚C) for 24 hours, then stretching with a jaw movement speed of 5 mm/s until breaking, removing the sample.

During the tests, the force and displacement were measured, which corresponded to the displacement of the bar of the testing machine.

Experimental tests of stretching of samples made by machining from C45 steel were carried out in the Gleeble 3800 simulator located at the Faculty of Materials, Process and Applied Physics Engineering at the Częstochowa University of Technology (Fig.5).

The Gleeble 3800 simulator has the following parameters:

- movement speed: up to 2000 m/s,
- maximum pressure: 20 MG,
- heating speed: up to 1000°C/s,
- maximum temperature: 1700°C,
- a resistance heating system for samples,
- tests at reduced pressure or protective atmosphere.

Fig. 5. Physical simulator Gleeble 3800, used in experimental research

Samples of identical shape and geometry as samples made of model material were used for the tests (Fig. 1). The samples were made by machining methods. 12 samples were used for experimental tests, three samples for each temperature

(900°C, 1000°C, 1100°C and 1200°C). The samples were measured and their dimensions are shown in Table 2.

Tab.2. Parameters of samples from, used for stretching (markings according to Fig. 2)

No.	T [°C]	D [mm]	d [mm]	a [mm]	L [mm]	L_k [mm]	ΔL [mm]
1	900	10.25	5.25	22.46	116.6	120.4	3.8
2		10.00	5.00	22.48	116.9	121.1	4.1
3		10.00	5.00	21.86	117.5	121.3	4.4
1	1000	10.05	5.14	22.35	116.5	120.2	3.7
2		10.00	5.00	22.31	116.4	120.4	4.0
3		10.03	5.02	21.73	116.2	120.9	4.7
1	1100	10.13	5.02	22.00	116.4	120.9	4.5
2		10.02	5.00	21.67	116.9	121.7	4.8
3		10.00	5.05	21.91	116.7	120.2	3.5
1	1200	10.15	5.08	22.38	116.5	120.5	4.0
2		10.00	5.00	22.28	116.7	120.7	4.0
3		10.05	5.01	21.97	116.5	121.3	4.8

Fig. 6 presents a set of samples made of C45 steel, used for experimental research.

Fig. 6. A set of samples made of C45 steel used for experimental research

Experimental tests of stretching of C45 specimens were carried out according to the following procedure: heating samples at 10°C/s to test temperature (900°C, 1000°C, 1100°C and 1200°C), withstanding at the target temperature for a period of 5 days s, stretching with the speed of movement of the jaw5 mm / s until it ruptures, removing the sample.

During the tensile test, the force, displacement and temperature of the material in the constriction were recorded.

After the completion of experimental tests carried out on samples made of plasticine and C45 steel, the broken samples were inspected (Fig.7-8)

Fig. 7. View of plasticine samples broken on a testing machine

Fig. 8. View of C45 steel samples broken in a tensile test using the Gleeble 3800 simulator at 1 - 900˚C, 2 - 1000˚C, 3 - 1100˚C, 4 - 1200˚C

2.2. Numerical calculations

To determine the limiting value of the Cockroft-Latham integral, the computer program DEFORM 3D was used. The numerical calculation methodology of the DEFORM 3D program uses the finite element method. The simulation program used has 13 different criteria implemented to determine the occurrence of cracks in the shaped material. Among the criteria available in the program is the normalized Cockroft-Latham criterion.

The standardized Cockroft-Latham criterion was chosen for its popularity in specialized FEM programs for the analysis of plastic forming of metals.

Numerical analysis was carried out for the process of stretching samples made of model material (commercial plasticine) and carbon steel C45.

The results of previous experimental studies were used for numerical studies.

In computer simulations, the geometry of the samples used for experimental studies was modeled in accordance with the geometrical parameters listed in Tab. 1-2.

DOI 10.2478/ama-2018-0044

In order to facilitate the computer simulation, the computer models of the samples were redesigned so that the virtual grips could be mounted (Fig.9). The shape of the ends of the samples does not affect the results, because during stretching the deformations are located in the necking area.

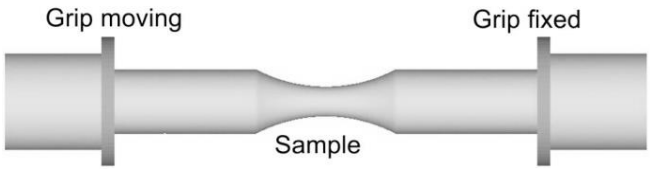

Fig. 9. Sample and mounting system in DEFORM-3D

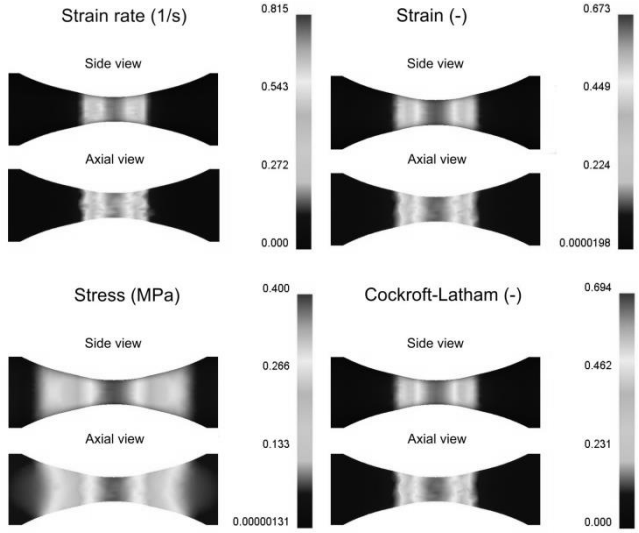

Fig.10. Distributions of intensity of strain rate, strain, stress and failure criterion for model material (white plasticine, T=0˚C)

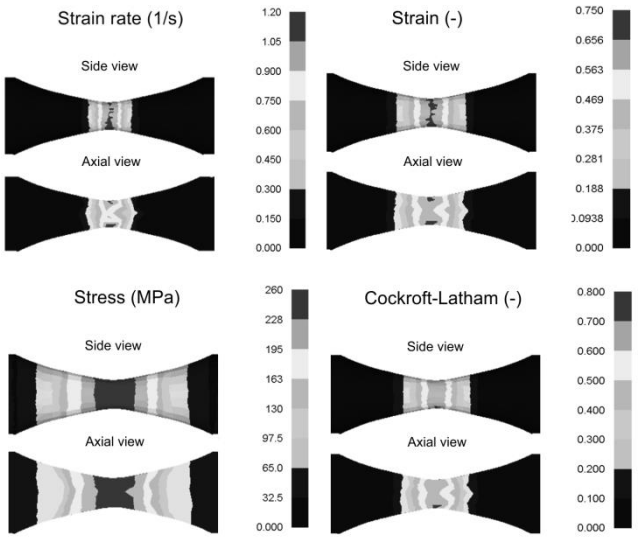

Fig. 11. Distributions of intensity of strain rate, strain, stress and failure criterion for the C45, T=900˚C

For the purpose of computer simulations, it was necessary to model 3D samples which models were imported into the DEFORM 3D solver. The samples prepared in this way were covered with a MES mesh with four-node elements (150,000 items). The material was modeled with a plastic model.

In the tensile calculations of C45 steel samples, a material model was taken from the library of the applied software. However, in the case of model material, own models developed and presented in the paper were used (Lis, Pater and Wójcik, 2016).

The tensile speed and the temperature according to the experimental parameters were adopted for numerical calculations.

Computer simulations allowed to accurately trace the stretching of the sample and determine the forces and maps of strains, stresses, strain rates and the Cockroft-Latham integral.

The use of necking has achieved its goal, for it forced the plastic deformation to be localized here. In the place of necking, the intensity of stress takes the largest values. Then the stresses reach the value of plasticizing stress, and the material suffers permanent deformations (Fig. 10-11).

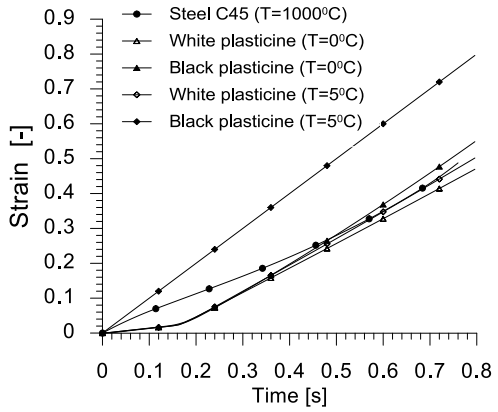

Fig. 12. Change in strain value during elongation of samples

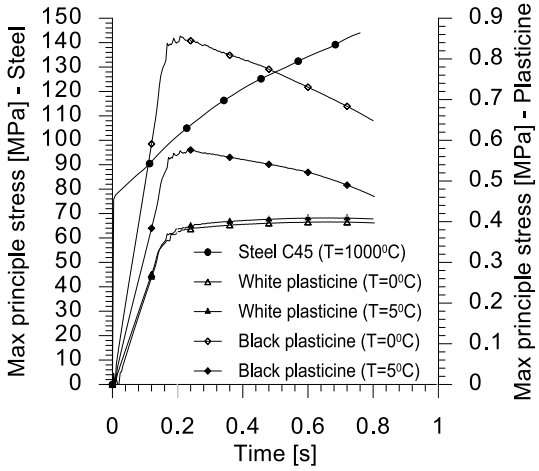

Fig. 13. Change in maximum values of main stresses during elongation of samples

Drawings Fig.12. and Fig. 13 show graphs of the change in strain value and maximum main stresses at a point located on the sample axis in the middle of its length.

The above maps obtained as a result of numerical research were presented, among others, distribution of the Cockroft-Latham integral in the samples subjected to the tensile test. The largest values of the Cockroft-Latham integral were observed in places of necking. Hence, there should be a violation of the consistency of the material. Assuming that the end of the simulation

was the moment in which the sample was broken from the distribution, the value of the boundary integral can be determined.

3. RESULTS

Based on experimental tests and numerical simulations, limit values for the Cockroft-Latham integral (C) for the model material and C45 steel were determined. These values are developed and presented in Tab. 3 and Tab. 4.

Tab. 3. Limit values of Cockrofta-Latham determined for the model material - plasticine

Temp.	No.	Type	Limit values of Cockrofta-Latham determined	
			Attempt	Average
0˚C	1	White	0.694	0.646
	2		0.661	
	3		0.584	
	1	Black	0.627	0.691
	2		0.697	
	3		0.749	
5˚C	1	White	0.868	0.786
	2		0.838	
	3		0.652	
	1	Black	1.180	1.134
	2		0.921	
	3		1.300	
10˚C	1	White	1.150	1.27
	2		1.450	
	3		1.210	
	1	Black	1.120	1.250
	2		1.480	
	3		1.150	
15˚C	1	White	1.500	1.377
	2		1.280	
	3		1.350	
	1	Black	2.100	2.037
	2		2.010	
	3		2.000	
20˚C	1	White	1.230	1.453
	2		1.530	
	3		1.600	
	1	Black	1.970	2.000
	2		2.210	
	3		1.820	

Based on the analysis of the obtained results of the model material, the limit value of the Cockroft-Latham integral has been stigmatized along with the increase in temperature (tab.3). The C values for the temperature range 0 ÷ 15˚C change in the range of 0.646÷1.453 for white material and 0.691÷2.037 for black material.

Tab. 4 shows the limit values of the Cockroft-Latham integral for C45 steel. The data in this Fig. shows that C values vary with temperature.

The limit value of the Cockrofta-Latham integral (C) for the entire temperature range (900°C-1200°C) of the hot forming of C45 steel is C_{gr}=0.756±0.125.

Tab. 4. Limit values of Cockrofta-Latham determined for C45 steel

Temp.	No.	Limit values of Cockrofta-Latham determined	
		Attempt	Average
900˚C	1	0.778	0.849
	2	0.917	
	3	0.853	
1000˚C	1	0.572	0.682
	2	0.645	
	3	0.829	
1100˚C	1	0.864	0.765
	2	0.870	
	3	0.563	
1200˚C	1	0.673	0.726
	2	0.664	
	3	0.842	

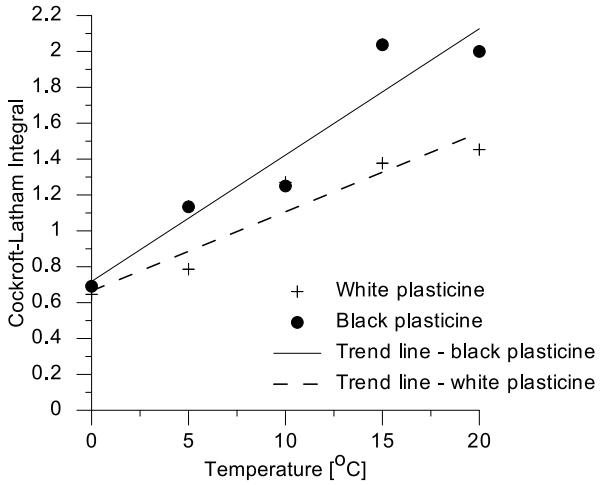

Fig. 14. Limit value of the Cockroft-Latham integral for model materials (commercial plasticine), depending on the temperature

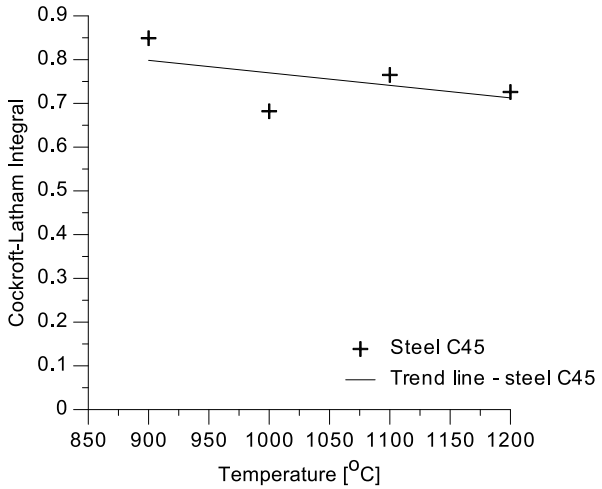

Fig. 15. Limit value of the Cockroft-Latham integral for C45 steel, depending on the temperature

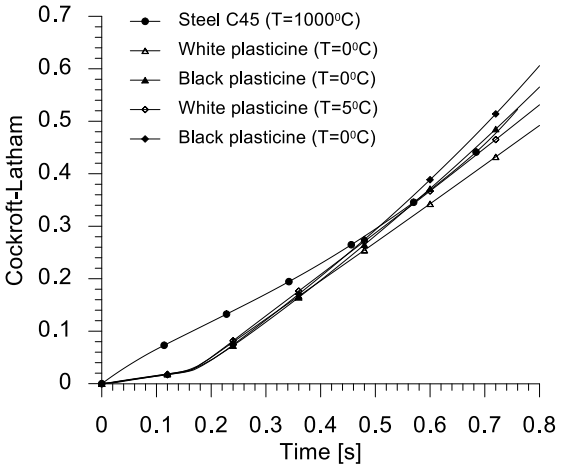

Fig. 16. Change of the Cockroft-Latham integral when elongating samples

Figs 14 and 15 show the average values of the Limits of Cockroft-Latham (C) as a function of temperature. The C trend line for individual materials was also determined on these charts.

The resulting trend lines are described by the following equations:

Black plasticine:

$$C = 0.718 + 0.07T \quad (3)$$

White plasticine:

$$C = 0.665 + 0.44T \quad (4)$$

where: C– limit value of the Cockroft-Latham integral, T– sample temperature [°C].

Fig. 16 shows the change in the value of the Cockroft-Latham integral for samples with the most approximate integral values between the material model and the hot-shaped C45 steel

4. SUMMARY

The paper presents the methodology and results of research aimed at determining the limit value of the Cockroft-Latham integral (C) for the model material (commercial plasticine - two colors) and for hot-formed C45 steel.

The used research method is based on experiments and numerical stretching process. The use of cylindrically shaped samples with constriction allowed to initiate the crack in a predicTab. place.

The limit values of the C-L integral for model materials increase linearly with the temperature increase, while for C45 units, the C values decrease slightly as the temperature rises.

The results of laboratory and numerical tests of the model material and steel of the C45 grade, hot-worked, were compared with each other.

Similarly, the results of the limit value of the Cockroft-Latham integral for heat treated C45 steel at 900°C-1200°C with white plasticine worked in the temperature range of 0°C to 5°C and with black plasticine molded at 0°C were observed. The C values for C45 steel in this temperature range oscillate between 0.849÷0.726. The limit value of the Cockroft-Latham integral for white plasticine processed in the temperature range of 0°C-5°C is 0.850÷0.646 and for black plasticine at 0°C it is equal 0.691.

The conducted research allowed to conclude that it is possible to use white plasticine with a temperature of 0°C-5°C and black at 0°C as a model material for physical examination of hot forming of C45 steel in the field of material cracking modeling.

REFERNCES

1. **Altan T., Breitling J., Taupin E., Wu W-T.** (1996), Material fracture and burr formation in blanking results of FEM simulations and comparison with experiments,*Journal of Materials Processing Technology*, 58, 68-78.
2. **Altan T., Vazquez V.,** (2000), New Concepts in die design - physical and computer modeling applications, *Journal of Materials Processing Technology*, 98, 212-223.
3. **Antolik Ł.,** (2014), Methodology of Fatigue Cracks Detection in Railway Axles in Comparison with European Standards Requirements (in Polish),*Problemy kolejnictwa*, 165, 7-19.
4. **Arikawa T., Kakimoto H.,** (2014), Prediction of surface crack in hot forging by numerical simulation*, Procedia Engineering*, 81, 474-479.
5. **Asai K., Kitamura K.,** (2014), Estimation of frictional property of lubricants for hot forging of steel using low-speed ring compression test, *Procedia Engineering*, 81,1970-1975.
6. **Assempour A., Farahani S., Naybodi A.,** (2012). A general methodology for bearing design in non-symmetric T-shaped sections in extrusion process, *Journal of Materials Processing Technology*, 212(1), 249-261.
7. **Assempour A., Razi S.,** (2002). Determination of load and strain-stress distributions in hot closed die forging using the plasticine modeling technique, Archive of SID, 2(15), 167-172.
8. **Bariani P.F., Bylya O., Ghiotti A. ,Novella M.F.,** (2014), Modelling of AA6082 Ductile Damage Evolution under Hot Rolling Conditions, Procedia Engineering, 81, 221-226.
9. **Bruschi S., Davey K., Krishnamurthy B.,** (2017), Physical modelling for metal forming processes, Procedia Engineering, 207, 1075-1080.
10. **Charoesunk K., Panich S., Uthaisangsuk V.,** (2017). Damage initiation and fracture loci for advances high strength steel sheets taking into account anisotropic behaviour. Journal of Materials Processing Technology, 248, 218-235.
11. **Cherkashina T., Mazur I.,** (2012), Mathematical and Physical Modeling of Soft Cobbing Process of Hot Rolling Steels, Material Science Forum, 704-705, 160-164.
12. **Cockroft M.G., Latham D.J,** (1968). Ductility and the workability of metals,*Journal of the Institute of Metals*, 96, 33-39.
13. **Derpenski L., Seweryn A.,Szusta J.,** (2018), Damage accumulation and ductile fracture modeling of notched specimens under biaxial loading at room temperature, *International Journal of Solids and Structures*, 134, 1-19.
14. **Dziubinska A., Gontarz A.,** (2015), A new method for producing magnesium alloy twin-rib aircraft brackets, *Aircraft Engineering and Aerospace Technology*, 2(87), 180-188.
15. **Eivani A. R., Jafarian H. R.,Mirghasemi S. M., Seyedein S. H.** (2018), A comparison between routine vs. normalized Cockroft-Latham Fracture criteria for prediction of fracture during equal channel angular pressing,*Engineering Fracture Mechanics*, 199, 721-729.
16. **Fu M. W., Li H., Lu J., Yang H.,** (2011), Ductile fracture: Experiments and computations,*International Journal of Plasticity*, 27, 147-180.
17. **Fuertes J. P., León J., Luis C. J., Luri R., Puertas I., Salcedo D.,** (2015), Comparative study of the damage attained with different specimens by FEM,*Procedia Engineering*, 132, 319-325.
18. **Galan I. S., Perig A.V.,** (2017), The experimental verification of the known flow line models describing local flow during ECAE (ECAP), Letters on materials, 7(3), 209-217.

19. **Gontarz A., Piesiak J.,** (2010), Crack model according to Cockroft-Latham criterion for magnesium alloy MA2 in hot forming conditions (in Polish), XXI(4), 217-227.
20. **Gontarz A., Winiarski G.,** (2015), Numerical and experimental study of producing flanges on hollow parts by extrusion with a movable sleeve, Archives of Metallurgy and Materials, 60, 1917-1921.
21. **Kowalczyk L.,** (1995), *Physical modeling of metal forming processes* (in Polish),Technologii Eksploatacji, Radom.
22. **Lis K., Pater Z., Walczuk P., Wojcik L.,**(2018), Preliminary analysis of a rotary compression test, *Adv. Sci. Technol. Res. J*, 12 (2), 77-82.
23. **Lis K., Pater Z., Wojcik L.,**(2016), Plastometric tests for plasticine as physical modelling material, *Open Engineering*, 6, 653-659.
24. **Mizuno K., Komori K.,** (2009), Study on plastic deformation in cone-type rotary piercing process using model piercing mill for modeling clay, *Journal of Materials Processing Technology*, 209, 4994-5001.
25. **Moon Y.H., Van Tyne C.J., (**2000), Validation via FEM and plasticine modeling of upper bound criteria of a process induced side surface defect in forgings, *Journal of Materials Processing Technology*, 99, 185-196
26. **Pater Z., Wojcik L.,**(2017), Physical analysis of cross-wedge rolling process of a stepped shaft,*Adv. Sci. Technol. Res. J.* ,11 (4), 60-67.
27. **Pieres F. M. A., Song N., Wu S.,** (2016), Numerical analysis of damage evolution form materials with tension - compression asymmetry, *Procedia Structural Integrity*, 1, 273-280.
28. **Rasty J., Sofuoglu H.,** (2000), Flow behaviour of plasticine used in physical modeling of metal forming process, *Tribology International*, 33, 523-529.

DOI 10.2478/ama-2018-0045

ESTIMATION OF FLOW RATE THROUGH ANALYSIS OF PIPE VIBRATION

Santhosh K. VENKATA, Bhagya R. NAVADA

Department of Instrumentation and Control Engineering, Manipal Institute of Technology,
Manipal Academy of Higher Education, Manipal 576104, India.

kv.santhu@gmail.com, kgbagya@gmail.com

received 9 September 2018, revised 15 December 2018, accepted 19 December 2018

Abstract: In this paper, implementation of soft sensing technique for measurement of fluid flow rate is reported. The objective of the paper is to design an estimator to physically measure the flow in pipe by analysing the vibration on the walls of the pipe. Commonly used head type flow meter causes obstruction to the flow and measurement would depend on the placement of these sensors. In the proposed technique vibration sensor is bonded on the pipe of liquid flow. It is observed that vibration in the pipe varies with the control action of stem. Single axis accelerometer is used to acquire vibration signal from pipe, signal is passed from the sensor to the system for processing. Basic techniques like filtering, amplification, and Fourier transform are used to process the signal. The obtained transform is trained using neural network algorithm to estimate the fluid flow rate. Artificial neural network is designed using back propagation with artificial bee colony algorithm. Designed estimator after being incorporated in practical setup is subjected to test and the result obtained shows successful estimation of flow rate with the root mean square percentage error of 0.667.

Key words: Accelerometer, Estimation, Frequency Response, Flow Rate, Neural Network, Vibration

1. INTRODUCTION

Flow process loops are found in almost all kinds of process industry starting from petroleum to diary, pharmaceutical, dye making, food and beverage industries and so on. Objective of these flow process is primarily to control flow rate or control secondary parameters like liquid level, temperature etc. Monitoring of the process is key requirement for obtaining the appropriate end product. To have a good monitoring system, obtaining information at each and every part of the process is essential. For measuring these parameters sensors are essential. A brief study is carried on, to understand various flow sensors.

A number of researchers have reported work in the area of measurement of flow some of those have been discussed below. Marick et al., (2014) have reported a method of flow measurement without disturbing the flow in a pipeline is. This consists of two gauges, one for measurement of static pressure and the other for online fluid pressure measurement. Difference between these two pressures were used to find the flow rate of the fluid. Measured pressure is converted into electrical quantity by using inductive transducer. A non-contact type flow rate measurement system is reported by Sinha et al. (2015). In this method, a Hall Effect sensor is used to measure the variation in flow rate. Hall probe was located on top of the rotameter thus change in movement of magnetic float influences output voltage of Hall Effect sensor. Based on these variations, flow rate was measured. An optical method of flow measurement is reported by Norgia et al. (2016), using a laser diode for observing the laser divergence. In this method, measurement of flow is based on Doppler shift due to particles present in the fluid and self-mixing ability of laser diode. A device for flow measurement using Bragg's grating is reported by Kirwan et al. (2016). In this method, movement of cantilever arm is measured due to fluid momentum flowing in round pipe elbow. Output of grating was shown highly associated to the flow rate through pipe and also was stated independent of temperature and static pressure. Measurement of fluid flow through a pipe using fringing field capacitors is reported by Liu and Wang (2016). Capacitors were arranged like a cap type structure around plastic pipe creating fringing capacitance inside the pipe. When fluid flows through pipe, change in capacitance was observed which was directly projecting change in flow rate. Flow measurement in wind tunnel using a piezo electric sensor is reported by Kim et al. (2017). Wind flow measurement based on dynamic stress measured on wind tunnel using Pitot tube and trip strips. Sensor was designed to be sensitive for shear stress developed and was insensitive to static stress developed due to whirlwind lift up. An algorithm for improvement in accuracy for measurement of open channel flow rate is reported by Agu et al. (2017). Open channel flow system was simulated and fluid flow rate was estimated based on fluid depth. Measurement of flow rate by weighing method using two tanks is reported by Jaiswal et al. (2017). Second tank was used for increasing the time of water collection for large collection of water for reducing the diverter error. Redundancy was also a factor for using two tanks in case of failure in working of the tank. Flow rate was calculated based on the total amount of water collected and the time to collect the water. Flow rate measurement in thermal power plant large pipelines using radiotracer method is reported by (Biswal et al. 2018; Pecly and Fernandes, 2017). In this method, solution of radiotracer with known concentration is injected into large pipe with consistent rate for a pre expected time duration. At the down streams where radiotracer was mixed homogeneously, water samples were collected and based on the concentration of radiotracer, flow rate was measured. A fluid flow rate monitoring system using video-metering is reported by Lay-Ekuakille et al. (2014). This method can be used

where there is requirement of contactless measurement. Measurement of small fluid flow using electrochemical phenomenon is reported by Krejčí et al. (2017). This phenomenon requires electrochemical compound due to which this method is not used in practical applications. Santhosh and Roy (2016) reported a flow measurement technique using venturi, independent of variations in liquid type and pipe dimensions.

Researchers have also reported work in the area of indirect measurement of fluid flow few of which are reported here. A method for measurement of water consumption in a pipe was reported by Schantz et al. (2015). In this method an accelerometer for vibration measurement at the pipes was used based on which usage of water was detected. Vibration at the pipes was not only due to fluid flow it was also due to valve on and off function causing pressure change. Measurement of pressure induced by low velocity turbulent airflow is reported by Hobeck and Inman, (2015) using pressure probe. Pressure probes were constructed to measure high turbulent low velocity airflow with high sensitivity. Designed pressure probes were able to measure the air flow with a mean velocity of 0-12 m/s with a sensitivity of 0.064 mV/Pa. Estimation of flow rate at the input of a control valve in a flow system using an observer based soft sensor is reported by Navada et al. (2017). Observer is developed by using the measurement from an orifice placed to measure the flow rate at output of control valve. Development of a virtual sensor for measurement of flow rate in the pipes by using mathematical models is reported by Malan et al. (2017). A mathematical model between flow rate and head loss was found by measuring state of the valves and flow rate at the inlet. For estimating flow rate through heat body, Hardy cross type algorithm was used. Measurement of fluid flow rate by observing the vibrations of fluid pipe was reported by Dinardo et al. (2018). In this paper, authors have considered the root mean square value of the vibration signal and the variation of this parameter was related to fluid flow rate and was concluded to be proportional.

Some of the research in the area of vibration measurement is described in this section. Measurement of amplitude of micro vibration using optical interferometers was reported by Yasuda et al. (2015). In this method, two beams were used one as reference and the other reflected from vibrating body. Wave reflected from vibrating body generates an interference signal whose number of amplitude peaks was proportional to vibration amplitude. A Bragg's grating sensor for measurement of vibration is reported by Guozhen et al. (2016). Based on the frequency response of the grating acceleration sensor, vibration was measured. A non-contact method for measurement of vibration using binocular vision sensor and piezoelectric actuators was reported by Qiu et al. (2018). In this paper, it was reported that binocular sensor was giving good performance for measurement of low frequency vibration and structural displacement at multiple points. Tracking of rotating object vibration using image processing technique was reported by Kim et al. (2015). In this method, image sensor was used to track the position of the laser beam and landmark on rotating object to obtain the vibration characteristics. An algorithm to measure the vibrations of a pump unit is reported by Koshekov et al. (2016) for analyzing the working of the pump. In this method, vibration signals were collected by placing sensors at different locations of pump unit. Vibration speed root mean square value was considered for gathering the information regarding the pattern of vibration signals. A non-contact method of vibration measurement is reported by Lezhin et al. (2017) for high pressure engine. In this method, use of one dimension vibrometer for obtaining the details of engine surface vibration is reported and also compared with other two methods. Measurement of vibration displacement from a remote location using camera is reported by Son et al. (2015). This approach was suggested to use in the areas where measurement of vibrations are difficult to measure in location. Displacement was measured using edge detection technique and by taking second derivative of image. This method was reported to be better compared to other method as there was possibility of vibration measurements at multiple points. Mozuras (2017) reported a technique for measurement of high noisy vibration signals using a nonlinear converter. A monotonic nonlinear converter was used to get the vibration signals whose spectral components were found using Fourier transform. Measurement of structural vibration using optic electronic sensor is reported by Qiu and Lau, (2018). Measurement of propagation of surface vibrations in the ground using accelerometer is reported by Czech and Gosk, (2017). In this paper, accelerometers were mounted in the ground in four different ways and out of them ring mounting method was reported as the reliable method. A battery less sensor for measurement of vibrations induced in the rotating shafts of large ships was reported by Lee et al. (2018). Magnetostrictive principle was used to measure the vibrations induced due to high speed rotations. These sensors were used due to their healthy working nature under harsh environments. An ultrasonic stroboscope for measurement of underwater vibrations was reported by Luo et al. (2014). Authors have reported that this method was able to get the online information regarding the underwater vibrations. A cantilever underwater was used to test the sensor and it was compared with the traditional sensors. This sensor was not sensitive to the environmental changes and the major advantage was that it was a non-contact type of measurement.

From the survey it is evident that, flow is measured by a number of ways and head type or obstruction flow meters form a larger part of available measurement techniques. In the head type flow meters, measurement of flow is based on measurement of pressure difference created due to obstruction in the flow. But it is seen from the reported work that output of these sensor invariably vary with position at which sensor is placed. Characteristics of sensor often depend on liquid composition. So, in the proposed work a non-contact technique independent of liquid characteristics is presented.

2. EXPERIMENTAL SETUP

The experimental setup involves a simple flow process system consisting of reservoir, pneumatic actuators and flow meters.as depicted in Fig. 1. P and I diagram of the flow process system is shown in Fig. 2. Solid lines connecting the blocks represent the flow of fluid, dash lines represent the electric signal in terms of current and dotted line represents the air pressure. Process consists of a reservoir tank from which water is pumped. Water flows along the path, where a control valve, rotameter and orifice plate are placed before returning back to reservoir. Rotameter shows the rate of fluid flowing out of control valve. A differential pressure transmitter (DPT) is mounted to measure the pressure difference created by the orifice plate towards the flow. Pressure difference across the orifice is measured and is represented in terms of mV voltage by pressure transmitter. Air to open type equal percentage control valve with a 3/4-inch valve opening is placed between pump and rotameter to vary the flow rate. Pneumatic actuator consists of a current to pressure converter, a diaphragm, upper

DOI 10.2478/ama-2018-0045

and lower pressure chamber, spring and valve stem. User input current of 4-20mA range is applied to current to pressure converter, which converts it into 3-15psi range of pressure which is applied on the lower chamber of the control valve. Once the applied pressure on lower chamber is more than upper chamber, diaphragm moves up causing valve to open leading to increase in output flow rate. When the pressure in lower chamber is less than the upper chamber, then spring brings valve stem to close position causing no fluid to flow out of control valve. A bypass valve is provided near the pump to provide returning path for the flow when the control valve is fully shut. Flow rate at the output of control valve is mainly based on the position of valve and also fluid flow rate at the inlet of control valve.

Fig. 1. Flow process setup

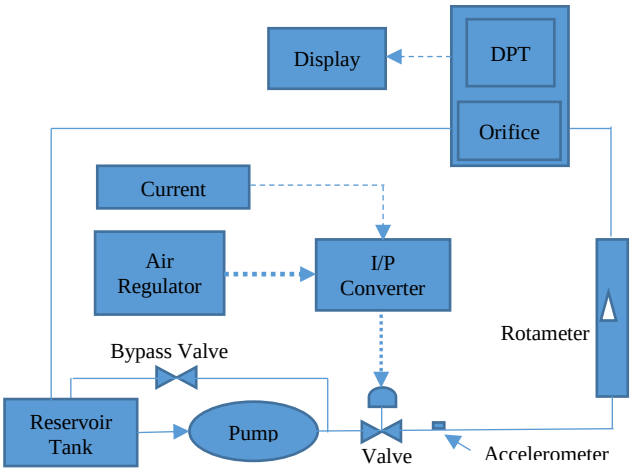

Fig. 2. P&I diagram of flow process system

3. STATEMENT OF OBJECTIVE

To understand the existing flow measurement technique using orifice flow meter, tests are carried out. Performance of the sensor is analyzed when the orifice hole diameter is varied and liquid is varied. The characteristics of the orifice flow meter is understood with the help of Bernoulli's equation given below).

$$\text{Flow rate: } Q = \frac{C.A_{th}.\sqrt{\frac{2.\Delta P}{\rho}}}{\sqrt{1-b^4}} \text{ lph} \quad (1)$$

where: C – is the coefficient, A_{th} – Cross section area at orifice hole, b – Ratio of orifice hole and pipe diameter, ρ – density of liquid, ΔP – difference in pressure

Pressure difference for varying flow under different beta 'b' is plot in Fig. 3. In the present study, a pipe diameter is considered to be 1 inch and orifice hole diameter is 0.5, 0.65 and 0.4 inches, flow is varied in the range of 0 to 1800 lph.

Similar tests are conducted by varying liquid density and the plot for the same is shown in Fig. 4.

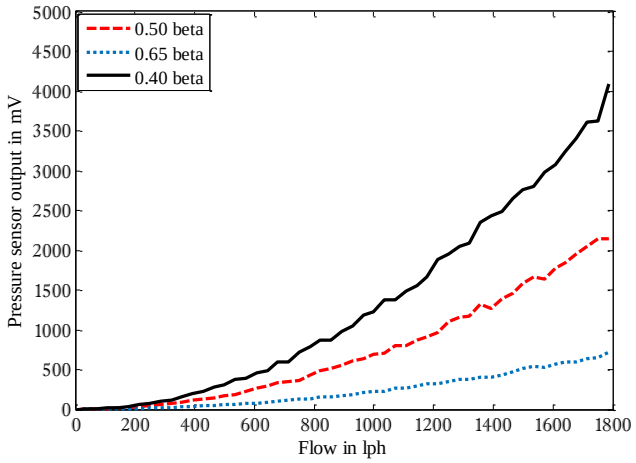

Fig. 3. Variation of flow transmitter characteristics with 'b'

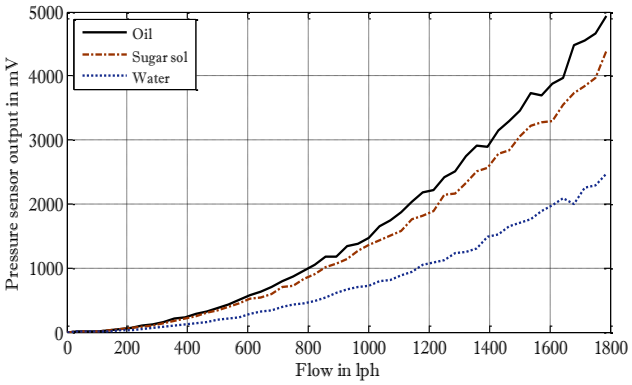

Fig. 4. Variation of flow transmitter characteristics with 'fluid density'

From the above graph and equations, it is clear that the present measurement technique involving head type flow meters like orifice, venturi, etc. or electromagnetic flow meters or rotameter would get effected by the placement of sensor. These meters would cause an impediment to the flow characteristics inside the pipe and if any physical faults occurs to these sensor, replacement of these is very tedious and need to be performed by authorized personnel only. So a technique is proposed in this paper which will measure the liquid flow without having contact with the flow and also would not pose any effect to flow characteristics.

4. METHODOLOGY

To achieve the objective discussed in the previous section it is essential to measure the flow rate using secondary sensor. Secondary sensor (accelerometer) data is used to estimate the flow rate in the proposed work. The vibration sensor is coupled on to

the pipe surface. In the proposed work, single axis accelerometer with a sensitivity of 9.8mV/g is mounted on pipe at the outlet of the pneumatic control valve, as shown in Fig. 5.

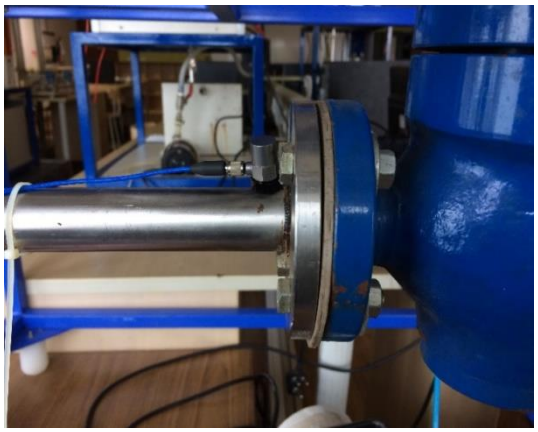

Fig. 5. Mounting of Accelerometer

Vibration data from the accelerometer is passed through an analog amplifier which is further acquired on to a computer using the data acquisition card. In the proposed work compact RIO of National Instruments is used to acquire the signal. Acquired data from the accelerometer is represented in Fig. 6 and Fig 7 for flow rates 1800 lph and 100 lph respectively.

To further analyze the signal, a band pass filter is designed. Filter is designed so as to reduce harmonics in the signal. Band pass filter is designed using the Sallen-Key architecture (Zin Ma Ma Myo et al. 2009) as given in below.

$$\text{Transfer function, } (s) = \frac{\frac{K_i}{P_i}.a.s}{\left[1+\frac{as}{P_i}+(as)^2\right]} \cdot \frac{\frac{K_i}{P_i}.a.s}{\left[1+\frac{1}{P_i}\left(\frac{s}{a}\right)+\left(\frac{s}{a}\right)^2\right]}. \quad (2)$$

A fourth order equation is considered, with 'K_i' as the gain at the mid frequency, 'f_i' of each filter. 'P_i' is the pole quality of each filter, 'B' is the filter coefficient. 'a' and '1/a' are the mid frequencies of individual filters.

$$\text{Gain at } f_i\text{: } K_i = \frac{B}{3-B}. \quad (3)$$

$$\text{Filter quality } P_i = \frac{1}{3-B}. \quad (4)$$

Output obtained after performing the filtering operation is shown in Fig 8 and Fig 9.

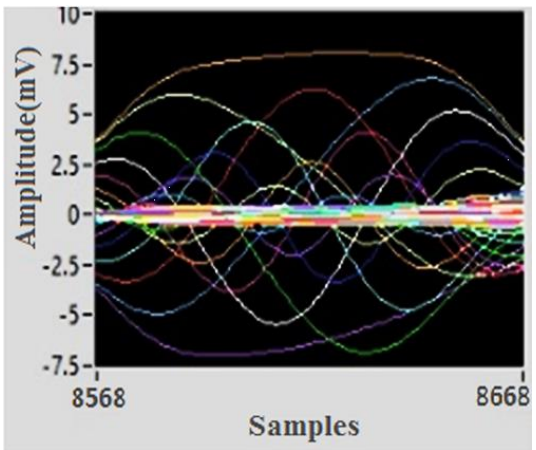

Fig. 6. Accelerometer signal for flow of 1800 lph

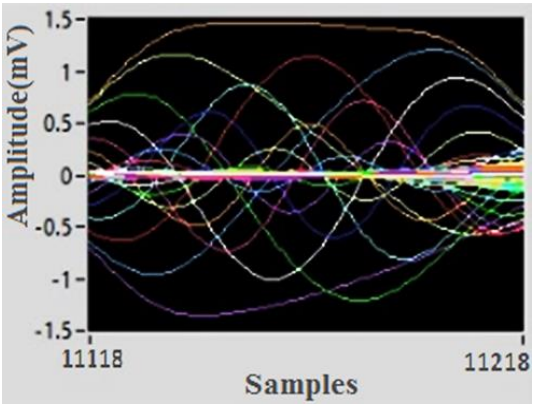

Fig. 7. Accelerometer signal for flow of 100 lph

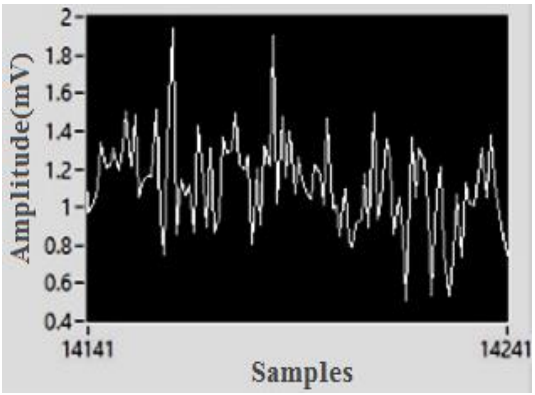

Fig. 8. Filtered output for flow of 1800 lph

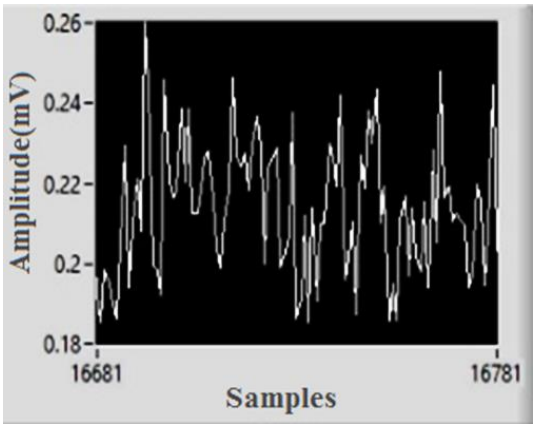

Fig. 9. Filtered output for flow of 100 lph

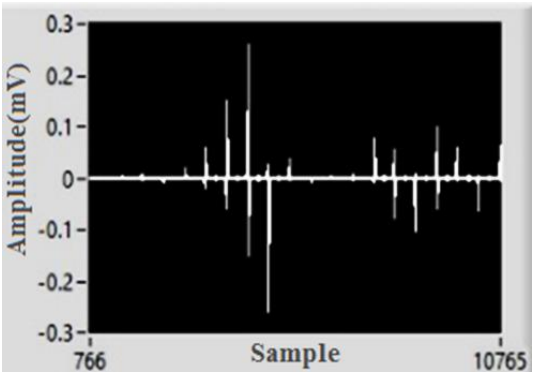

Fig. 10. Fourier transform output for flow of 1800 lph

DOI 10.2478/ama-2018-0045

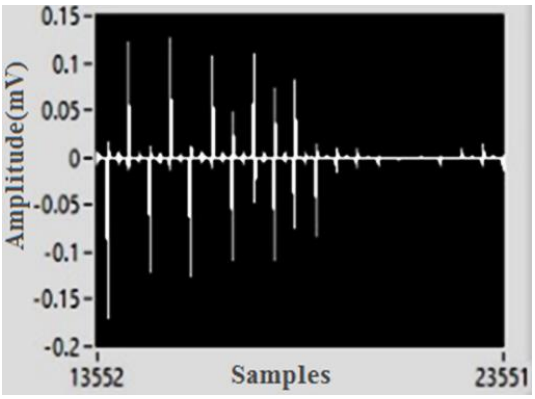

Fig. 11. Fourier transform output for flow of 100 lph

Fourier transform of the filtered signal is obtained so as to derive a magnitude function relating to flow rate. Fourier transform signal obtained for the flow of 100 lph and 1800 lph is shown in Fig. 10 and Fig. 11 respectively. The obtained Fourier transform signal is used to estimate the flow rate using neural network algorithm. For training the neural network is fed with input data and target data. Learning of neurons is achieved by varying the weighted function and activation function. Various algorithms had been presented in literature to varying the values of weighted function like Levenberg–Marquardt algorithm, genetic algorithm, artificial bee colony algorithms, ant colony optimization, etc. In the proposed work artificial bee colony algorithm is used to train the weights.

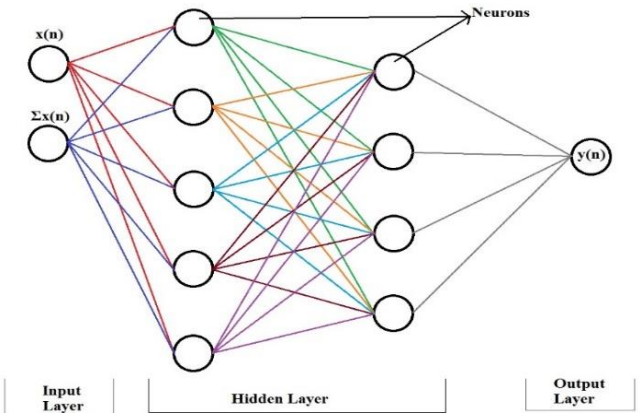

Fig. 12. Structure of neural network

Tab.1. Neural network parameters

Training data	2x86	60%
Validation data	2x29	20%
Test data	2x29	20%
Input layer	2 neurons	
Hidden layers	5 neurons	
	4 neurons	
Output layer	1 neuron	
Activation function	Tanh	
Learning rate	0.03	
Regularization rate	0.1	

Neurons are clustered in various networks like linear network, back propagation network, radial basis function, etc. In the proposed work back-propagation network is implemented. The multi-layer perceptron layer consisting of two hidden layers, one output and input layer is obtained. Output layer consists of a single neuron, hidden layers consists of five and four neurons. Input layer consists of two neurons which is subjected with Fourier transform signal and the normalized Fourier transform signal as shown in Fig 12. Neural network parameters obtained after training is shown in Tab. 1.

5. RESULTS AND ANALYSIS

Flow estimation technique designed using the accelerometer as sensor is tested and validated with standard available instrument. For testing flow rate is varied in the range of 0 to 1800 lph. The liquid under test is also varied to comprehend its performance of the designed system. Results obtained for the test conducted are shown in Tab. 2.

Tab. 2. Results obtained when tested with physical system

Actual flow (lph)	Estimated flow (lph)	Liquid type	% error
50	49.5	Water	1.00
150	151.2	Water	-0.80
400	401.5	Water	-0.38
510	513.6	Water	-0.71
650	648.2	Water	0.28
770	771.6	Water	-0.21
910	916.4	Water	-0.70
1000	997.2	Water	0.28
1180	1181.7	Water	-0.14
1320	1326.5	Water	-0.49
1510	1494	Water	1.06
1700	1721	Water	-1.24
350	351.8	Sugar solution	-0.51
480	484.8	Sugar solution	-1.00
610	607.4	Sugar solution	0.43
870	876.1	Sugar solution	-0.70
990	998.2	Sugar solution	-0.83
1250	1254.1	Sugar solution	-0.33
1470	1463.5	Sugar solution	0.44
1650	1662.3	Sugar solution	-0.75
1780	1776.4	Sugar solution	0.20

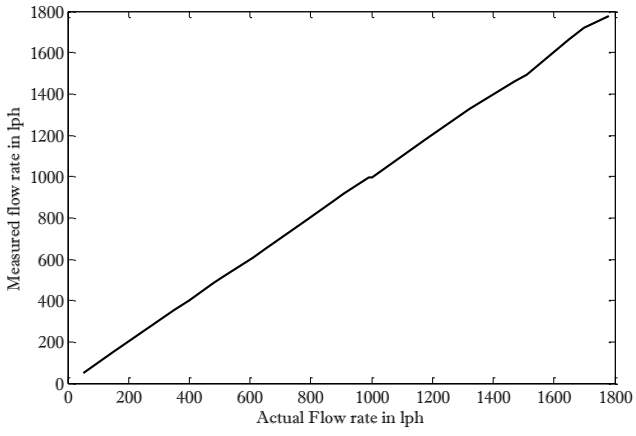

Fig. 13. Input output performance of proposed technique

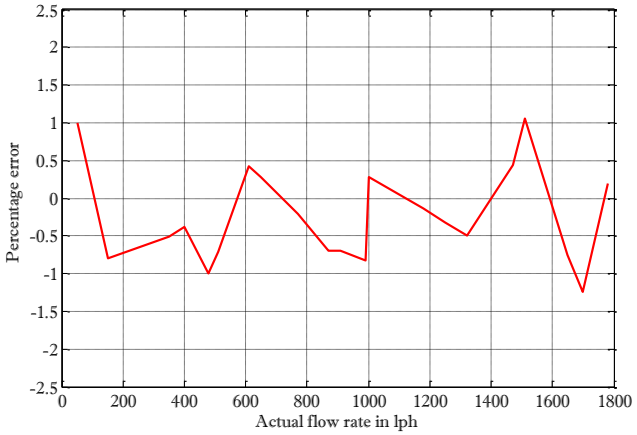

Fig. 14. Error performance of proposed technique

Performance of the presented work in estimating the flow rate of the liquid is represented in Tab. 2. It is observed that the flow rate is estimated accurately with maximum root mean square error of 1.24 %. Presented work is able to measure the flow rate indeterminate of fluid type within the maximum error of 21 lph without recalibrating the system for variation in fluid type. The plot of the error and input-output characteristics is depicted in Fig. 13 and Fig. 14. Characteristics shows linear behavior from the measurement system.

6. CONCLUSION

Flow measurement being one of the most widely used process in any industries, need to be highly precise and accurate. It is also expected that the system should be robust and needs less recalibration for variations in parameters. Available contact type measurement techniques often interrupt the behavior of flow and also needed to be recalibrated for changes in liquid type. Liquid flow estimation technique from the vibration analysis of the structure was designed with an objective of accurately measuring the flow rate even with changes in liquid type was fulfilled. The technique was designed by processing the signal from accelerometer in the stages of amplification, filtering, Fourier transform and neural network modeling. Performance of the trained system was analyzed using practical setup, and results shows successful implementation with a tolerable root mean square error of 0.67%.

From the characteristics displayed by the flow measurement system it is clear that, the instrument can be put in use for measurement of flow under harsh environment when the fluid parameter varies constantly.

REFERENCES

1. **Agu C.E., Hjulstad Å., Elseth G., Lie B**. (2017), Algorithm with improved accuracy for real-time measurement of flow rate in open channel systems, *Flow Measurement and Instrumentation,* 57, 20-27.
2. **Biswal J., Pant H.J., Goswami S., Samantray J.S., Sharma V.K., Sarma K.S.S.** (2018), Measurement of flow rates of water in large diameter pipelines using radiotracer dilution method, *Flow Measurement and Instrumentation*, 59, 194-200.
3. **Czech K.R., Gosk W.** (2017), Measurement of surface vibration accelerations propagated in the environment, *Procedia engineering*, 189, 45-50.
4. **Dinardo G., Fabbiano L., Vacca G., Lay-Ekuakille A.** (2018), Vibrational signal processing for characterization of fluid flows in pipes, *Measurement*, 113, 196-204.
5. **Guozhen Y., Yongqian L., Zhi Y.** (2016), A novel fiber Bragg grating acceleration sensor for measurement of vibration, *Optik-International Journal for Light and Electron Optics*, 127(20), 8874-8882.
6. **Hobeck J. D., Inman D.J.** (2015), Low-Cost Pressure Probe Sensor for Predicting Turbulence-Induced Vibration from Invasive Low-Velocity Turbulent Flow Measurements, *IEEE Sensors Journal*, 15(8), 4373-4379.
7. **Jaiswal S.K., Yadav S., Agarwal R.** (2017), Design and development of a novel water flow measurement system, *Measurement*, 105, 120-129.
8. **Kim D., Khalil H., Nam J., Park, K**. (2015), Image-based tracking system for rotating object vibration measurement using laser scanning vibrometer, *International Journal of Precision Engineering and Manufacturing*, 16(8), 1717-1721.
9. **Kim T., Saini A., Kim J., Gopalarathnam A., Zhu Y., Palmieri F.L., Jiang X.** (2017), Piezoelectric Floating Element Shear Stress Sensor for the Wind Tunnel Flow Measurement, *IEEE Trans. Ind. Electron*, 46, 1-1.
10. **Kirwan P.P., Creighton D., Costello C., O'Brien T.P., Moloney K.W.** (2016), Momentum Change Flow Meter With Pressure Compensation Using FBGs, *IEEE Sensors Journal*, 16(19), 7061-7064.
11. **Koshekov K.T., Klikushin Y.N., Kobenko V.Y., Sof'ina N.N., Savostin A. A., Kashevkin A.A.** (2016), Testing a pump unit by identification measurements of vibration signals, *Russian Journal of Nondestructive Testing*, 52(5), 280-286.
12. **Krejčí J., Ježová L., Kučerová R., Plička R., Broža Š., Krejčí D., Ventrubová I.** (2017), The measurement of small flow. *Sensors and Actuators A: Physical*, 266, 308-313.
13. **Lay-Ekuakille A., Vergallo P., Griffo G., Morello R.** (2014), Pipeline flow measurement using real-time imaging, *Measurement*, 47, 1008-1015.
14. **Lee J.K., Seung H.M., Park C.I., Lee J.K., Lim D.H., Kim, Y.Y.** (2018), Magnetostrictive patch sensor system for battery-less real-time measurement of torsional vibrations of rotating shafts, *Journal of Sound and Vibration,* 414, 245-258.
15. **Lezhin D.S., Falaleev S.V., Safin A.I., Ulanov A.M., Vergnano D.** (2017), Comparison of different methods of non-contact vibration measurement, *Procedia Engineering*, 176, 175-183.
16. **Liu Z., Wang W.** (2016), Flow measurement method based on a fringing field capacitor structure, *Electronics Letters*, 52(21), 1771-1772.
17. **Luo Z., Chu J., Shen L., Hu P., Zhu H., Hu L.** (2014), Measurement of underwater vibration by ultrasonic speckle stroboscopic technique. *Measurement*, 47, 938-945.
18. **Malan S., Greco C., Tisseur R., Bari F.** (2017), Parameters Estimation of Hydraulic Circuit Head Losses for Virtual Sensor Design, *IEEE Transactions on Control Systems Technology*, 25(4), 1345-1358.
19. **Marick S., Bera S.K., Bera S.C.** (2014), A modified technique of flow transducer using Bourdon tube as primary sensing element, *IEEE Sensors Journal*, 14(9), 3033-3039.
20. **Mozuras A**. (2017), Vibration measurement with nonlinear converter in the presence of noise, *Journal of Sound and Vibration*, 407, 309-331.
21. **Navada B.R., Santhosh K.V., Mazhar A., Singh A.K.,** (2017), July. Design of Kalman observer for estimation of in-flow, *International Conference on Intelligent Computing, Instrumentation and Control Technologies (ICICICT),* 1010-1014),
22. **Norgia M., Pesatori A., Donati S.** (2016), Compact laser-diode instrument for flow measurement, *IEEE Transactions on Instrumentation and Measurement,* 65(6), 1478-1483.
23. **Pecly J.O.G., Fernandes S.R.C.** (2017), Ancillary device for flow rate measurement using dye tracer technique, *Flow Measurement and Instrumentation*, 54, 274-282.

DOI 10.2478/ama-2018-0045

24. **Qiu Q., Lau D.** (2018), Measurement of structural vibration by using optic-electronic sensor, *Measurement*, 117, 435-443.
25. **Qiu Z.C., Wang X.F., Zhang X.M., Liu J.G.** (2018), A novel vibration measurement and active control method for a hinged flexible two-connected piezoelectric plate, *Mechanical Systems and Signal Processing*, 107, 357-395.
26. **Santhosh K.V., Roy B.K.** (2016), A Practically validated intelligent calibration circuit using optimized ANN for flow measurement using venture, *Jr. of The Institution of Engineers (India): Series B*, 97 (1), 31-39.
27. **Schantz C., Donnal J., Sennett B., Gillman M., Muller S., Leeb, S.** (2015), Water nonintrusive load monitoring, *IEEE Sensors Journal*, 15(4), 2177-2185.
28. **Sinha S., Banerjee D., Mandal N., Sarkar R., Bera S.C.** (2015), Design and implementation of real-time flow measurement system using Hall probe sensor and PC-based SCADA, *IEEE Sensors Journal*, 15(10), 5592-5600.
29. **Son K.S., Jeon H.S., Park J.H., Park J. W.** (2015), Vibration displacement measurement technology for cylindrical structures using camera images, *Nuclear Engineering and Technology*, 47(4), 488-499.
30. **Yasuda A., Hasegawa S., Pohtala J.V., Miyazaki T.** (2015), Amplitude measurement of micro-vibration with robust optical interferometer systems, *Optik-International Journal for Light and Electron Optics*, 126(23), 4577-4580.
31. **Zin M.M.M., Zaw M.A., Zaw M.N.** (2009), Design and Implementation of Active Band-Pass Filter for Low Frequency RFID (Radio Frequency Identification) System, *Proceedings of the International Multi Conference of Engineers and Computer Scientists, Hong Kong*.

sciendo

DOI 10.2478/ama-2018-0046

acta mechanica et automatica, vol.12 no.4 (2018)

AN INTERFACE CRACK WITH MIXED ELECTRO-MAGNETIC CONDITIONS AT IT FACES IN A PIEZOELECTRIC / PIEZOMAGNETIC BIMATERIAL UNDER ANTI-PLANE MECHANICAL AND IN-PLANE ELECTRIC LOADINGS

Oleg ONOPRIIENKO[*], Volodymyr LOBODA[*], Alla SHEVELEVA[**], Yuri LAPUSTA[***]

[*]Department of Theoretical and Applied Mechanics, Oles Honchar Dnipro National University, Gagarin Av., 72, Dnipro 49010, Ukraine
[**]Department of Computational Mathematics, Oles Honchar Dnipro National University, Gagarin Av., 72, Dnipro 49010, Ukraine
[***]Université Clermont Auvergne, SIGMA Clermont (ex- IFMA, French Institute of Advanced Mechanics),
Institut Pascal, BP 10448, F-63000 Clermont-Ferrand, France, CNRS, UMR 6602, IP, F-63178 Aubière, France

onopriienko.oleg@gmail.com, loboda@dnu.dp.ua, allasheveleva@i.ua, lapusta@sigma-clermont.fr

received 22 September 2017, revised 17 December 2018, accepted 20 December 2018

Abstract: An interface crack between two semi-infinite piezoelectric/piezomagnetic spaces under out-of-plane mechanical load and in-plane electrical and magnetic fields parallel to the crack faces is considered. Some part of the crack faces is assumed to be electrically conductive and having uniform distribution of magnetic potential whilst the remaining part of the crack faces is electrically and magnetically permeable. The mechanical, electrical, and magnetic factors are presented via functions which are analytic in the whole plane except the crack region. Due to these representations the combined Dirichlet-Riemann and Hilbert boundary value problems are formulated and solved in rather simple analytical form for any relation between conductive and permeable zone lengths. Resulting from this solution the analytical expressions for stress, electric and magnetic fields as well as for the crack faces displacement jump are presented. The singularities of the obtained solution at the crack tips and at the separation point of the mention zones are investigated and the formulas for the corresponding intensity factors are presented. The influence of external electric and magnetic fields upon the mechanic, electric and magnetic quantities at the crack region are illustrated in graph and table forms.

Keywords: Piezoelectromagnetic Material, Mode-III Interface Crack, Analytical Solution

1. INTRODUCTION

Piezoelectromagnetic materials are often used as functional parts of different engineering systems including sensors, transducers and actuators. However, existing micro-defects and particularly interface cracks can strongly reduce their strength. For this reason, interface cracks in piezoelectric and piezoelectomagnetic materials have been actively studying in the last several decades. A certain attention in this period was devoted to plane interface crack problem. Particularly, concerning piezoelectomagnetic materials this problem was developed in paper by Fan et al., (2009) and Feng et al., (2010). Different variants of electrical and magnetic conditions at the crack faces of an interface crack with a contact zone in a magnetoelectroelastic bimaterial under mechanical, electric and magnetic loads were considered by Herrmann et al., (2010), Feng et al., (2011, 2012), and Ma et al., (2012). Additional accounting of thermal flux for an interface crack in a magnetoelectroelastic bimaterial were performed in papers of Ma et al., (2011) and Feng et al., (2012). Modelling of the pre-fracture zone for an interface crack between two dissimilar magnetoelectroelastic materials was done by Ma et al., (2013). The electrically impermeable and magnetically permeable conditions at the crack faces were considered in this paper.

It is known (Parton and Kudryavtsev, 1988) that an in-plane electric or magnetic field induces the out-of-plane deformation for piezoelectric and piezoelectomagnetic material with certain directions of polarization. On this reason an investigation of such kind of deformation, particularly the mode III cracks, is more important for the mentioned materials than for electrically and magnetically passive ones. The mode III interface crack problem for dissimilar piezo-electromagneto-elastic bimaterial media with taking into account the electro-magnetic field inside the crack was investigated by Li and Kardomateas (2006) for impermeable and permeable crack models. A closed-form solution for anti-plane mechanical and in-plane electric and magnetic fields for a crack between two dissimilar magnetoelectroelastic materials was obtained in papers by Wang and Mai (2006, 2008) for the two extreme cases of an impermeable and a permeable crack. The anti-plane deformation of the multilayered piezomagnetic/piezoelectric composite with periodic interface cracks, subjected to in-plane magnetic or electric fields, was studied by Wan et al., (2012a) and Wan et al., (2012b) analyzed the mode III crack crossing the magnetoelectroelastic bimaterial interface under concentrated magnetoelectromechanical loads. The behaviour of two collinear and also parallel symmetry and non-symmetric interface cracks in magneto–electro–elastic materials under an anti-plane shear stress loading was by studied by Zhou et al., (2004, 2007a, 2009) with use of Schmidt method. The solutions of a limited-permeable crack or two collinear limited-permeable cracks in piezoelectric/ piezomagnetic materials subjected to a uniform tension loading were investigated in paper by Zhou et al., (2007b) using the generalized Almansi's theorem. Anti-plane problem for an impermeable or permeable interface crack between two dissimilar magnetoelectroelastic plates subjected to anti-plane mechanical and in-plane magneto-electrical loads was investigated by Su and

Feng (2008). Multiferroic interface fracture of piezomagnetic/ piezoelectric composite under magnetic and electric loadings was considered by Li and Lee (2010). Shi et al., (2013) investigated arc-shaped interface cracks between a functionally graded magneto-electro-elastic layer and an orthotropic elastic substrate under anti-plane shear load. Single and periodic mode-III cracks moving along the interface of piezoelectric-piezomagnetic bimaterial were considered by Chen et al., (2012) and Yue and Wan (2014), respectively. Also the case of a moving interface crack between magnetoelectroelastic and functionally graded elastic layers was studied by Hu and Chen (2014). An exact analytic solution to the anti-plane problem for a non-homogeneous bimaterial medium containing closed interfacial cracks, which faces can move relatively to each other with dry friction under the action of arbitrary single loading and also cyclic loading was considered by Sulym et al., (2015a, 2015b). A more detailed review of anti-plane crack problem investigation in piezoelectric/piezomagnetic bimaterials is presented in Govorukha et al., (2016).

Temporary actuators and other electronic devices are often constructed with use of thin film electrodes sandwiched between piezoelectric layers. Such electrodes are usually prepared of a metal powder, conducting polymers etc. and do not change the mechanical properties of matrixes (Ru, 2000). Delamination of the mentioned electrodes leads to the appearance of conducting interface cracks. For a plane case a conductive interface crack in a piezoelectric bimaterial was considered by Beom and Atluri (2002) and Loboda et al., (2014) for "open" and contact zone crack models, respectively. For an out-of-plane conductive interface crack the results of the papers Wang and Zhong (2002) and Wang et al., (2003) specifying the oscillating singularity at the crack tips are valid. However in many cases only some part of the crack faces can be conductive because of interface electrode delamination while on remaining part some other kind of electrical conditions can take place. Accounting of such mixed electrical conditions at the crack faces leads to more complicated problem than for uniform ones. The crack with mixed (conductive-permeable) conditions at the crack faces was considered for a piezoelectric bimaterial by Lapusta et al., (2017). However, for a piezoelectric/ piezomagnetic bimaterials this important situation has not been studied before and it comprises the main subject of the present paper. In spite of this case is more complicated than the piezoelectric one, an exact solution of the problem was found.

2. BASIC FORMULAS FOR PEMM (PIEZO-ELECTRO-MAGNETIC MATERIAL) FOR ANTI-PLANE CASE

The constitutive relations for the piezo-electro-magnetic material are (Sih and Song, 2003):

$$\sigma_{ij} = c_{ijks}\varepsilon_{ks} - e_{sij}E_s - h_{sij}H_s,$$

$$D_i = e_{iks}\varepsilon_{ks} + \alpha_{is}E_s + d_{is}H_s,$$

$$B_i = h_{iks}\varepsilon_{ks} + d_{is}E_s + \gamma_{is}H_s,$$

where σ_{ij}, ε_{ij} – components of stress and strain tensors, D_i, B_i – components of the electric and magnetic inductions, E_i, H_i – intensities of the electric and magnetic fields, c_{ijks} – elastic, e_{iks} – piezoelectric, h_{iks} – piezomagnetic, d_{is} – electromagnetic constants, α_{is}, γ_{is} – electric and magnetic permeabilities.

The equilibrium equations in the absence of body forces and free charges are:

$$\sigma_{ij,j} = 0, D_{i,i} = 0, B_{i,i} = 0.$$

The expressions for the deformation, electric and magnetic fields have the form:

$$\varepsilon_{ij} = \frac{1}{2}\left(u_{i,j} + u_{j,i}\right), E_i = -\phi_{,i}, H_i = -\psi_{,i},$$

where u_i – the components of the displacement vector, ϕ, ψ – the electric and magnetic potentials, comma means differentiation on the respective coordinate.

In an anti-plane case we have:

$$u_1 = u_2 = 0, u_3 = u_3(x_1, x_2),$$

$$\phi = \phi(x_1, x_2), \psi = \psi(x_1, x_2).$$

Then, the constitutive relations take the form:

$$\begin{pmatrix}\sigma_{3i}\\ D_i\\ B_i\end{pmatrix} = \mathbf{R}\begin{pmatrix}u_{3,i}\\ -\phi_{,i}\\ -\psi_{,i}\end{pmatrix}, \mathbf{R} = \begin{pmatrix}c_{44} & e_{15} & h_{15}\\ e_{15} & -\alpha_{11} & -d_{11}\\ h_{15} & -d_{11} & -\gamma_{11}\end{pmatrix},$$

where $i = 1,2$.

Introducing the vectors:

$$\mathbf{u} = [u_3, \phi, \psi]^T, \mathbf{t} = [\sigma_{32}, D_2, B_2]^T, \quad (1)$$

one can write

$$\mathbf{t} = \mathbf{R}\mathbf{u}_{,2}. \quad (2)$$

As the functions u_3, ϕ and ψ are harmonic, then taking into account (2), the following presentations are valid:

$$\mathbf{u} = \Phi(z) + \overline{\Phi}(\bar{z}),$$

$$\mathbf{t} = \mathbf{B}\Phi'(z) + \overline{\mathbf{B}}\overline{\Phi}'(\bar{z}), \quad (3)$$

where: $\Phi(z) = [\Phi_1(z), \Phi_2(z), \Phi_3(z)]^{\mathrm{T}}$ – an arbitrary analytical vector-function of the complex variable $z = x_1 + ix_2$, $\mathbf{B} = i\mathbf{R}$.

3. FORMULATION OF THE PROBLEM AND BASIC FORMULAS FOR A BIMATERIAL COMPOUND

Assume that the crack is located in the interval $[c, b]$ of the material separation line (Fig. 1). Suppose also that the section $[c, a]$ of the crack faces is covered with electrodes, which, moreover, maintain a constant distribution of the magnetic field. It means that the conditions on this section can be written in the form:

$$\sigma_{32}^{(1)} = \sigma_{32}^{(2)} = 0, E_1^{(1)} = E_1^{(2)} = 0,$$

$$H_1^{(1)} = H_1^{(2)} = 0 \text{ for } c < x_1 < a. \quad (4)$$

The remaining part of the crack is assumed to be free from electrodes. Therefore, because of the absence of the crack opening in x_2 direction this part of crack faces should be considered as electrically and magneto permeable. Thus, one gets the following conditions:

$$\sigma_{32}^{(1)} = \sigma_{32}^{(2)} = 0, \langle D_2 \rangle = 0, \langle B_2 \rangle = 0,$$

$$\langle E_1 \rangle = 0, \langle H_1 \rangle = 0 \text{ for } a < x_1 < b, \quad (5)$$

where $\langle \bullet \rangle$ means the jump of the function via material interface.

sciendo
DOI 10.2478/ama-2018-0046

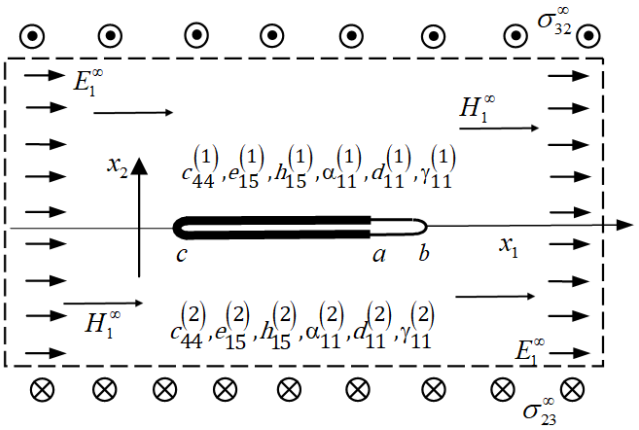

Fig. 1. A crack between two piezoelectromagnetic materials

The crack described above may arise due to a soft multi-layered electrode exfoliation, made of ferro-magnetic material, situated at the interval $[c, a]$, with the additional exfoliation of the interval $[a, b]$ of the non-electroded interface. Electric and magnetic conditions used in (4), (5) can be considered as a certain approximation of real conditions taking place at the interface crack faces in piezoelectromagnetic bimaterials. However in many cases these conditions model electric and magnetic state at these faces with sufficient accuracy Wang and Mai (2008). It's also assumed, that the vector $P^{\infty} = [\sigma_{32}^{\infty}, E_1^{\infty}, H_1^{\infty}]^T$ is given at infinity.

Introducing the vectors:

$$\mathbf{v}' = [u_3', D_2, B_2]^T, \mathbf{P} = [\sigma_{32}, \phi', \psi']^T \tag{6}$$

(the derivatives in (6) are implicit on x_1), on the basis of (3) we have:

$$\mathbf{v}' = \mathbf{M}\Phi'(z) + \overline{\mathbf{M}}\overline{\Phi}'(\bar{z}), \tag{7}$$

$$\mathbf{P} = \mathbf{N}\Phi'(z) + \overline{\mathbf{N}}\overline{\Phi}'(\bar{z}), \tag{8}$$

where the matrixes $\mathbf{M}$ and $\mathbf{N}$ have the structure:

$$\mathbf{M} = \begin{pmatrix} 1 & 0 & 0 \\ B_{21} & B_{22} & B_{23} \\ B_{31} & B_{32} & B_{33} \end{pmatrix}, \mathbf{N} = \begin{pmatrix} B_{11} & B_{12} & B_{13} \\ 0 & 1 & 0 \\ 0 & 0 & 1 \end{pmatrix}.$$

For a bimaterial compound the relations (7), (8) can be written in the form:

$$\mathbf{v}'^{(k)} = \mathbf{M}^{(k)}\Phi'^{(k)}(z) + \overline{\mathbf{M}}^{(k)}\overline{\Phi}'^{(k)}(\bar{z}), \tag{9}$$

$$\mathbf{P}^{(k)} = \mathbf{N}^{(k)}\Phi'^{(k)}(z) + \overline{\mathbf{N}}^{(k)}\overline{\Phi}'^{(k)}(\bar{z}), \tag{10}$$

where $k = 1$ for the area 1 and $k = 2$ for the area 2; $\mathbf{M}^{(k)}$ and $\mathbf{N}^{(k)}$ are the matrixes $\mathbf{M}$ and $\mathbf{N}$ for the areas 1 and 2, respectively; $\Phi^{(k)}(z)$ are arbitrary vector-functions, analytic in the areas 1 and 2, respectively.

Next we require that the equality $P^{(1)} = P^{(2)}$ holds true on the entire axis x_1. Then it follows from (10):

$$\mathbf{N}^{(1)}\Phi'^{(1)}(x_1 + i0) + \overline{\mathbf{N}}^{(1)}\overline{\Phi'^{(1)}}(x_1 - i0) =$$

$$= \mathbf{N}^{(2)}\Phi'^{(2)}(x_1 - i0) + \overline{\mathbf{N}}^{(2)}\overline{\Phi'^{(2)}}(x_1 + i0). \tag{11}$$

Here we have used the designation $F(x_1 \pm i0) = F^{\pm}(x_1)$, which means the limit value of a function $F(z)$ *at* $x_2 \to 0$ from above or below, respectively.

The equation (11) can be written as:

$$\mathbf{B}^{(1)}\Phi'^{(1)}(x_1 + i0) - \overline{\mathbf{B}}^{(2)}\overline{\Phi}'^{(2)}(x_1 + i0) =$$

$$= \mathbf{B}^{(2)}\Phi'^{(2)}(x_1 - i0) - \overline{\mathbf{B}}^{(1)}\overline{\Phi}'^{(1)}(x_1 - i0).$$

The left and right sides of the last equation can be considered as the boundary values of the functions:

$$\mathbf{N}^{(1)}\Phi'^{(1)}(z) - \overline{\mathbf{N}}^{(2)}\overline{\Phi}'^{(2)}(z)$$

and:

$$\mathbf{N}^{(2)}\Phi'^{(2)}(z) - \overline{\mathbf{N}}^{(1)}\overline{\Phi}'^{(1)}(z), \tag{12}$$

which are analytic in the upper and lower planes, respectively. But it means that there is a function $\Pi(z)$, which is equal to the mentioned functions in each half-plane and is analytic in the entire plane.

Assuming $\Pi(z)|_{z\to\infty} \to 0$, on the basis of the Liouville theorem we find that each of the functions (12) is equal to 0 for each z from the corresponding half-plane. Hence, we obtain:

$$\overline{\Phi}'^{(2)}(z) = \left(\overline{\mathbf{N}}^{(2)}\right)^{-1}\mathbf{N}^{(1)}\Phi'^{(1)}(z) \text{ for } x_2 > 0, \tag{13}$$

$$\overline{\Phi}'^{(1)}(z) = \left(\overline{\mathbf{N}}^{(1)}\right)^{-1}\mathbf{N}^{(2)}\Phi'^{(2)}(z) \text{ for } x_2 < 0. \tag{14}$$

Further we find the jump of the following vector function:

$$\langle \mathbf{v}'(x_1) \rangle = \mathbf{v}'^{(1)}(x_1 + i0) - \mathbf{v}'^{(1)}(x_1 - i0), \tag{15}$$

when passing through the interface. Finding from the formula (9):

$$\mathbf{v}'^{(k)}(x_1 \pm i0) = \mathbf{M}^{(k)}\Phi'^{(k)}(x_1 \pm i0) + \overline{\mathbf{M}}^{(k)}\overline{\Phi}'^{(k)}(x_1 \mp i0)$$

and substituting in (15), one gets:

$$\langle \mathbf{v}'(x_1) \rangle = \mathbf{M}^{(1)}\Phi'^{(1)}(x_1 + i0) + \overline{\mathbf{M}}^{(1)}\overline{\Phi}'^{(1)}(x_1 - i0) -$$

$$-\mathbf{M}^{(2)}\Phi'^{(2)}(x_1 - i0) - \overline{\mathbf{M}}^{(2)}\overline{\Phi}'^{(2)}(x_1 + i0).$$

Determining further:

$$\Phi'^{(2)}(x_1 - i0) = \left(\mathbf{N}^{(2)}\right)^{-1}\overline{\mathbf{N}}^{(1)}\overline{\Phi}'^{(1)}(x_1 - i0)$$

from (14) and substituting this expression together with (13), at $x_2 \to +0$, into the latest formula, leads to:

$$\langle \mathbf{v}'(x_1) \rangle = \mathbf{D}\Phi'^{(1)}(x_1 + i0) + \overline{\mathbf{D}}\overline{\Phi}'^{(1)}(x_1 - i0), \tag{16}$$

where: $\mathbf{D} = \mathbf{M}^{(1)} - \overline{\mathbf{M}}^{(2)}\left(\overline{\mathbf{N}}^{(2)}\right)^{-1}\mathbf{N}^{(1)}$.

Introducing a new vector-function:

$$\mathbf{W}(z) = \begin{cases} \mathbf{D}\Phi'^{(1)}(z), & x_2 > 0, \\ -\overline{\mathbf{D}}\overline{\Phi}'^{(1)}(z), & x_2 < 0 \end{cases} \tag{17}$$

the expression (16) can be written as:

$$\langle \mathbf{v}'(x_1) \rangle = \mathbf{W}^{+}(x_1) - \mathbf{W}^{-}(x_1). \tag{18}$$

From the relations (10) we have:

$$\mathbf{P}^{(1)}(x_1, 0) =$$
$$\mathbf{N}^{(1)}\Phi'^{(1)}(x_1 + i0) + \overline{\mathbf{N}}^{(1)}\overline{\Phi}'^{(1)}(x_1 - i0). \tag{19}$$

Taking into account that on the base of (17):

$$\Phi'^{(1)}(x_1 + i0) = \mathbf{D}^{-1}\mathbf{W}(x_1 + i0),$$
$$\overline{\Phi}'^{(1)}(x_1 - i0) = -(\overline{\mathbf{D}}^{-1})^{-1}\mathbf{W}(x_1 - i0),$$

and substituting these relations into (19), leads to:

$$\mathbf{P}^{(1)}(x_1, 0) = \mathbf{S}\mathbf{W}^{+}(x_1) - \bar{\mathbf{S}}\mathbf{W}^{-}(x_1), \tag{20}$$

where: $\mathbf{S} = \mathbf{N}^{(1)}\mathbf{D}^{-1}$. From the last relations it follows that:

$$\mathbf{S} = \left[\mathbf{M}^{(1)}\left(\mathbf{N}^{(1)}\right)^{-1} - \overline{\mathbf{M}}^{(2)}\left(\overline{\mathbf{N}}^{(2)}\right)^{-1}\right]^{-1}.$$

The representations (18) and (20) can be used for solving of anti-plane problems for bimaterials with cracks at the interface. However, we transform further these representations to the form, which is more convenient for the solution of the formulated problem.

Consider the matrix $\mathbf{L} = [L_1, L_2, L_3]$ and the composition:

$$\mathbf{L}\mathbf{P}^{(1)}(x_1, 0) = \mathbf{L}\mathbf{S}\mathbf{W}^{+}(x_1) - \mathbf{L}\bar{\mathbf{S}}\mathbf{W}^{-}(x_1). \quad (21)$$

Denoting $\mathbf{Y} = [Y_1, Y_2, Y_3] = \mathbf{L}\mathbf{S}$, we introduce the function:

$$F(z) = \mathbf{Y}\mathbf{W}(z). \quad (22)$$

Let's assume that $\mathbf{L}\bar{\mathbf{S}} = -\gamma\mathbf{L}\mathbf{S}$ and transpose last equation for convenience. It gives:

$$(\gamma\mathbf{S}^T + \bar{\mathbf{S}}^T)\mathbf{L}^T = 0. \quad (23)$$

This is an eigenvalue problem for finding an eigenvalue γ and an eigenvector $\mathbf{L}^T$. The eigenvalues are the roots of the equation:

$$\det(\gamma\mathbf{S}^T + \bar{\mathbf{S}}^T) = 0, \quad (24)$$

which we denote as γ_1, γ_2, γ_3. Eigenvectors $\mathrm{L_j^T} = \left[L_{\mathrm{j}1}, L_{\mathrm{j}2}, L_{\mathrm{j}3}\right]^{\mathrm{T}}$ $(j = 1,2,3)$, which correspond to the eigenvalues γ_{j} are found from the system (23).

Denoting:

$$\mathbf{Y}_j = \mathbf{L}_j\mathbf{S}, \quad (25)$$

we obtain from (21):

$$\mathbf{L}_j\mathbf{P}^{(1)}(x_1, 0) = \mathbf{Y}_j\mathbf{W}^{+}(x_1) + \gamma_j\mathbf{Y}_j\mathbf{W}^{-}(x_1),$$

or, taking into account (22), one gets:

$$\mathbf{L}_j\mathbf{P}^{(1)}(x_1, 0) = F_j{}^{+}(x_1) + \gamma_j F_j{}^{-}(x_1), \quad (26)$$

where:

$$F_j(z) = \mathbf{Y}_j\mathbf{W}(z). \quad (27)$$

Because $\mathbf{F}^{+}(x_1) = \mathbf{F}^{-}(x_1) = \mathbf{F}(x_1)$ for $x_1 \notin (c, b)$, we obtain from (26) the following condition at infinity:

$$F_j(z)\big|_{z\to\infty} = \frac{1}{1+\gamma_j}\left(L_{j1}\sigma_{32}^{\infty} + L_{j2}E_1^{\infty} + L_{j3}H_1^{\infty}\right). \quad (28)$$

It should be noted that for the considered class of piezoelectric/piezomagnetic materials the matrix $\mathbf{S}$ has the following structure:

$$\mathbf{S} = \begin{pmatrix} i\,s_{11} & s_{12} & s_{13} \\ s_{21} & i\,s_{22} & i\,s_{23} \\ s_{31} & i\,s_{32} & i\,s_{33} \end{pmatrix}, \quad (29)$$

where all s_{kl} $(k, l = 1,2,3)$ are real. In this case the eigenvalues of the system (23) are:

$$\gamma_1 = 1, \gamma_2 = \frac{\delta+1}{\delta-1}, \gamma_3 = \frac{\delta-1}{\delta+1}, \quad (30)$$

where $t_1 = s_{21}s_{32}s_{13} + s_{12}s_{23}s_{31} - s_{31}s_{22}s_{13} - s_{12}s_{21}s_{33}$, $t_2 = s_{11}s_{22}s_{33} - s_{23}s_{32}s_{11}$, $\delta = \sqrt{t_2/t_1}$.

The eigenvectors, corresponding to these eigenvalues are found from the system (23) and can be presented in the form:

$$\mathbf{L}_1 = [0,1,\omega_{13}], \mathbf{L}_2 = [1, i\omega_{22}, i\omega_{23}],$$

$$\mathbf{L}_3 = [1, i\omega_{32}, i\omega_{33}], \quad (31)$$

where: $\omega_{13} = -\frac{s_{21}}{s_{31}}$, $\omega_{22} = \frac{\omega}{D_0}(s_{12}s_{23} - s_{13}s_{32})$, $\omega_{23} = \frac{\omega}{D_0}(s_{22}s_{13} - s_{23}s_{12})$, $\omega_{32} = -\omega_{22}$, $\omega_{33} = -\omega_{23}, \omega = \frac{\gamma_2+1}{\gamma_2-1}$, $D_0 = s_{22}s_{33} - s_{23}s_{32}$.

Taking into account the presentation (31) the relation (26) for $j = 1,2$ can be written in the form:

$$E_1^{(1)}(x_1, 0) + \omega_{13}H_1^{(1)}(x_1, 0) = F_1^{+}(x_1) + F_1^{-}(x_1), \quad (32)$$

$$\sigma_{32}^{(1)}(x_1, 0) + i\omega_{22}E_1^{(1)}(x_1, 0) + i\omega_{23}H_1^{(1)}(x_1, 0) =$$

$$= F_2^{+}(x_1) + \gamma_2 F_2^{-}(x_1). \quad (33)$$

From the equations (6), (18) and (27) one gets:

$$Y_{j1}\langle u_3{}'(x_1, 0)\rangle + Y_{j2}\langle D_2(x_1, 0)\rangle + Y_{j3}\langle B_2(x_1, 0)\rangle =$$

$$= F_j^{+}(x_1) - F_j^{-}(x_1). \quad (34)$$

It follows from analysis of (29) and (31) that for the considered class of materials $Y_{11} = 0$, Y_{jk} are real and Y_{1k}, Y_{j1} are pure imaginary. Therefore, introducing the following designations $\eta_{1k} = -iY_{1k}, \eta_{j1} = -iY_{j1}, \eta_{jk} = Y_{jk}$ $(j, k = 2,3)$ the Eq. (34) for $j = 1,2$ can be written in the form:

$$i\eta_{12}\langle D_2(x_1, 0)\rangle + i\eta_{13}\langle B_2(x_1, 0)\rangle = F_1^{+}(x_1) - F_1^{-}(x_1), \quad (35)$$

$$i\eta_{21}\langle u_3{}'(x_1, 0)\rangle + \eta_{22}\langle D_2(x_1, 0)\rangle + \eta_{23}\langle B_2(x_1, 0)\rangle =$$

$$= F_2^{+}(x_1) - F_2^{-}(x_1). \quad (36)$$

It's important that all ω_{ij} and η_{ij} in Eqs. (32), (33) and (35), (36) are real.

4. FORMULATION AND SOLUTION OF THE PROBLEMS OF LINER RELATIONSHIP

Satisfying the conditions (14) with use of (33), one gets:

$$F_2^{+}(x_1) + \gamma_2 F_2^{-}(x_1) = 0 \text{ for } c < x_1 < a. \quad (37)$$

Satisfying further the conditions (15) by using (33) and (36), we obtain:

$$\mathrm{Re}[F_2^{+}(x_1) + \gamma_2 F_2^{-}(x_1)] = 0,$$

$$\mathrm{Re}[F_2^{+}(x_1) - F_2^{-}(x_1)] = 0 \text{ for } a < x_1 < b.$$

The last equation can be written in the form:

$$\mathrm{Re}F_2^{\pm}(x_1) = 0 \quad \text{for } a < x_1 < b. \quad (38)$$

The equations (37), (38) form the combined Dirichlet-Riemann boundary value problem. To solve this problem we introduce the following substitution:

$$F_2\ (z) = i\Phi_2(z) \quad (39)$$

and Eqs. (37), (38) attain the form:

$$\Phi_2^{+}(x_1) + \gamma_2\Phi_2^{-}(x_1) = 0, c < x_1 < a,$$

$$\mathrm{Im}\Phi_2^{+}(x_1) = 0, a < x_1 < b. \quad (40)$$

On the base of (28) and (39) the conditions at infinity can be presented in the form:

$$\Phi_2(z)|_{z\to\infty} = \tilde{E}_2 + \tilde{H}_2 - i\tilde{\sigma}_{32}^{(1)}, \quad (41)$$

where $\tilde{E}_2 = \frac{\omega_{22}}{1+\gamma_2}E_1^{\infty}$, $\tilde{H}_2 = \frac{\omega_{23}}{1+\gamma_2}H_1^{\infty}$, $\tilde{\sigma}_{32}^{(2)} = \frac{\sigma_{32}^{\infty}}{1+\gamma_2}$.

Considering the results of Nahmein and Nuller (1986) and Kozinov et al., (2013) the solution of the problem (40) under the conditions at infinity (41) has the following form:

$$\Phi_2(z) = P(z)X_1(z) + Q(z)X_2(z), \quad (42)$$

where: $P(z) = C_1 z + C_2$, $Q(z) = D_1 z + D_2$, $l = b - c$,

$X_1(z) = \frac{ie^{i\chi(z)}}{\sqrt{(z-c)(z-b)}}$, $X_2(z) = \frac{e^{i\chi(z)}}{\sqrt{(z-c)(z-a)}}$,

$\chi(z) = 2\varepsilon_2 \ln\frac{\sqrt{(b-a)(z-c)}}{\sqrt{l(z-a)}+\sqrt{(a-c)(z-b)}}$, $\varepsilon_2 = \frac{1}{2\pi}\ln\gamma_2$,

$C_1 = -\tilde{\sigma}_{32}\cos\beta - (\tilde{E}_2 + \tilde{H}_2)\sin\beta$, $C_2 = -\frac{c+b}{2}C_1 - \beta_1 D_1$,

$D_1 = (\tilde{E}_2 + \tilde{H}_2)\cos\beta - \tilde{\sigma}_{32}\sin\beta$, $D_2 = \beta_1 C_1 - \frac{c+a}{2}D_1$.

In the above relations:

$$\beta = \varepsilon_2 \ln\frac{1-\sqrt{1-\lambda}}{1+\sqrt{1-\lambda}}, \beta_1 = \varepsilon_2\sqrt{(a-c)(b-c)}, \lambda = (b-a)/l.$$

Using presentation (33) one can write:

$$\sigma_{32}^{(1)}(x_1,0) + i\omega_{22}E_1^{(1)}(x_1,0) + i\omega_{23}H_1^{(1)}(x_1,0) = \\ = i[\Phi_2^+(x_1) + \gamma_2\Phi_2^-(x_1)]. \quad (43)$$

The stress $\sigma_{32}^{(1)}(x_1,0)$ can be found from (43), however only the combination of $E_1^{(1)}(x_1,0)$ and $H_1^{(1)}(x_1,0)$ can be obtained as imaginary part of this expression. To find the mentioned values separately consider the expressions (32) and (35).

Satisfying with use of (32) to second and third boundary conditions of (4) one arrives at the following equation:

$$F_1^+(x_1) + F_1^-(x_1) = 0 \text{ for } c < x_1 < a. \quad (44)$$

Due to second and third boundary conditions of (5) the function $F_1(z)$ is analytic in the whole plane except the segment $[c,a]$. Taking this fact into account, the solution of Eq. (44) can be presented in the form Muskhelishvili (1977):

$$F_1(z) = \frac{c_0 + c_1 z}{\sqrt{(z-c)(z-a)}},$$

where c_0 and c_1 are arbitrary constants. Determining these constants from the condition at infinity $F_1(z)|_{z\to\infty} = 0.5(E_1^{\infty} + \omega_{13}H_1^{\infty})$, which follows from (32), and from the requirement of single valuedness of displacements, one gets:

$$F_1(z) = (E_1^{\infty} + \omega_{13}H_1^{\infty})\frac{z-(a+c)/2}{2\sqrt{(z-c)(z-a)}}. \quad (45)$$

Using the solutions (42), (45) and the presentations (35), (36), we get the following system for u_3, D_2, B_2 determination at $x_1 \in (c,a)$:

$$i\eta_{21}\langle u'_3(x_1,0)\rangle + \eta_{22}\langle D_2(x_1,0)\rangle + \eta_{23}\langle B_2(x_1,0)\rangle = \\ = i\sqrt{\alpha}\left[\frac{P(x_1)}{\sqrt{b-x_1}} - i\frac{Q(x_1)}{\sqrt{a-x_1}}\right]\frac{\exp[i\chi^*(x_1)]}{\sqrt{x_1-c}}, \quad (46)$$

$$i\eta_{12}\langle D_2(x_1,0)\rangle + i\eta_{13}\langle B_2(x_1,0)\rangle = \\ = (E_1^{\infty} + m_{13}H_1^{\infty})\cdot\frac{x_1-(a+c)/2}{\sqrt{(x_1-c)(a-x_1)}}, \quad (47)$$

where: $\alpha = \frac{(1+\gamma_2)^2}{4\gamma_2}$,

$$\chi^*(x_1) = 2\varepsilon_2\ln\left[\frac{\sqrt{(b-a)(x_1-c)}}{\sqrt{(b-c)(a-x_1)}+\sqrt{(a-c)(b-x_1)}}\right].$$

From Eq. (46) one gets the following expression for the displacement jump at the segment (c,a):

$$\langle u'_3(x_1,0)\rangle = \frac{2\sqrt{\alpha}}{\eta_{21}\sqrt{x_1-c}}\left(\frac{P(x_1)\cos\chi^*(x_1)}{\sqrt{b-x_1}} + \frac{Q(x_1)\sin\chi^*(x_1)}{\sqrt{a-x_1}}\right)$$

Integrating this equation, one arrives at:

$$\langle u_3(x_1,0)\rangle = \int_c^{x_1}\left[\frac{2\sqrt{\alpha}}{\eta_{21}\sqrt{t-c}}\left(\frac{P(t)\cos\chi^*(t)}{\sqrt{b-t}} + \right.\right. \\ \left.\left. + \frac{Q(t)\sin\chi^*(t)}{\sqrt{a-t}}\right)\right]dt\,, c < x_1 < a. \quad (48)$$

and also the real part of (46) and imaginary part of (47) lead to the following system of equations at the interval $x_1 \in (c,a)$:

$$\eta_{12}\langle D_2(x_1,0)\rangle + \eta_{13}\langle B_2(x_1,0)\rangle = \\ = -(E_1^{\infty} + \omega_{13}H_1^{\infty})\cdot\frac{x_1-(a+c)/2}{\sqrt{(x_1-c)(a-x_1)}},$$

$$\eta_{22}\langle D_2(x_1,0)\rangle + \eta_{23}\langle B_2(x_1,0)\rangle = \\ = -\frac{P_2(x_1)}{\sqrt{b-x_1}}\sin\chi^*(x_1) + \frac{Q_2(x_1)}{\sqrt{a-x_1}}\cos\chi^*(x_1). \quad (49)$$

From this system the expressions for $\langle D_2(x_1,0)\rangle$ and $\langle B_2(x_1,0)\rangle$ at the interval (c,a) can be easily found.

With use of (42), it follows from (33) for $x_1 > b$:

$$\sigma_{32}^{(1)}(x_1,0) + i\left(\omega_{22}E_1^{(1)}(x_1,0) + \omega_{23}H_1^{(1)}(x_1,0)\right) = \\ = i\left[\frac{Q(x_1)}{\sqrt{x_1-a}} + \frac{iP(x_1)}{\sqrt{x_1-b}}\right]\frac{(1+\gamma_2)\exp[i\chi(x_1)]}{\sqrt{x_1-c}}.$$

From this equation the expression for the stress at the crack continuation can be written in the form:

$$\sigma_{32}^{(1)}(x_1,0) = -(1+\gamma_2)\left(\frac{Q(x_1)}{\sqrt{x_1-a}}\cdot\frac{\sin[\chi(x_1)]}{\sqrt{x_1-c}} + \right. \\ \left. + \frac{P(x_1)}{\sqrt{x_1-b}}\cdot\frac{\cos\chi(x_1)}{\sqrt{x_1-c}}\right)\,, x_1 > b. \quad (50)$$

For electrical and magnetic fields at the crack continuation $x_1 > b$ one arrives at the following system:

$$E_1^{(1)}(x_1,0) + \omega_{13}H_1^{(1)}(x_1,0) = \\ = (E_1^{\infty} + m_{13}H_1^{\infty})\frac{x_1-(a+c)/2}{\sqrt{(x_1-c)(x_1-a)}}, \quad (51)$$

$$\omega_{22}E_1^{(1)}(x_1,0) + \omega_{23}H_1^{(1)}(x_1,0) = \\ = \frac{(1+\gamma_2)}{\sqrt{x_1-c}}\cdot\left(\frac{Q(x_1)}{\sqrt{x_1-a}}\cos[\chi(x_1)] - \frac{P(x_1)}{\sqrt{x_1-b}}\sin[\chi(x_1)]\right). \quad (52)$$

From the last system the expressions for $E_1^{(1)}(x_1,0)$ and $H_1^{(1)}(x_1,0)$ at $x_1 > b$ can be easily found.

Consider now the interval (a,b). Taking into account that at this interval (Herrmann and Loboda, 2003):

$$X_1^{\pm}(x_1)=\frac{\pm e^{\pm\chi_0(x_1)}}{\sqrt{(x_1-c)(b-x_1)}},\ X_2^{\pm}(x_1)=\frac{e^{\pm\chi_0(x_1)}}{\sqrt{(x_1-c)(x_1-a)}},$$

where: $\chi_0(x_1)=2\varepsilon_2\tan^{-1}\sqrt{\frac{(a-c)(b-x_1)}{(b-c)(x_1-a)}}$ and using (42), one can write

$$\Phi_2^{\pm}(x_1)=\pm\frac{e^{\pm\chi_0(x_1)P\ (x_1)}}{\sqrt{(x_1-c)(b-x_1)}}+\frac{e^{\pm\chi_0(x_1)Q\ (x_1)}}{\sqrt{(x_1-c)(x_1-a)}}. \quad (53)$$

Substituting (53) into (36), (39) and taking into account that $\langle D_2(x_1,0)\rangle=0$, $\langle B_1(x_1,0)\rangle=0$ at (a,b) we obtain the following expression for the displacement jump:

$$\langle u'_3(x_1,0)\rangle=\frac{2}{\eta_{21}\sqrt{x_1-c}}\left(\frac{P(x_1)}{\sqrt{b-x_1}}\cosh\chi_0(x_1)+\right.$$

$$\left.+\frac{Q(x_1)}{\sqrt{x_1-a}}\sinh\chi_0(x_1)\right)\ ,\ a<x_1<b.$$

Integrating this equation, one arrives at:

$$\langle u_3(x_1,0)\rangle=\int_b^{x_1}\left[\frac{2}{\eta_{21}\sqrt{t-c}}\left(\frac{P(t)}{\sqrt{b-t}}\cosh\chi_0(t)+\right.\right.$$

$$\left.\left.+\frac{Q(t)}{\sqrt{t-a}}\sinh\chi_0(t)\right)\right]dt,\ a<x_1<b. \quad (54)$$

The formulas (32), (33) give for $a<x_1<b$ the equation (51) and the following expression:

$$\omega_{22}E_1^{(1)}(x_1,0)+\omega_{23}H_1^{(1)}(x_1,0)=$$

$$=\frac{P(x_1)}{\sqrt{(x_1-c)(b-x_1)}}\left(e^{\chi_0(x_1)}-\gamma_2e^{-\chi_0(x_1)}\right)+$$

$$+\frac{\mathrm{Q}(x_1)}{\sqrt{(x_1-c)(x_1-a)}}\left(e^{\chi_0(x_1)}+\gamma_2e^{-\chi_0(x_1)}\right). \quad (55)$$

From the system (51), (55) the expressions for $E_1^{(1)}(x_1,0)$ and $H_1^{(1)}(x_1,0)$ at $a<x_1<b$ can be easily found.

5. STRESS, ELECTRIC AND MAGNETIC INTENSITY FACTORS

Analysis of the formulas (47)-(49) and (52), (53) shows that the stress $\sigma_{32}^{(1)}(x_1,0)$ is singular for $x_1\to b+0$, $E_1^{(1)}(x_1,0)$, $H_1^{(1)}(x_1,0)$ are singular for $x_1\to a+0$ and $x_1\to b-0$, and also $\langle D_2(x_1,0)\rangle$, $\langle B_2(x_1,0)\rangle$ are singular for $x_1\to a-0$. In all mentioned cases, a square root singularity takes place. Therefore, introducing the following stress and electrical intensity factors (IFs):

$$K_3=\lim_{x_1\to b+0}\sqrt{2\pi(x_1-b)}\sigma_{32}(x_1,0),$$

$$K_E^a=\lim_{x_1\to a+0}\sqrt{2\pi(x_1-a)}E_1^{(1)}(x_1,0),$$

$$K_H^a=\lim_{x_1\to a+0}\sqrt{2\pi(x_1-a)}H_1^{(1)}(x_1,0),$$

$$K_E^b=\lim_{x_1\to b-0}\sqrt{2\pi(b-x_1)}E_1^{(1)}(x_1,0),$$

$$K_H^b=\lim_{x_1\to b-0}\sqrt{2\pi(b-x_1)}H_1^{(1)}(x_1,0),$$

$$K_D^a=\lim_{x_1\to a-0}\sqrt{2\pi(a-x_1)}\langle D_2(x_1,0)\rangle,$$

$$K_B^a=\lim_{x_1\to a-0}\sqrt{2\pi(a-x_1)}\langle B_2(x_1,0)\rangle$$

and using formulas (50), (51), (55) and (48), (49), one obtains:

$$K_3=-\frac{(1+\gamma_2)\sqrt{2\pi}}{\sqrt{b-c}}P(b),$$

$$K_E^a+\omega_{13}K_H^a=\sqrt{\frac{\pi(a-c)}{2}}(E_1^{\infty}+\omega_{13}H_1^{\infty}),$$

$$\omega_{22}K_E^a+\omega_{23}K_H^a=\sqrt{\frac{2\pi}{a-c}}(1+\gamma_2)Q(a), \quad (56)$$

$$K_E^b+\omega_{13}K_H^b=0,$$

$$\omega_{22}K_E^b+\omega_{23}K_H^b=\sqrt{\frac{2\pi}{b-c}}(1-\gamma_2)P(b), \quad (57)$$

$$\eta_{12}K_D^a+\eta_{13}K_B^a=-(E_1^{\infty}+\omega_{13}H_1^{\infty})\sqrt{\pi(a-c)/2},$$

$$\eta_{22}K_D^a+\eta_{23}K_B^a=\sqrt{2\pi}Q(a). \quad (58)$$

Substituting the expressions for $P(b)$ from (42), we obtain the following formula:

$$K_3=\sqrt{\frac{\pi l}{2}}\{-\sigma_{32}^{\infty}cos\beta-(\omega_{22}E_1^{\infty}+\omega_{23}H_1^{\infty})sin\beta-$$

$$-2\varepsilon_2\sqrt{1-\lambda}[-\sigma_{32}^{\infty}sin\beta+(\omega_{22}E_1^{\infty}+\omega_{23}H_1^{\infty})cos\beta]\}. \quad (59)$$

The intensity factors K_E^a and K_H^a, K_E^b and K_H^b, K_D^a and K_B^a can be found from the systems (56), (57), (58), respectively.

At the left crack tip c, an oscillating singularity takes place. Such singularity for a conductive interface crack in an anti-plane case of a piezoelectric material has been already analyzed in papers by Wang et al., (2003) and Wang and Zhong (2002). For this reason, we do not pay special attention to this singularity here. At the right crack tip, the same oscillating singularity will take place only if $a=b$, i.e. if the permeable part of the crack is absent. In a more general case, which is studied in this paper, i.e. for zone $[a,b]$ having nonzero length, the previously mentioned oscillating singularity at the point $a=b$ transforms into two square root singularities at two different points a and b with intensity factors defining by Eqs. (56)-(59). Similar situation has been studied for an antiplane case of a piezoelectric material by Lapusta et al., (2017) and also it is similar to the case of a frictionless contact zone at the interface crack tip for a plane problem (Comninou, 1977).

6. NUMERICAL REALIZATION

For the numerical analysis the materials with the following characteristics (Sih and Song, 2003) were chosen:

$$\mathrm{c}_{44}^{(1)}=43.7\cdot10^9[Pa],\ e_{15}^{(1)}=17[C/m^2],$$

$$\alpha_{11}^{(1)}=15.1\cdot10^{-9}\left[\frac{C}{V\cdot m}\right],\quad d_{11}^{(1)}=0,\ \ h_{15}^{(1)}=165\left[\frac{N}{a\cdot m}\right],$$

$$\gamma_{11}^{(1)}=180.5\cdot10^{-6}\left[\frac{N\cdot s^2}{C^2}\right],\ \ \mathrm{c}_{44}^{(2)}=42.47\cdot10^9[Pa],$$

$$e_{15}^{(2)}=-0.48[C/m^2],\quad \alpha_{11}^{(2)}=0.0757\cdot10^{-9}\left[\frac{C}{V\cdot m}\right],$$

$$d_{11}^{(2)}=0,h_{15}^{(2)}=385\left[\frac{N}{\mathrm{a}\cdot m}\right],\gamma_{11}^{(2)}=414.5\cdot10^{-6}\left[\frac{N\cdot s^2}{C^2}\right]$$

and $c = -0.01m$, $b = 0.01\ m$, $\lambda = 0{,}1$.

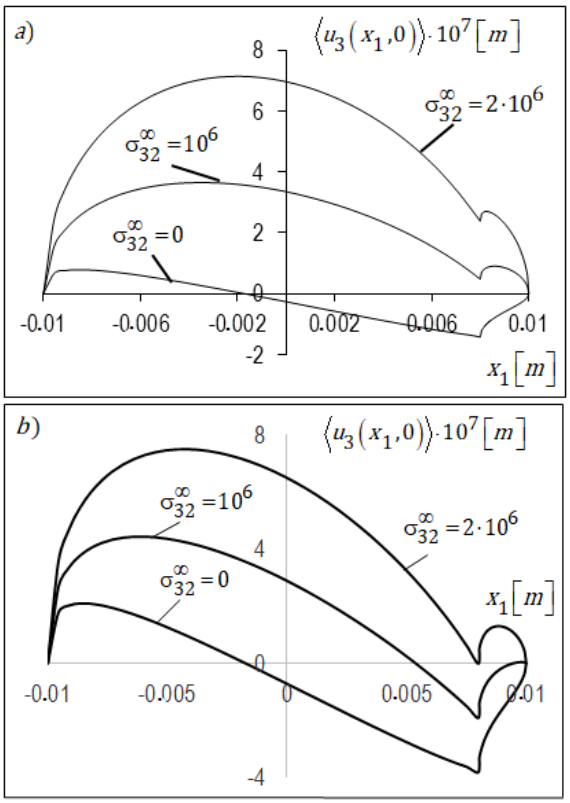

Fig. 2. The displacement jump at the segment $[c, b]$ for $E_1^{\infty} = 9 \cdot 10^3[V/m]$, $H_1^{\infty} = 0$ (a) and $E_1^{\infty} = 0$, $H_1^{\infty} = 1.7 \cdot 10^4[A/m]$ (b)

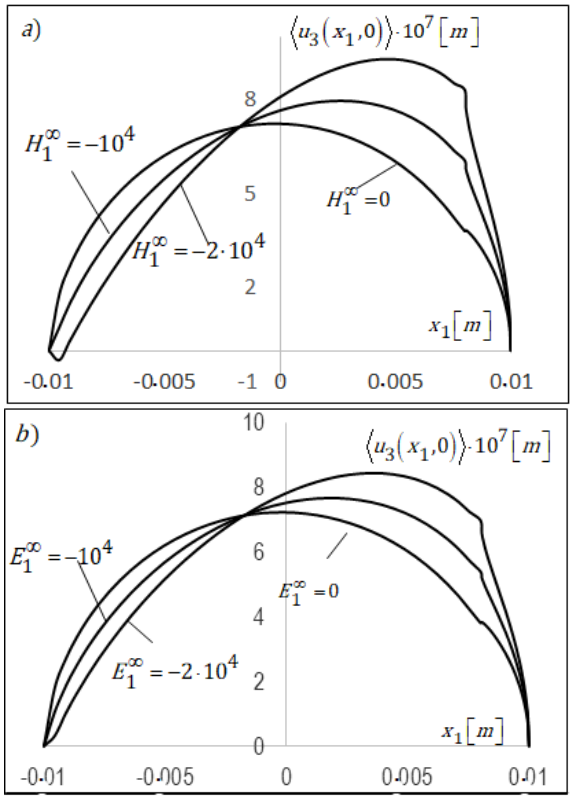

Fig. 3. The displacement jump at the segment $[c, b]$ for different vaues of $H_1^{\infty}[A/m]$ (a) and $E_1^{\infty}[V/m]$(b)

The crack sliding for $E_1^{\infty} = 9 \cdot 10^3[V/m]$, $H_1^{\infty} = 0$ and $E_1^{\infty} = 0$, $H_1^{\infty} = 1.7 \cdot 10^4[A/m]$ and different values of $\sigma_{32}^{\infty}[Pa]$ are presented in Figures 2a and 2b, respectively. It can be seen from these Figures that even for zero mechanical loading σ_{32}^{∞} the crack faces slide with respect to each other due to non-zero electric (Fig. 2a) or magnetic (Fig. 2b) fields.

The crack sliding for $\sigma_{32}^{\infty} = 2 \cdot 10^6[Pa]$ and different values of $H_1^{\infty}[A/m]$ and $E_1^{\infty}[V/m]$ are presented in Figs. 3a and 3b, respectively.

It should be mention that the oscillating singularity takes place at the left crack tip. However for the presented model of the crack sliding the oscillating singularity is physically admissible because the faces can slide relative to each other in any direction. One of the appearances the negative crack faces jump (analogy of the oscillating singularity) can be seen for the lower lines at the left crack tip in Fig. 3a.

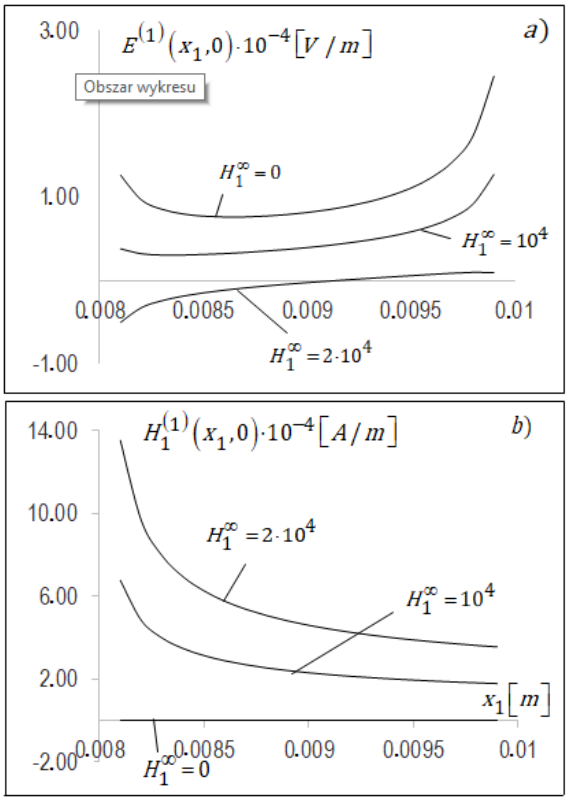

Fig. 4. The variation of the electric $E_1^{(1)}(x_1, 0)$ (a) and magnetic $H_1^{(1)}(x_1, 0)$ (b) fields along the electro-magnetically permeable crack region (a, b)

The variation of the electric $E_1^{(1)}(x_1, 0)$ and magnetic $H_1^{(1)}(x_1, 0)$ fields along the electro-magnetically permeable crack region (a, b) are shown in Figs. 4a and 4b, respectively, for $\lambda = 0.1$, $\sigma_{32}^{\infty} = 10^6[Pa]$, $E_1^{\infty} = 0$ and different values of $H_1^{\infty}[A/m]$. It is seen from these figures that $E_1^{(1)}(x_1, 0)$ and $H_1^{(1)}(x_1, 0)$ is almost equal to 0 for $E_1^{\infty} = 0$ and $H_1^{\infty} = 0$, but they become rather large for a nonzero external magnetic field. Besides, $E_1^{(1)}(x_1, 0)$ and $H_1^{(1)}(x_1, 0)$ are singular at both ends of the segment $[a, b]$.

Consider further the behavior of mechanic, electric and magnetic values at the crack continuation. Fig. 5 show the stress $\sigma_{32}^{(1)}(x_1, 0)$ variations in this zone for $E_1^{\infty} = 9 \cdot 10^3[V/m]$,

$H_1^\infty = 0$ (a) and $E_1^\infty = 0$, $H_1^\infty = 1.7 \cdot 10^4 [A/m]$ (b) and different values of $\sigma_{32}^\infty [Pa]$.

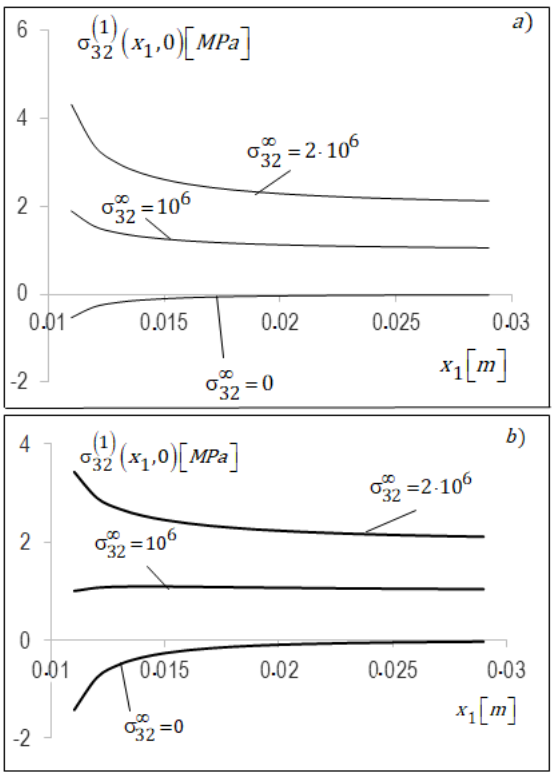

Fig. 5. The stress $\sigma_{32}^{(1)}(x_1, 0)$ variations on (a, b) for $E_1^\infty = 9 \cdot 10^3 [V/m]$, $H_1^\infty = 0$ (a) and $E_1^\infty = 0$, $H_1^\infty = 1.7 \cdot 10^4 [A/m]$ (b) and different values of σ_{32}^∞

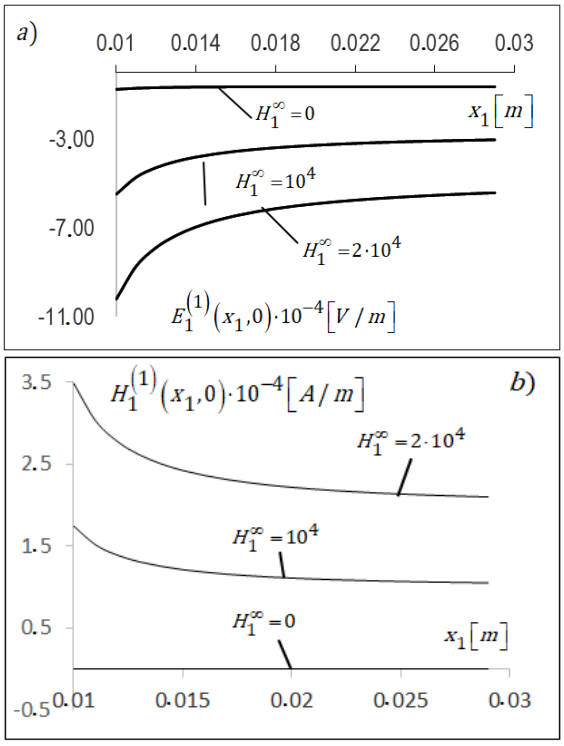

Fig. 6. The variation of the electric $E_1^{(1)}(x_1, 0)$ (a) and magnetic $H_1^{(1)}(x_1, 0)$ (b) fields along the crack continuation $b > 0$ for $\lambda = 0.1$, $\sigma_{32}^\infty = 10^6 [Pa]$, $E_1^\infty = 0$ and different values of H_1^∞

The variation of the electric $E_1^{(1)}(x_1, 0)$ and magnetic $H_1^{(1)}(x_1, 0)$ fields along the crack continuation $b > 0$ are shown in Figs. 6a and 6b, respectively, for $\lambda = 0.1$, $\sigma_{32}^\infty = 10^6 [Pa]$, $E_1^\infty = 0$ and different values of $H_1^\infty [A/m]$. It is seen from these figures that $H_1^{(1)}(x_1, 0)$ is almost equal to 0 for $E_1^\infty = 0$ and $H_1^\infty = 0$, but $E_1^{(1)}(x_1, 0)$ decreases on modulus while $H_1^{(1)}(x_1, 0)$ increases with growing of H_1^∞.

Variations of the normalized stress intensity factor (SIF) K_3 is shown in Tables 1 for $\sigma_{32}^\infty = 10^6 [Pa]$, $E_1^\infty = 0$ and different values of λ and H_1^∞. It can be seen that for each λ the decreasing of magnetic field H_1^∞ (growing it on modules) leads to decreasing of the SIF K_3 and even to turning it into zero for $\lambda = 0.1$ and $H_1^\infty = -18742 [A/m]$. It means that electric and magnetic fields can be used for governing of the SIF and decreasing the probability of fracture.

Tab. 1. Variations of the normalized stress intensity factor (SIF) K_3

H^∞ \ λ	0.1	0.2	0.3
0	177676.	181031.	181731.
-5000	130277.	150716.	160997.
-10000	82877.8	120401.	140263.
-15000	35478.5	90086.	119529.
-18742.6	0.0	67394.7	104009.

To control the obtained analytical solution the numerical experiment has been performed. The finite sized body composed of two piezoelectric parallelepipeds $-30mm \le x_1 \le 30mm$, $0 \le x_2 \le 20mm$, $0 \le x_3 \le 180mm$ and $-30mm \le x_1 \le 30mm$, $-20mm \le x_2 \le 0$, $0 \le x_3 \le 180mm$ with the same piezoelectric material parameters as above is considered. A crack in the region $-10mm \le x_1 \le 10mm$, $x_2 = 0$, $0 \le x_3 \le 180mm$ is situated. It is assumed that for $-10mm \le x_1 \le 5mm$ the faces of the crack are conductive while in the remaining part they are permeable. The lower boundary $x_2 = -20mm$ was fixed while to the upper one $x_2 = 20mm$ the uniformly distributed shear stress $\sigma_{32}^{(1)}(x_1, 20) = 10MPa$ was applied. The finite element ABAQUS code was used for the solution of this problem. The mesh grinding at the crack tips was done. As a result of this solution the maximum value of the crack sliding at the point $x_1 = x_2 = 0$, $x_3 = 90mm$ turned out to be $4.93 \times 10^{-4} mm$. Analytical analysis performing for the same loading, materials, conducting and permeable zone lengths gave the result 4.61×10^{-4} mm for the crack sliding at the same point. Taking into account that we compared the results for finite size domain (with a crack 3 times shorter than the width of the compound) and for infinite domain, the obtained error in 6.51% can be considered as quite satisfactory. Therefore, this numerical test confirms the validity of the analytical approach developed in this paper.

7. CONCLUSIONS

An interface crack $c \le x_1 \le b$, $x_2 = 0$ between two semi-infinite piezoelectric/piezomagnetic spaces $x_2 > 0$ and $x_2 < 0$

under out-of-plane mechanical load and in-plane electrical and magnetic fields parallel to the crack faces is considered. The part (c, a) of the crack $(a \leq b)$ faces is assumed to be electrically conductive and having uniform distribution of magnetic potential on it faces. The remaining part of the crack faces is electrically and magnetically permeable. Such situation can occur because of a soft multi-layered electrode exfoliation, made of ferromagnetic material, situated at the interval $[c, a]$, with additional exfoliation of the interval $[a, b]$ of the non-electroded interface. The considered problem involves the mixed electric and magnetic conditions at the crack faces and is much more complicated than the traditional formulation of the interface crack problem for a conductive crack.

The presentations (32), (33) and (35), (36) were formulated for mechanical, electrical, and magnetic factors via a functions which are analytic in the whole plane except the crack region. With these representations the combined Dirichlet-Riemann boundary value problem (37), (38) and Hilbert problem (44) are formulated and solved in the form of relatively simple analytical formulas for any position of the point a. Due to this solution analytical expressions for stress, electric and magnetic fields as well as for the crack faces displacement jump are presented. The singularities of the obtained solution at the points a and b are investigated and the formulas for the corresponding intensity factors are presented. In Figures 2-6 the variations of the mechanic, electric and magnetic quantities along the appropriate parts of the interface are illustrated for certain materials combinations and for certain positions of the point a. The stress intensity factor corresponding to the results of Figs. 2-6 are given in Tab. 1.

The results of analytical and numerical analysis showed that both electric and magnetic fields essentially influence the mechanical, electrical and magnetic fields at the crack tip. It follows from this results that the mentioned fields can be used for decreasing of the stress intensity factor and consequently for the decreasing of failure dangerous of electronic devices working under the action of the mention fields.

REFERENCES

1. **Beom H. G., Atluri S. N.** (2002), Conducting cracks in dissimilar piezoelectric media, *International Journal of Fracture*, 118, 285–301.
2. **Chen H., Wei W., Liu J., Fang D.** (2012), Propagation of a mode-III interfacial crack in a piezoelectric-piezomagnetic bi-material, *Int. J. Solids Struct.*, 49, 2547–2558.
3. **Comninou M.** (1977), The interface crack, *Trans. ASME. Ser. E, J. Applied Mechanics*, 44(4), 631–636.
4. **Fan C., Zhou Y., Wang H., Zhao M.** (2009), Singular behaviors of interfacial cracks in 2D magnetoelectroelastic bimaterials, *Acta Mech. Solida Sinica*, 22, 232-239.
5. **Feng W. J., Ma P., Pan E. N., Liu J. X.** (2011), A magnetically impermeable and electrically permeable interface crack with a contact zone in a magnetoelectroelastic bimaterial under concentrated magnetoelectromechanical loads on the crack faces, *Sci. China Ser. G*, 54, 1666-1679.
6. **Feng W. J., Ma P., Su R. K. L.** (2012), An electrically impermeable and magnetically permeable interface crack with a contact zone in magnetoelectroelastic bimaterials under a thermal flux and magneto-electromechanical loads, *Int. J. Solids Structures*, 49, 3472-3483.
7. **Feng W. J., Su R. K. L., Liu J. X., Li Y. S.** (2010), Fracture analysis of bounded magnetoelectroelastic layers with interfacial cracks under magnetoelectromechanical loads: plane problem, *J. Intell. Mater. Syst. Struct.*, 21, 581-594.
8. **Govorukha V., Kamlah M., Loboda V., Lapusta Y.** (2016), Interface cracks in piezoelectric materials, *Smart Mater. Struct.,* 25, 023001 (20pp).
9. **Herrmann K. P., Loboda V. V.** (2003), Fracture mechanical assessment of interface cracks with contact zones in piezoelectric bimaterials under thermoelectromechanical loadings, I. Electrically permeable interface cracks, *Int. J. Solids and Structures*, 40, 4191-4217.
10. **Herrmann K. P., Loboda V. V., Khodanen T. V.** (2010), An interface crack with contact zones in a piezoelectric/piezomagnetic bimaterial, *Archive of Applied Mechanics*, 80(6), 651-670.
11. **Hu K., Chen Z.** (2010), An interface crack moving between magnetoelectroelastic and functionally graded elastic layers, *Appl. Math. Modelling*, 38, 910-925.
12. **Kozinov S., Loboda V., Lapusta Y.** (2013), Periodic set of limited electrically permeable interface cracks with contact zones, *Mech. Res. Communic.*, 48, 32-41.
13. **Lapusta Y., Onopriienko O., Loboda V.** (2017), An interface crack with partially electrically conductive crack faces under antiplane mechanical and in-plane electric loadings, *Mech. Res. Commun.*, 81, 38–43.
14. **Li R., Kardomateas G. A.** (2006), The mode III interface crack in piezo-electro-magneto-elastic dissimilar bimaterials, *J. Appl. Mech.*, 73, 220–227.
15. **Li Y. D., Lee K. Y.** (2010), Effects of magneto-electric loadings and piezomagnetic/piezoelectric stiffening on multiferroic interface fracture, *Eng. Fract. Mech.*, 77, 856-866.
16. **Loboda V., Sheveleva A., Lapusta Y.** (2014), An electrically conducting interface crack with a contact zone in a piezoelectric bimaterial, *Int. J. Solids Struct.*, 51, 63–73.
17. **Ma P., Feng W. J., Su R. K. L.** (2012), An electrically impermeable and magnetically permeable interface crack with a contact zone in a magnetoelectroelastic bimaterial under uniform magnetoelectromechanical loads, *Eur. J. Mech. A/Solids*, 32, 41-51.
18. **Ma P., Feng W. J., Su R. K. L.** (2013), Pre-fracture zone model on electrically impermeable and magnetically permeable interface crack between two dissimilar magnetoelectroelastic materials, *Eng. Fract. Mech.*, 102, 310-323.
19. **Ma P., Feng W., Su R. K. L.** (2011), Fracture assessment of an interface crack between two dissimilar magnetoelectroelastic materials under heat flow and magnetoelectromechanical loadings, *Acta Mech. Solida Sinica*, 24, 429-438.
20. **Muskhelishvili N. I.** (1977), *Some Basic Problems of Mathematical Theory of Elasticity*, Noordhoff International Publishing, Leyden.
21. **Nahmein E. L., Nuller B. M.** (1986), Contact of an elastic half plane and a particularly unbonded stamp [in russian], *Prikladnaja matematica i mechanika*, 50, 663–673.
22. **Parton V. Z., Kudryavtsev B. A.** (1988), *Electromagnetoelasticity*, Gordon and Breach Science Publishers, New York.
23. **Ru C. Q.** (2000), Electrode-ceramic interfacial cracks in piezoelectric multilayer materials, *ASME J. Appl. Mech.*, 67, 255–261.
24. **Shi P. P., Sun S., Li X.** (2013), The cyclically symmetric cracks on the arc-shaped interface between a functionally graded magneto-electro-elastic layer and an orthotropic elastic substrate under static anti-plane shear load, *Eng. Fract. Mech.*, 105, 238-249.
25. **Sih G. C., Song Z. F.** (2003), Magnetic and electric poling effects associated with crack growth in $BaTiO_3$–$CoFe_2O_4$ composite, *Theoretical and Applied Fracture Mechanics*, 39, 209–227.
26. **Su R. K. L., Feng W. J.** (2008), Fracture behavior of a bonded magneto-electro-elastic rectangular plate with an interface crack, *Arch. Appl. Mech.*, 78, 343–362.
27. **Sulym H. T., Piskozub L. G., Piskozub Y. Z., Pasternak Ya. M**. (2015a), Antiplane deformation of a bimaterial containing an interfacial crack with the account of friction. I. Single loading, *Acta Mechanica et Automatica*, 9(2), 115-121.
28. **Sulym H. T., Piskozub L. G., Piskozub Y. Z., Pasternak Ya. M.** (2015b), Antiplane deformation of a bimaterial containing an interfacial crack with the account of friction. 2. Repeating and cyclic loading, *Acta Mechanica et Automatica*, 9(3), 178-184.

29. **Wan Y, Yue Y, Zhong Z.** (2012a), Multilayered piezomagnetic/ piezoelectric composite with periodic interface cracks under magnetic or electric field, *Eng. Fract. Mech.*, 84, 132–145.
30. **Wan Y., Yue Y., Zhong Z.** (2012b), A mode III crack crossing the magnetoelectroelastic bimaterial interface under concentrated magnetoelectromechanical loads, *Int. J. Solids Structures*, 49, 3008-3021.
31. **Wang B. L., Mai Y. W.** (2006), Closed-form solution for an antiplane interface crack between two dissimilar magnetoelectroelastic layers, *J. Appl. Mech.*, 73, 281–290.
32. **Wang B. L., Mai Y. W.** (2008), An exact analysis for mode III cracks between two dissimilar magneto-electro-elastic layers, *Mech. Compos. Mater.*, 44, 533–548.
33. **Wang X., Zhong Z.** (2002), A conducting arc crack between a circular piezoelectric inclusion and an unbounded matrix, *Int. J. Solids Struct.*, 39, 5895–5911.
34. **Wang X., Zhong Z., Wu F. L.** (2003), A moving conducting crack at the interface of two dissimilar piezoelectric materials, *Int. J. Solids Struct.*, 40, 2381–2399.
35. **Yue Y., Wan Y.** (2014), Multilayered piezomagnetic/piezoelectric composite with periodic interfacial Yoffe-type cracks under magnetic or electric field, *Acta Mech.*, 225, 2133-2150.
36. **Zhou Z. G., Chen Y., Wang B.** (2007), The behavior of two parallel interface cracks in magneto-electro-elastic materials under an anti-plane shear stress loading, *Compos. Struct.*, 77, 97–103.
37. **Zhou Z. G., Wang B., Sun Y. G.** (2004), Two collinear interface cracks in magneto-electro-elastic composites, *Int. J. Eng. Science*, 42, 1155–1167.
38. **Zhou Z. G., Wang J. Z., Wu L. Z.** (2009), The behavior of two parallel non-symmetric interface cracks in a magneto-electro-elastic material strip under an anti-plane shear stress loading, *Int. J. Appl. Electromagn. Mech.*, 29, 163–184.
39. **Zhou Z. G., Zhang P. W., Wu L. Z.** (2007), Solutions to a limited-permeable crack or two limited-permeable collinear cracks in piezoelectric/piezomagnetic materials, *Arch. Appl. Mech.*, 77, 861–882.

Acknowledgements: This work has been carried out within the framework of the Transversal Program of the Pascal Institute (UMR CNRS 6602), Division "Materials and Multiscale Modeling", of the Excellence Laboratory LabEx IMobS3 (ANR-10-LABX-16-01) (supported by the French program investissement d'avenir and managed by the National Research Agency (ANR), the European Commission (Auvergne FEDER funds) and the Region Auvergne), and, also, of the project CAP 20-25, Axis 2, Theme Usine du Futur, which is gratefully acknowledged.

sciendo

DOI 10.2478/ama-2018-0047

acta mechanica et automatica, vol.12 no.4 (2018)

STATISTICAL ANALYSIS OF HUMAN HEART RHYTHM WITH INCREASED INFORMATIVENESS

Serhii LUPENKO[*], Nadiia LUTSYK[*], Oleh YASNIY[*], Łukasz SOBASZEK[**]

[*]Faculty of Computer Information Systems and Software Engineering, Ternopil Ivan Pul'uj National Technical University, 46001, Ruska str. 56, Ternopil, Ukraine
[**]Institute of Technological Systems of Information, Mechanical Engineering Faculty, Lublin University of Technology, ul. Nadbystrzycka 38 D, 20–618 Lublin

lupenko.san@gmail.com, lutsyk.nadiia@gmail.com, oleh.yasniy@gmail.com, l.sobaszek@pollub.pl

received 10 July 2018, revised 17 December 2018, accepted 20 December 2018

Abstract: The new methods of statistical analysis of heart rhythm were developed based on its generalized mathematical model in a form of random rhythm function, that allows to increase the informativeness and detailed analysis of heart rhythm in cardiovascular information systems. Three information criteria (BIC, AIC and AICc) were used to determine the cumulative distribution functions that best describe the sample and to assess the unknown parameters of distributions. The usage of the rhythm function to analyse heart rhythm allows to consider much better its time structure that is the basis to improve the accuracy of diagnosis of cardiac rhythm.

Key words: Mathematical Model, Heart Rhythm, Statistical Analysis, Diagnosis, Information System

1. INTRODUCTION

The study of heart rhythm is one of the most promising non-invasive methods of diagnosis of the cardiovascular system and the adaptive capacity of the human body, since it is a sensitive indicator of the degree of concordance and order in the functioning of the human body as an integral system (Akaike, 1974; Ciucurel et al., 2018; Evaristo et al., 2018; Fumagalli et al., 2018; Gadhoumi et al., 2018; Galeotti and Scully, 2018).

Analysis of heart rhythm allows to perform early diagnostics of abnormal fetal, to identify autonomic neuropathy in diabetic patients, to assess the risk of death after myocardial infarction, to determine the measure of tension of human body regulatory process state, etc (Hammad et al., 2018; Isler et al., 2019; Koichubekoc et al., 2018; Li et al., 2018; Mustaqeem et al., 2017; Napoli et al., 2018; Serrano and Figiola, 2009; Sharma and Sunkria, 2018; Shen et al., 2015; Wang et al., 2018).

In modern cardiovascular information systems, the research of heart rhythm is implemented by recording and automated processing of cardiointervalogram or rhythmogram (Brandão et al., 2014).

Cardiointervalogram is the sequence of values that are equal to the time intervals between peak values of R-wave of electrocardiogram in the sequential cardiac cycles. Rhythmogram is a discrete process that is defined on a finite or on a counTab. set of moments of time equal to the moment of time when the peak values of electrocardiogram R-wave are recorded and rhythm cardiogram values are equal to the time intervals between peak values of electrocardiogram R-wave. Rhythmogram is more informative empirical curve related with the analysis of heart rhythm as compared with cardiointervalogram because it contains information about the moments of time at which the peak values of R-wave of electrocardiogram are recorded (Bozhokin and Suslova, 2014).

However, this kind of curve does not allow to determine more detailed features of heart rhythm, since it reflects only changes in the duration of the cardiac cycle. Therefore, it does not take into account the entire set of time intervals between single-phase values of heart cyclic signal for every phase. The latter data enable to represent the rhythm in completely.

Cardiointervalogram and rhythmogram have insufficient precision and informativeness for the heart rhythm analysis (Kotel'nikov et al., 2002). This points out the relevance and prospects of developing a new approach to modeling and analysis of heart rhythm. This would allow increasing the level of informativeness, the growth of reliability of heart rhythm analysis that provide the early diagnosis of cardiac diseases and regulatory activity of the human body as a whole.

2. METHODOLOGY

2.1. New approach for the analysis of heart rhythm

The growth of reliability and informativeness of heart rhythm analysis can be achieved by statistical analysis of not only RR-intervals which define the duration of the cardiac cycle but also by identifying statistical patterns for the greater amount of time intervals that separate the single-phase intervals of electrocardiogram. The electrocardiogram as a registered electrocardiosignal $\xi(\omega, t)$ is convenient to be treated theoretically as a deterministic function $\xi_{\omega}(t)$ of real argument ($t \in R$). For example, the following single-phase counting of electrocardiogram may be the starts of P-wave, Q-wave, R-wave, S-wave, T-wave, U-wave. That is, the object of the statistical analysis of rhythm is a set of sequences of

DOI 10.2478/ama-2018-0047

time intervals between single-phase counting of electrocardiogram, namely, the sequences $TT(t_{T,n})$, $PP(t_{P,n})$, $QQ(t_{Q,n})$, $RR(t_{R,n})$, $SS(t_{S,n})$ determined by the formulae:

$$PP(t_{P,n}) = P(t_{P,n}) - P(t_{P,n-1})$$
$$QQ(t_{Q,n}) = Q(t_{Q,n}) - Q(t_{Q,n-1})$$
$$RR(t_{R,n}) = R(t_{R,n}) - R(t_{R,n-1})$$
$$SS(t_{S,n}) = S(t_{S,n}) - S(t_{S,n-1}) \quad (1)$$
$$TT(t_{T,n}) = T(t_{T,n}) - T(t_{T,n-1})$$
$$UU(t_{U,n}) = U(t_{U,n}) - U(t_{U,n-1}); n = \overline{2,N},$$

where: $P(t_{P,n})$, $Q(t_{Q,n})$, $R(t_{R,n})$, $S(t_{S,n})$, $T(t_{T,n})$, $U(t_{U,n})$ are the time moments of start of P-wave, Q-wave, R-wave, S-wave, T-wave, U-wave, respectively, n is a number of cardiac cycles.

Under this approach, the more informative discrete function is constructed. Theoretically, it can be as dense as necessary and can be transformed into a function of real argument $T(t)$, $t \in R$. This function is called the rhythm function of cyclic process [18]. In this case, the electrocardiosignal is such a cyclic process.

The formation of the above sequences and rhythm function from electrocardiogram is schematically presented in Fig. 1.

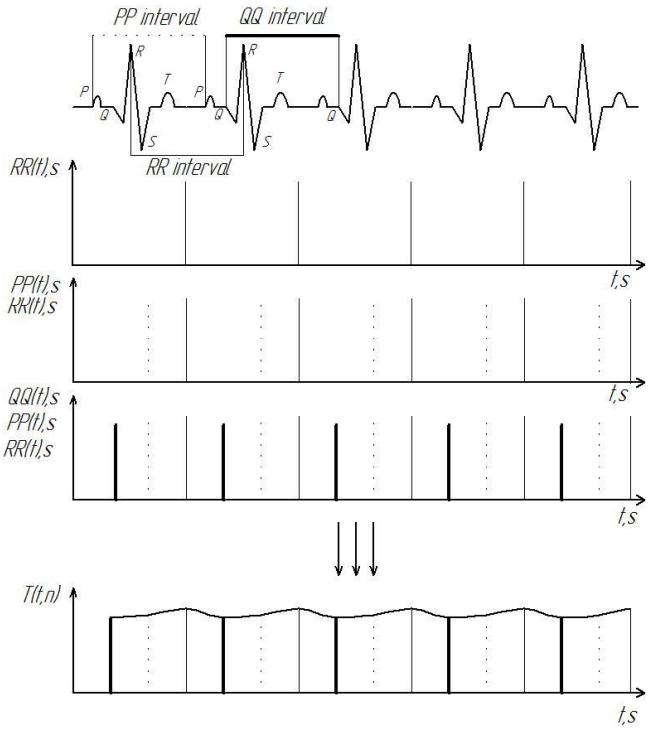

Fig. 1. Scheme of formation sequences of time intervals between single-phase counting of electrocardiogram

There were performed 20 experiments on the processing of electrocardiograms based on the presented above approach to the analysis of heart rhythm with a purpose of its verification. For example, let's present the results of one of these experiments. Namely, the electrocardiogram of male was registered. His age was 58 years. The graph of several cycles of registered electrocardiogram is shown in Fig. 2.

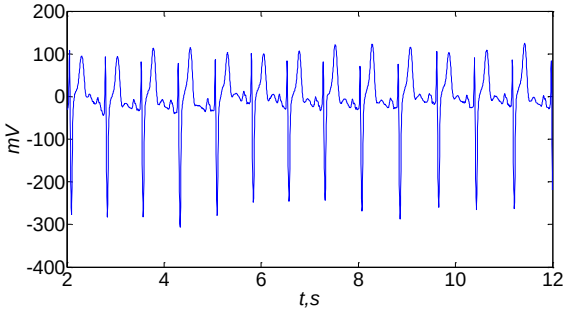

Fig. 2. The graph of registered electrocardiogram

The lengths of PP, TT, QQ, RR, SS intervals were estimated for every cardiac cycle of registered electrocardiogram by methods available in literature [19]. The plots of obtained sequences $TT(t_{T,n})$, $PP(t_{P,n})$, $QQ(t_{Q,n})$, $RR(t_{R,n})$, $SS(t_{S,n})$ are shown in Fig. 3.

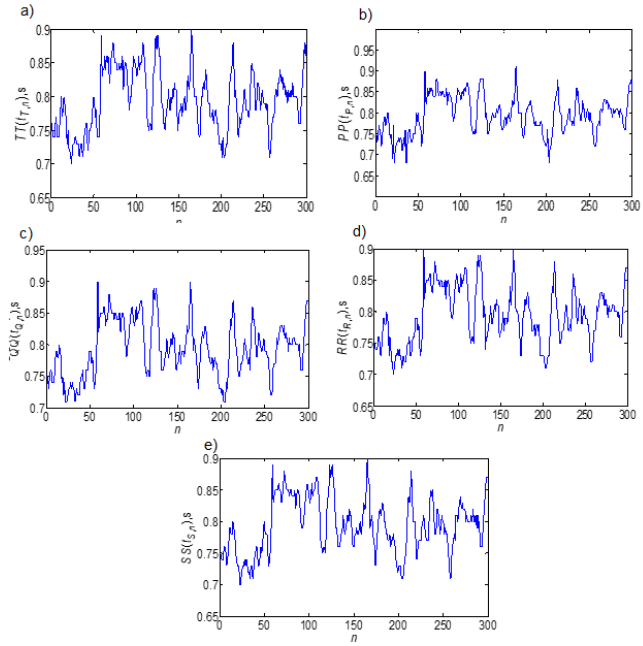

Fig. 3. Time intervals between a single-phase countings of ECG: a) $TT(t_{T,n})$, b) $PP(t_{P,n})$, c) $QQ(t_{Q,n})$, d) $RR(t_{R,n})$, e) $SS(t_{S,n})$

It is necessary to explain the mathematical model of the above mentioned sequences, in order to perform the statistical estimation of their stochastic characteristics. As in the case of mathematical models of rhythm cardiogram, these models of the above-indicated sequences can be both stationary and non-stationary random sequences. Therefore, the first step in explanation of the mathematical model as the foundation of statistical analysis of random sequences is the stationarity test, which can be done by applying the method of Foster-Stewart [8]. This method allows to check for trend components in the mathematical expectation (mean) and variance of the studied random sequences. Statistics of the criteria are as follows:

$$K = \sum_{i=2}^{n} K_i \quad (2)$$
$$d = \sum_{i=2}^{n} d_i \quad (3)$$

where: $d_i = u_i - l_i, K_i = u_i + l_i,$

$$u_i = \begin{cases} 1, \text{if the i}^{\text{th}} \text{ observation is an upper record} \\ 0, \text{otherwise.} \end{cases} \quad (4)$$

$$l_i = \begin{cases} 1, \text{if the i}^{\text{th}} \text{ observation is an lower record} \\ 0, \text{otherwise.} \end{cases} \quad (5)$$

The *K* statistics is used to check the trend in the variance of the random sequence, and the *d* statistics is employed to identify a trend in its mathematical expectation. It is obvious, that

$$0 \le K \le n-1 \text{ and } -(n-1) \le d \le n-1. \quad (6)$$

In the absence of trend, the random variables $t = \frac{d}{f}$ and $\tilde{t} = \frac{t-f^2}{l}$, where $l = \sqrt{2\ln n - 3.4253}$, $f = \sqrt{2\ln n - 0.8456}$ are distributed according to Student distribution with $v = n$ degrees of freedom.

If $|t|$, $|\tilde{t}| > t_{\frac{1+\alpha}{2}}$, then the null hypothesis of the absence of trend is rejected with the confidence level of α.

3. RESULTS

The values of corresponding statistics for different sequences $TT(t_{T,n})$, $PP(t_{P,n})$, $QQ(t_{Q,n})$, $RR(t_{R,n})$, $SS(t_{S,n})$ are presented in Tab. 1.

Tab. 1. The values of calculated statistics for sequences PP, TT, QQ, RR, SS of ECG (Fig. 3)

Intervals	$\|t\|$	$\|\tilde{t}\|$	$t_{0.975}$
TT	0	0.1966	1.9679
PP	0.6154	0.1989	1.9679
QQ	0.3076	1.2626	1.9679
RR	0	0.9068	1.9679
SS	0.3076	0.5550	1.9679

The verification of stationarity hypotheses confirmed that the mentioned above random sequences $TT(t_{T,n})$, $PP(t_{P,n})$, $QQ(t_{Q,n})$, $RR(t_{R,n})$, $SS(t_{S,n})$ do not contradict the hypothesis of stationarity.

The informative characteristics of heart rate analysis and methods of their study were determined. The significant characteristics of random sequences are their mathematical expectation, variance, probability density and cumulative distribution functions. Tab. 2 provides the values of mathematical expectation and variance of the given sequences.

Tab. 2. The mathematical expectation and variance of sequences TT, PP, QQ, RR, SS

Intervals	Expected value	Variance
TT	0.794	1.97e-3
PP	0.795	2e-3
QQ	0.795	1.9e-3
RR	0.795	1.95e-3
SS	0.795	1.94e-3

Three information criteria were used to determine the cumulative distribution functions that best describe the sample and the unknown parameters of distributions. These criteria are Akaike information criterion (AIC), Bayesian information criterion (BIC) and Akaike information criterion with a correction for finite sample sizes (AICc).

Tab. 3. The best fit distributions and their parameters obtained for sequences PP, TT, QQ, RR, SS

Interval	Inform.criter.	Name of distribution	Parameters of distribution
PP	AIC	GEV	$\xi = -0.299$ $\mu = 0.0448$ $\sigma = 0.7793$
	BIC	GEV	$\xi = -0.2802$ $\mu = 0.0435$ $\sigma = 0.7787$
	AICc	GEV	$\xi = -0.299$ $\mu = 0.0448$ $\sigma = 0.7793$
QQ	AIC	GEV	$\xi = -0.2819$ $\mu = 0.0433$ $\sigma = 0.779$
	BIC	GEV	$\xi = -0.2819$ $\mu = 0.0433$ $\sigma = 0.779$
	AICc	GEV	$\xi = -0.2819$ $\mu = 0.0433$ $\sigma = 0.779$
RR	AIC	GEV	$\xi = -0.283$ $\mu = 0.0435$ $\sigma = 0.779$
	BIC	GEV	$\xi = -0.283$ $\mu = 0.0435$ $\sigma = 0.779$
	AICc	GEV	$\xi = -0.283$ $\mu = 0.0435$ $\sigma = 0.779$
SS	AIC	GEV	$\xi = -0.2938$ $\mu = 0.0436$ $\sigma = 0.7792$
	BIC	GEV	$\xi = -0.2938$ $\mu = 0.0436$ $\sigma = 0.7792$
	AICc	GEV	$\xi = -0.2938$ $\mu = 0.0436$ $\sigma = 0.7792$
TT	AIC	GEV	$\xi = -0.2802$ $\mu = 0.0435$ $\sigma = 0.7787$
	BIC	Birnb.-Saund.	$\alpha = 0.7932$ $\beta = 0.0558$
	AICc	GEV	$\xi = -0.2802$ $\mu = 0.0435$ $\sigma = 0.7787$

The values of AIC information criterion can be found by the following formula (Akaike, 1974):

$$\text{AIC} = 2\ln L_{max} + 2k, \quad (7)$$

DOI 10.2478/ama-2018-0047

where: L_{max} is the maximum of likelihood function, k is the number of parameters of distribution. The best model is the one that minimizes the value of AIC. This criterion is obtained by the approximate minimization of Kullback-Leibler information entropy. It is a measure of the difference between the true distribution of data and the distribution of the model (Liddle, 2007).
The values of BIC information criterion can be determined by the following formula (Schwarz, 1978):

$$\mathrm{BIC} = -2\ln L_{max} + k\ln N, \tag{8}$$

where: N is the sample size.

While using BIC, the researcher suggests that the elements of the sample are independent and identically distributed. The application of AIC and BIC criteria usually shows good agreement between the conclusions about the best model (Liddle, 2007).

In the case when the sample size is insignificant, it is advisable to use the AICc. The value of this criterion is calculated using the formula (Sugiura, 1978):

$$\mathrm{AICc} = \mathrm{AIC} + 2\mathrm{k}(\mathrm{k}+1)/\mathrm{N}\text{-}\mathrm{k}\text{-}1. \tag{9}$$

As a result of the use of information criteria, it was found that these samples of different intervals (PP, TT, QQ, RR, SS) are best described by two distribution functions − generalized extreme values function (Fisher-Tippett distribution) and Birnbaum-Saunders distribution (see Tab. 3).

Recall that generalized extreme values (GEV) function has the following form:

$$G(z) = \exp\left\{-\left[1+\xi\left(\frac{z-\mu}{\sigma}\right)\right]^{-\frac{1}{\xi}}\right\}. \tag{10}$$

where: ξ, μ, σ are the parameters of distribution (Coles, 2001).

The Birnbaum-Saunders (Birnb.-Saund.) distribution is described by the following expression:

$$F(x;\alpha,\beta) = \Phi\left(\frac{1}{\alpha}\left[\left(\frac{x}{\beta}\right)^{\frac{1}{2}} - \left(\frac{\beta}{x}\right)^{\frac{1}{2}}\right]\right). \tag{10}$$

where: $\Phi(x)$ is the cumulative function of normal distribution, α, β are the parameters of distribution (Coles, 2001).

The probability density function and cumulative distribution function of TT and PP intervals are shown in Fig. 4.

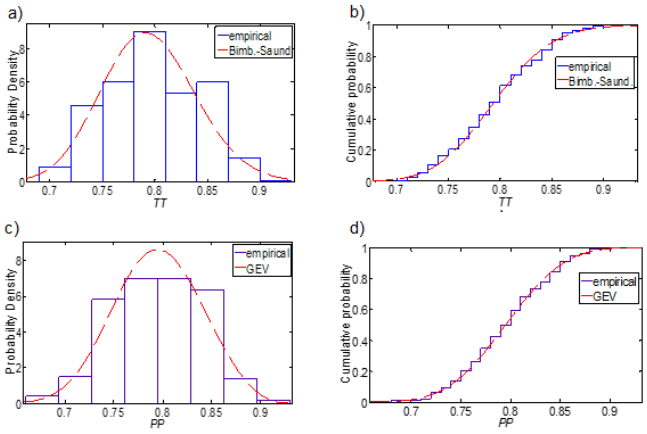

Fig. 4. The probability density function and cumulative distribution function of intervals a) TT interval, b) PP interval

It was found that the random sequences $TT(t_{T,n})$, $PP(t_{P,n})$, $QQ(t_{Q,n})$, $RR(t_{R,n})$, $SS(t_{S,n})$ are the stationary random processes. Their probabilistic characteristics, such as mathematical expectation, variance, probability density function and cumulative density function were estimated. The calculated mathematical expectation and variance are practically identical for every random sequence. This is also true for the estimated parameters of distributions. These sequences can be described well enough by Fisher–Tippett distribution.

4. CONCLUSIONS

Three information criteria (BIC, AIC and AICc) were used to determine the cumulative distribution functions that best describe the sample and to estimate the unknown parameters of distributions. It was found that the samples of different intervals (PP, TT, QQ, RR, SS) are well enough described by next distribution functions − generalized extreme values function (Fisher-Tippett distribution) and Birnbaum-Saunders distribution. Also, it was determined that the mentioned above random sequences are the stationary random processes. Their probabilistic characteristics, such as the mathematical expectation, variance, probability density function and cumulative density function were estimated. For this case, the calculated mathematical expectation and variance are practically identical for every random sequence. The mathematical expectation of samples was approximately equal to 0.795 s, and the variance is around 0.2 s^2. This is also true for the estimated parameters of distributions.

In general, the use of the rhythm function to analyze heart rhythm allows considering much better its time structure that is the basis to improve the accuracy of diagnosis of cardiac rhythm.

REFERENCES

1. **Akaike H.** (1974), A new look at the statistical model identification, *IEEE Transactions on Automatic Control*, 19(4), 716–723.
2. **Berkaya S.K., Uysal A.K., Gunal E.S, Ergin S., Gunal S., Gulmezoglu M.B.** (2018), A survey on ECG analysis, *Biomedical Signal Processing and Control*, 43, 216-235.
3. **Bozhokin S.V., Suslova I.B.** (2014), Wavelet Analysis of Non-stationary Signals in Medical Cyber-Physical Systems (MCPS). B S. Balandin, S. Andreev, & Y. Koucheryavy (Eds), *Internet of Things, Smart Spaces and Next Generation Networks and Systems*, Springer International Publishing.
4. **Brandão G.S., Sampaio A.A.C., Brandão G.S., Urbano J.J., Fonsêca N.T., Apostólico N., Oliveira E.F., Perez E.A., Almeida R.G., Dias I.S., Santos I.R., Nacif S.R., Oliveira L.V.F.** (2014), Analysis of heart rate variability in the measurement of the activity of the autonomic nervous system: technical note, *Manual Therapy, Posturology & Rehabilitation Journal*, 12, 243-251.
5. **Ciucurel C., Georgescu L., Iconaru E.I.** (2018), ECG response to submaximal exercise from the perspective of Golden Ratio harmonic rhythm, *Biomedical Signal Processing and Control*, 40, 156-162.
6. **Coles S.** (2001), *Extreme values, regular variation and point processes,* Springer, London.
7. **Evaristo R.M., Batista A.M., Viana R.L., Iarosz K.C., Szezech J.D. Jr., Godoy M.F.** (2018). Mathematical model with autoregressive process for electrocardiogram signals, *Communications in Nonlinear Science and Numerical Simulation*, 57, 415-421.
8. **Foster F.G., Stuart A.** (1954), Distribution-Free Tests in Time-Series Based on the Breaking of Records, *Journal of the Royal Statistical Society. Series B* (*Methodological*), 16(1), 1-22.

10. **Fumagalli F., Silver A.E**., **Tan Q., Zaidi N., Ristagno G.** (2018), Cardiac rhythm analysis during ongoing cardiopulmonary resuscitation using the Analysis During Compressions with Fast Reconfirmation technology, *Heart Rhythm*, 15(2), 248-255.
11. **Gadhoumi K., Do D., Badilini F., Pelter M.M., Hu X.** (2018), Wavelet leader multifractal analysis of heart rate variability in atrial fibrillation, *Journal of Electrocardiology*, 51(6), S83-S87.
12. **Galeotti L., Scully C.G.** (2018), A method to extract realistic artifacts from electrocardiogram recordings for robust algorithm testing, *Journal of Electrocardiology*, 51(6), S56-S60.
13. **Hammad M., Maher A., Wang K., Jiang F., Amrani M.** (2018), Detection of abnormal heart conditions based on characteristics of ECG signals, *Measurement*, 125, 634-644.
14. **Isler Y., Narin A., Ozer M., Perc M.** (2019), Multi-stage classification of congestive heart failure based on short-term heart rate variability, *Chaos, Solitons & Fractals*, 118, 145-151.
15. **Koichubekov B.K., Sorokina M.A., Laryushina Y.M., Turgunova L.G., Korshukov I.V.** (2018), Nonlinear analyses of heart rate variability in hypertension, *Annales de Cardiologie et d'Angéiologie*, 67(3), 174-179.
16. **Kotel'nikov S.A., Nozdrachev A.D., Odinak M.M., Shustov E.B., Kovalenko I.Yu., Davydenko V.Yu.** (2002), Cardiac Rhythm Variability: Approaches to Mechanisms, *Human Physiology*, 28(1), 114-127.
17. **Li J., Chen Ch., Yao Q., Zhang P., Wang J., Hu J., Feng F.** (2018), The effect of circadian rhythm on the correlation and multifractality of heart rate signals during exercise, *Physica A: Statistical Mechanics and its Applications*, 509, 1207-1213.
18. **Liddle A.R.** (2007), Information criteria for astrophysical model selection, *Monthly Notices of the Royal Astronomical Society: Letters*, 377(1), 74-78.
19. **Lupenko S., N. Lutsyk, Y. Lapusta.** (2015), Cyclic linear random process as a mathematical model of cyclic signals, *Acta Mechanica et Automatica*, 9(4), 219-224.
20. **Lytvynenko I., Maruschak P., Lupenko S., Panin S.** (2015), Segmentation and Statistical Processing of Geometric and Spatial Data on Self-Organized Surface Relief of Statically Deformed Aluminum Alloy, *Applied Mechanics and Materials*, 770, 288-293.
21. **Mustaqeem A., Anwar SM, Khan AR., Majid M.** (2017), A statistical analysis based recommender model for heart disease patients, *International Journal of Medical Informatics*, 108, 134-145.
22. **Napoli N.J., Demas M.W., Mendu S., Stephens C.L., Kennedy K.D, Harrivel A.R, Bailey R.E., Barnes L.E.** (2018), Uncertainty in heart rate complexity metrics caused by R-peak perturbations, *Computers in Biology and Medicine*, 103, 198-207.
23. **Schwarz G.** (1978). Estimating the Dimension of a Model. *The Annals of Statistics*, 6(2), 461-464.
24. **Serrano E., Figliola A.** (2009), Wavelet Leaders: A new method to estimate the multifractal singularity spectra, *Physica A: Statistical Mechanics and its Applications*, 388(14), 2793-2805.
25. **Sharma L.D., Sunkaria R.K.** (2018), Stationary wavelet transform based technique for automated external defibrillator using optimally selected classifiers, *Measurement*, 125, 29-36.
26. **Shen C., Yu Z., Liu Z.** (2015), The use of statistics in heart rhythm research: a review, *Heart Rhythm*, 12(6), 1376-1386.
27. **Sugiura N.** (1978). Further analysts of the data by akaike' s information criterion and the finite corrections. *Communications in Statistics - Theory and Methods*, 7(1), 13-26.
28. **Wang Y., Wei S., Zhang S., Zhang Y., Zhao L., Liu C., Murray A.** (2018), Comparison of time-domain, frequency-domain and non-linear analysis for distinguishing congestive heart failure patients from normal sinus rhythm subjects, *Biomedical Signal Processing and Control*, 42, 30-36.

ABSTRACTS

Vladimir V. Savenko
Electroplastic Deformation by Twinningmetals

The article deals with theoretical and experimental approaches to electroplastic deformation caused by twinning of metals. The author specifies physical fundamentals of Kinetics regarding the development of twinning caused by the excitation of electronic subsystem of metals. Physical models of new channels for the realization of twinning aroused under conditions of electroplasticity have been discussed. Mechanisms of plasticized influence of a surface electric charge have been defined as well as the contribution of a dynamic pinch-effect in the elastic plastic deformation of metals with the participation of the intrinsic magnetic field of the current. The dynamic pinch effect creates ultrasonic vibration of the lattice system while Kinetics changes and plastic deformation are stimulated increasing the amplitude of the oscillations of rectilinear dislocations and the periodic change in the position of the dislocation loops with an increase in the probability of detachment of dislocations from the stoppers. When deformed above the yield point and due to the pinch effect the intrinsic magnetic field of the current diffuses into the crystal where the diffusion rate depends both on the conductivity of the metal and on the frequency of the current. It is necessary to take into account the physical conditions for the creation of ponderomotive effects in relation to specific technically important materials for the practical use of electroplastic deformation technology, especially when processing metals with pressure.

Małgorzata Poniatowska
Optimizing Sampling Parameters of CMM Data Acquisition for Machining Error Correction Of Freeform Surfaces

An optimization study using the design of experiment technique is described, in which the surface profile height of a freeform surface, determined in coordinate measurements, is the response variable. The control factors are coordinate sampling parameters, i.e. the sampling grid size and the measuring tip diameter. As a result of the research, an optimal combination of these parameters was found for surface mapping with acceptable measurement uncertainty. The presented study is the first stage of optimization of machining error correction for the freeform surface and was intended to take into account mechanical-geometric filtration of surface irregularities caused by these geometrical parameters. The tests were carried out on a freeform workpiece milled with specific machining parameters, Ra of the surface roughness was 1.62 μm. The search for the optimal combination of parameters was conducted using Statistica software.

Leyla Sultanova
Two-Parametric Analysis of Anti-Plane Shear Deformation of a Coated Elastic Half-Space

The anti-plane shear deformation problem of a half-space coated by a soft or a stiff thin layer is considered. The two-term asymptotic analysis is developed motivated by the scaling for the displacement and stress components obtained from the exact solution of a model problem for a shear harmonic load. It is shown that for a rather high contrast in stiffness of the layer and the half-space Winkler-type behaviour appears for a relatively soft coating, while for a relatively stiff one, the equations of plate shear are valid. For low contrast, an alternative approximation is suggested based on the reduced continuity conditions and the fact that the applied load may be transmitted to the interface. In case of a stiff layer, a simpler problem for a homogeneous half-space with effective boundary condition is also formulated, modelling the effect of the coating, while for a relatively soft layer a uniformly valid approximate formula is introduced.

Józef Tutaj, Bogdan Fijałkowski
A New Fuel-Injection Mechatronic Control Method for Direct-Injection Internal Combustion Engines

In this paper, a novel fuel-injection mechatronic control method and system for direct injection (DI) internal combustion engines (ICE) is proposed. This method and system is based on the energy saving in a capacitance using DC-DC converter, giving a very fast ON state of the fuel injectors' electro-magnetic fluidical valves without an application of the initial load current. A fuel-injection controller for the DI ICEs that provides a very short rising time of an electromagnet-winding current in an initial ON state of the fuel-injector's electromagnetic fluidical valves, which improves a fuel-injection controller reliability and simplify its construction, is presented. Due to a number of advantages of afore -mentioned fuel-injection mechatronic control method and system, it may be utilised for the DI ICEs with fuel injectors dedicated to all types of liquid and/or gas fuels, for example, gasoline, diesel-oil, alkohol, LPG and NPG.

Volodimyr Kalchenko, Andrij Yeroshenko, Sergiy Boyko
Crossing Axes of Workpiece and Tool at Grinding of the Circular Trough with Variable Profile

In the article the method of grinding with crossed axes of the tool and the workpiece got further developed. The work discloses a method of processing details having an external surface with a profile in the form of an arc of a circle of variable radius (for example, rolls of pipe rolling mills). The particular three-dimensional geometric models of the processing, shaping and profiling of abrasive wheels have been developed. A method for controlling the grinding process, which ensures the removal of allowances along equidistant curves has been offered. The developed method of grinding provides a constant depth of cutting according to the coordinate of profile processing. This is achieved at the expense of the synchronous inclination of the wheel and its insertion by the size of the allowance. The diameter of grinding wheel affects on the maximum angle of orientation of the wheel has been proven. It has been shown that increasing the diameter of the abrasive wheel has led to a slight decrease in value orientation angle.

Łukasz Wójcik, Zbigniew Pater
Comparison Analysis of Cockroft – Latham Criterion Values of Commercial Plasticine and C45 Steel

The paper presents and compares the results of theoretical and experimental research in the field of cracking of model material (commercial plasticine) and C45 steel in hot forming conditions. The aim of the research was to determine the limit values of the Cockroft-Latham integral for both materials. The presented research methodology includes experimental tests (tensile tests) and numerical simulations carried out in the DEFORM-3D program. For laboratory tests, axially symmetric samples made of C45 steel and model material were used. On the basis of the obtained experimental and numerical results, a comparative analysis of both materials was carried out.

Santhosh K. Venkata, Bhagya R Navada
Estimation of Flow Rate Through Analysis of Pipe Vibration

In this paper, implementation of soft sensing technique for measurement of fluid flow rate is reported. The objective of the paper is to design an estimator to physically measure the flow in pipe by analysing the vibration on the walls of the pipe. Commonly used head type flow meter causes obstruction to the flow and measurement would depend on the placement of these sensors. In the proposed technique vibration sensor is bonded on the pipe of liquid flow. It is observed that vibration in the pipe varies with the control action of stem. Single axis accelerometer is used to acquire vibration signal from pipe, signal is passed from the sensor to the system for processing. Basic techniques like filtering, amplification, and Fourier transform are used to process the signal. The obtained transform is trained using neural network algorithm to estimate the fluid flow rate. Artificial neural network is designed using back propagation with artificial bee colony algorithm. Designed estimator after being incorporated in practical setup is subjected to test and the result obtained shows successful estimation of flow rate with the root mean square percentage error of 0.667.

Oleg Onopriienko, Volodymyr Loboda, Alla Sheveleva, Yuri Lapusta
An Interface Crack with Mixed Electro-Magnetic Conditions at it Faces in a Piezoelectric/ Piezomagnetic Bimaterial under Anti-Plane Mechanical and In-Plane Electric Loadings

An interface crack between two semi-infinite piezoelectric/piezomagnetic spaces under out-of-plane mechanical load and in-plane electrical and magnetic fields parallel to the crack faces is considered. Some part of the crack faces is assumed to be electrically conductive and having uniform distribution of magnetic potential whilst the remaining part of the crack faces is electrically and magnetically permeable. The mechanical, electrical, and magnetic factors are presented via functions which are analytic in the whole plane except the crack region. Due to these representations the combined Dirichlet-Riemann and Hilbert boundary value problems are formulated and solved in rather simple analytical form for any relation between conductive and permeable zone lengths. Resulting from this solution the analytical expressions for stress, electric and magnetic fields as well as for the crack faces displacement jump are presented. The singularities of the obtained solution at the crack tips and at the separation point of the mention zones are investigated and the formulas for the corresponding intensity factors are presented. The influence of external electric and magnetic fields upon the mechanic, electric and magnetic quantities at the crack region are illustrated in graph and table forms.

Serhii Lupenko, Nadiia Lutsyk, Oleh Yasniy, Łukasz Sobaszek
Statistical Analysis of Human Heart Rhythm with Increased Informativeness

The new methods of statistical analysis of heart rhythm were developed based on its generalized mathematical model in a form of random rhythm function, that allows to increase the informativeness and detailed analysis of heart rhythm in cardiovascular information systems. Three information criteria (BIC, AIC and AICc) were used to determine the cumulative distribution functions that best describe the sample and to assess the unknown parameters of distributions. The usage of the rhythm function to analyse heart rhythm allows to consider much better its time structure that is the basis to improve the accuracy of diagnosis of cardiac rhythm.